UNIVERSITY OF BIRMINGHAM

Computational Simulations of Pure ThO_2 and $Th_{(1-x)}U_{(x)}O_2$ and $Th_{(1-x)}Pu_{(x)}O_2$ Doped Systems for Nuclear Fuel Applications

By

Claire Louise Green

Supervisor: Dr Mark Read

A thesis submitted to the University of Birmingham for the degree of Doctor of Philosophy

The School of Chemistry

College of Engineering and Physical Sciences

University of Birmingham

September 2016

Declaration

I, Claire Green, confirm that the work resented in this thesis is my own. Where information has been derived from other sources or from colleges within the research group, I confirm that this has been properly indicated and fully acknowledged in this thesis.

Abstract

As the stocks of fossil fuels are rapidly depleting the world has turned to other forms or electricity generation including nuclear power. The production of electricity via nuclear power already supplies a large amount of the world's population and is becoming increasing more viable as the concern of global warming also becoming progressively more apparent. Thorium dioxide fuel has been widely researched and investigated as a potential replacement to uranium dioxide for many years as it has many advantages over the current uranium dioxide fuel. Due to the hazards of working with radioactive materials in the laboratory, computational work has become a popular method to complete initial predictions of the properties and characteristics of the fuel.

A new potential model was developed for both the Th-O and the Gd-O interactions using two different derivation methods. In both cases the potential model included the shell model rather than the previously used rigid ion model; the shell model has been proven to be superior in modelling defects and defect interactions. Potential validation using bulk properties confirmed the robustness of the potentials and allowed confidence in taking them forward to investigate defects such as the introduction of fission products, surface simulations and molecular dynamic simulations.

Within this work the pure and mixed oxide fuels have been examined using various atomistic modelling codes including GULP, METADISE and DL_POLY to allow a robust understanding of the properties and features of the fuel.

Dedication

I would like to dedicate this thesis to my aunt, Constance Booth, who always believed in me, and supported me through every single step of this process.

Acknowledgements

I would like to thank my friends and family who have provided me with support and encouragement throughout this whole process. My parents especially as they have tried their very best to give me guidance and support throughout my entire academic career to date. I would also like to thank my fellow college Geoffrey Cutts for his outstanding patience in teaching me to use his potential derivation code and his continued support throughout my time at the University of Birmingham. Last, but not least, I would like to say thank you to my supervisor, Mark Read, for his invaluable advice and guidance throughout.

List of publications

- *Derivation of Enhanced Interatomic Potentials for Thorium Dioxide (ThO_2): a Potential Nuclear Fuel*. Conference proceedings, 4th annual bear PGR conference (2013).

Poster presentations and oral presentations

- 1st prize poster – MEGS conference, (2012)
- Poster – MEGS conference (2013)
- Poster – Bluebear conference, University of Birmingham (2013)
- Poster and oral presentation – Bluebear conference, University of Birmingham (2013)
- Poster – Solid state conference, Bath University (2013)
- Poster – CCP5 conference, Manchester University (2013)
- Poster – Postgraduate symposium, University of Birmingham (2014)
- Poster – RSC energy conference, London (2015)
- Poster and oral presentation – Postgraduate symposium , University of Birmingham (2015)

Contents

List of Figures

List of Tables

Chapter 1

Introduction

Contents

1.1 Introduction

The use of nuclear power to fulfil the world's energy needs is becoming an increasingly viable option as the stocks of fossil fuels are rapidly depleting. The Hurst report [1] outlines a predicted timeframe for the dates of peak oil production and its expected terminal decline being much sooner than initially expected. Whilst the imminent depletion of fossil fuels is a major concern, the current most pressing issues are that of global emmissions produced in the generation of energy from the burning of these fossil fuels. Whilst the current oil and natural gas supplies are utilised, the production of CO_2 emissions will continue to be a problem with the burden of global warming growing profoundly. The climate change act [2] published in 2008 establised the worlds first climate change target with the aim to reduce the UK's greenhouse gas emissions by at least 80% by 2050. Therefore, alternative methods of fuel production must be investiagted.

Many renewable sources of energy production have been explored such as solar, tidal and wind energy but their reliability upon uncontrollable variables makes them impractical and unreliable as a primary energy source [3]. Hydrogen fuel has posed many promising solutions including its decreased greenhouse gas production [4]. Unfortunately, hydrogen fuel continues to pose issues with storage and safety in addition to requiring energy to produce it by the hydrolysis of water.

Nuclear power is considered to be a cleaner alternative to burning fossil fuels as no greenhouse gases are emitted directly from the fuel burning process. In addition, Sovacool et al. [5] investigated the release of greenhouse emissions

throughout the whole life cycle, including fuel uranium ore mining, fuel fabrication, isotopic enrichment, construction and operation of the fuel plant. The study found that even though there was a release of CO_2 throughout the process, it was still considerably less than that released from burning fossil fuels. In fact, the only other process that produces less CO_2 emissions than nuclear power is offshore wind farms.

This leaves nuclear power as an extremely promising alternative to the world's energy crisis with research into the nuclear power industry being plentiful since the 1950's. The nuclear energy institute [6] recorded 30 countries worldwide that are operating 444 nuclear reactors, with an additional 63 plants under construction. Figure 1 shows the percentage breakdown of the UK's energy supply by different energy sources.

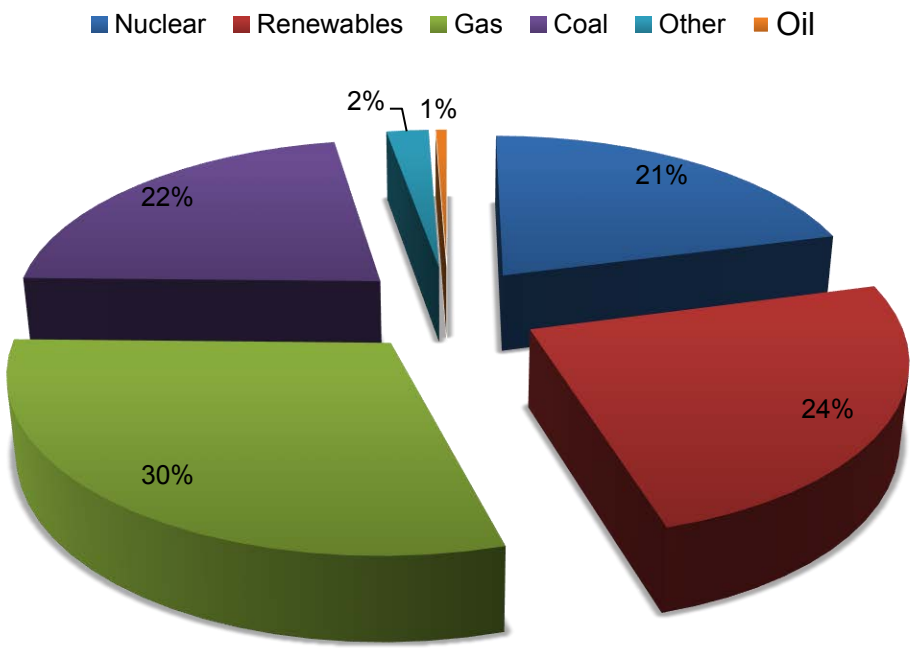

Figure 1: Breakdown of the UK's electricity mix [7]

Whilst nuclear power is already fully utilized in reactors around the world investigations into alternative nuclear fuels is ongoing. This chapter summarises the basic principles of nuclear energy, the types of nuclear fuel including advantages and disadvantages of each and the production of fission materials within the fuel cycle itself.

1.2 Basic Principles of Nuclear Energy

The splitting of atoms during nuclear fission releases large amounts of energy that nuclear reactors can then utilize in the generation of electricity. In fact, the current nuclear process for uranium produces 3.7 million times as much energy as burning the same amount of coal [8]. The basic principles of a nuclear reactor are that the energy released from the fission process is used to heat water in order to generate steam, which can then drive turbines and generate electrical power. A standard nuclear reactor will consist of the reactor core in which the fission process takes place. The core holds the nuclear fuel in tubes called fuel rods; each fuel rod contains around 400 ceramic fuel pellets surrounded by a metallic zircaloy cladding. These fuel rods are then arranged in an ordered assembly within the core. The process of fission is a rapid chain reaction that must be controlled at all times. In nuclear reactors this process is controlled by a number of procedures including control rods and a moderating material within the core. Control rods are made with a neutron absorbing material and can be inserted or withdrawn from the core as required. In some reactors, neutron absorbing materials such as gadolinium can be directly incorporated into the fuel pellets as a moderator to slow down neutrons and ensure fission. The energy released during the fission process can be transferred to a coolant material as heat energy. This coolant material, usually water, is circulated throughout the core. The reactor core is contained within a pressurised vessel separate to the rest of the reactor and the steam generator processes. The whole reactor is then held within a containment vessel that prevents contamination and protects the

outside world from any of the radiation released in any of the nuclear processes within the reactor.

Thoria can be used in many different types of reactors and has been tried and tested in many existing reactors as well as newer prototypes. The type of fuel used varies between reactors; generation IV reactors such as the gas-cooled reactor (GCR), very high temperature reactor (VHTR) and molten salt reactors (MSR) can use a variety of fuel types such as molten thorium fluoride salts or solid thorium dioxide, whereas some reactors, such as pebble bed reactor, a type of VHTR, are only designed for the oxide of the fuel. The molten salt reactor offers many benefits compared to other reactor types; it can run at much higher temperatures, lower pressures and has high thermal to electrical conversion efficiency [9]. Molten salt reactors fuelled by thorium dioxide also produce less plutonium than with any other nuclear fuel.

1.3 Introduction to Nuclear Fuels

A nuclear fuel is a material that is able to sustain a fission chain reaction and therefore act as a source of nuclear energy. Commercial power plants that are in operation today rely on uranium and/or plutonium-uranium mixed fuel with U^{235} being the principal fissile material. The uranium fuel does not only consist of U^{235}, as U^{238} makes up the bulk of the material. It is this U^{238} that undergoes neutron capture to produce plutonium. Multiple isotopes of plutonium are produced in this neutron capture process, but it is Pu^{239} which contributes most heavily to the process and increases the amount of energy produced by the fuel. The

production of plutonium within the fuel seems to be a beneficial factor until the end of the fuel cycle when the spent nuclear fuel still contains a significant amount of plutonium and other actinides that are highly radioactive and difficult to store. The waste produced from the uranium fuel cycle is of growing concern as some of the waste materials, especially plutonium, can remain radioactive for 100,000 years and can contribute significantly to weapon proliferation.

Thorium dioxide, mixed plutonium-thorium and uranium-thorium nuclear fuels are an alternative to current uranium based fuels and have many beneficial factors over uranium, including percentage abundance and safety. Thorium has been investigated as an alternative nuclear fuel for many years [10, 11] with research being conducted since the late 1950s [12, 13]. India has been particularly interested in thorium fuel as it has around 25% of the world's thorium reserves and in the three stage nuclear power programme [15] has already been researched and used extensively [13- 17].

As a fuel, thorium itself is not fissile; it requires a neutron source such as uranium or plutonium to begin the fuel cycle. Once the naturally occurring Th^{232} has absorbed a neutron it forms Th^{233}. This isotope of thorium then undergoes beta decay to eventually form U^{233}. The isotopic uranium formed then undergoes fission itself to produce the heat energy required to generate electricity. Figure 1.1 shows the full transmutation process described above.

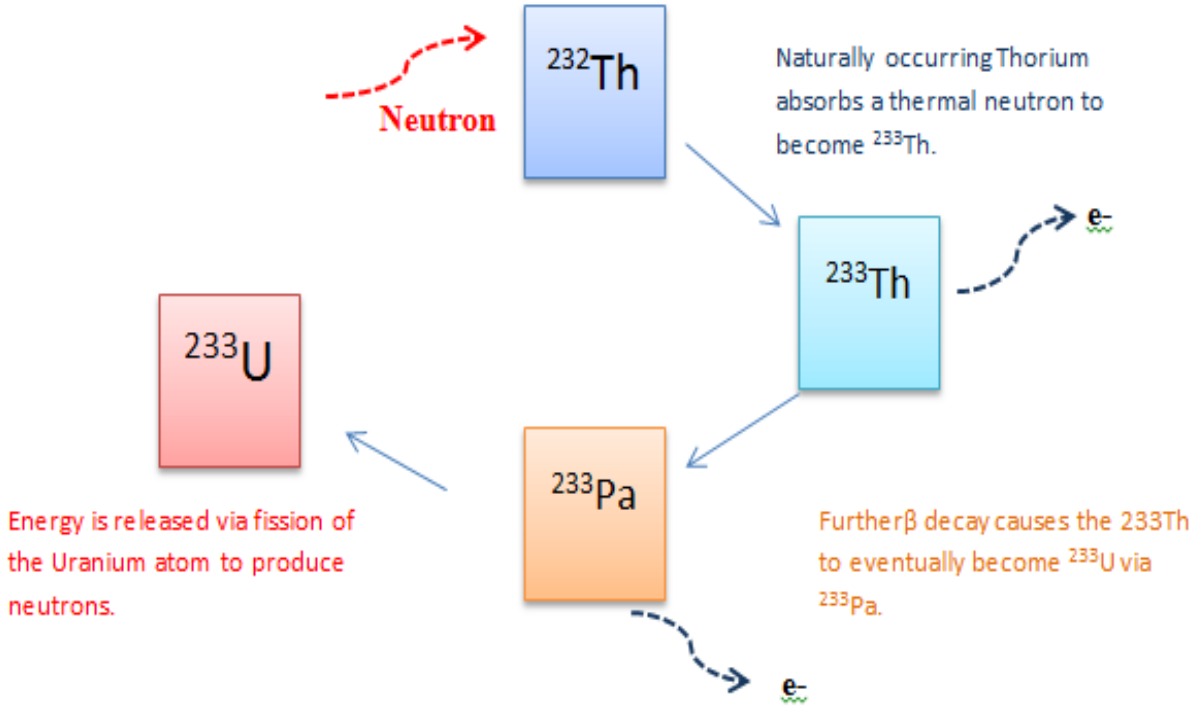

Figure 1.1: Illustration of the thorium fuel cycle

1.4 Benefits of the Thorium Fuel Cycle

The thorium fuel cycle has received a vast amount of interest as it is considered to be much safer than that of the uranium cycle, specifically as it produces less waste actinides such as plutonium [17]. The natural thorium used is Th^{232} requires neutrons to begin the breeding process. Therefore, the natural thorium is combined with either uranium or plutonium to provide the initial neutrons needed. As discussed in section 1.2 the thorium isotope is converted to U^{233} upon capture of a neutron (shown in figure 3) and it is this U^{233} that is used as the energy generating fuel and as U^{233} is the main fuel , not U^{238}, there is not as much Pu^{239} produced. This significantly reduces storage issues and proliferation risks. The

presence of U^{233} produced within the cycle has also been thought to cause difficulty in the manufacture of weapons as it produces a significant gamma dose field.

Apart from the production of less waste plutonium and other actinides, the thorium fuel cycle also has many other potential benefits in comparison with uranium. Naturally, thorium is four times more abundant in the Earth's crust than uranium which means in many countries it can come as an easily exploitable resource. It also promises the long term sustainability of thorium fuelled nuclear power. Thorium dioxide is also more chemically stable than uranium dioxide and does not oxidise as easily. This means that any of the storage issues associated with the oxidation of uranium dioxide can be eliminated for the thorium dioxide fuel.

The most important characteristic of a nuclear fuel is the amount of energy it releases; a fuel must release enough energy throughout the cycle for the whole make up to be economically viable. A way of measuring how much energy can potentially be generated is by measuring the emission of fission neutrons, Eta (η). The more fission neutrons produced per absorption of a thermal neutron the more heat energy released throughout the fuel cycle. In fact, the number of fission neutrons emitted per thermal neutron absorbed must be greater than one for a critical reactor and above two for a breeder reactor [18]. Table 1 shows the spectrum-averaged values for eta for the principle fuel types against temperature.

Temperature (°c)	U^{233}	U^{235}	Pu^{239}
20	2.284	2.065	2.035
100	2.288	2.063	1.998
200	2.291	2.060	1.947
400	2.292	2.050	1.860
600	2.292	2.042	1.811
1000	2.292	2.033	1.770

Table 1: Spectrum-averaged values of Eta (η) against temperature [18].

U^{233} is the principle fuel produced within the thorium fuel cycle and as table 1 shows it is the best fuel for both critical and breeder reactors.

Many of the advantages and disadvantages of uranium and uranium mixed fuels along with thorium and thorium mixed fuels have been discussed within a report published by the National Nuclear Laboratory [19]. The discussion includes resource availability, economics, radiotoxicity and reprocessing of the materials with conclusions that thorium has many more beneficial properties than uranium in the nuclear industry.

1.5 Waste Materials

According to the world nuclear association [19], waste materials produced within a fuel cycle can be categorised as high, medium or low-level depending upon how much radiation they emit. Low-level waste products can be produced throughout all of the stages of the fuel cycle from fuel mining to fuel reprocessing. Medium-level waste products are produced during operation of the nuclear reactor and during fuel processing. The higher-level waste products however are those that cause the most concern and are contained within the spent fuel. These high-level materials emit alpha, beta and gamma radiation and include Pu^{238}, U^{234}, Np^{237} and Am^{241}. The main issues with these waste materials is the long half-life making them difficult to store due to some of the elements having half lives of thousands of years.

Figure 1.3 shows the yield of each fission product produced in the thorium fuel cycle by atomic weight. Fission products with the highest yield have an atomic number in the range of around 30-40 and 50-60. Elements in this range include strontium, barium, xenon and caesium.

As well as emitting damaging radiation, some actinides produced within the fuel cycle such as gadolinium and xenon can act as fuel poisoners. Due to their high neutron absorption capacity, they can absorb neutrons within the fuel that are needed for the chain reaction to continue. This is of particular concern for thorium as it requires neutrons to form the U-233 fuel that is required. Although these materials are initially undesirable, they can also be inserted into the fuel as control

rods to help control the reaction; they can be used to slow down or stop the chain reaction.

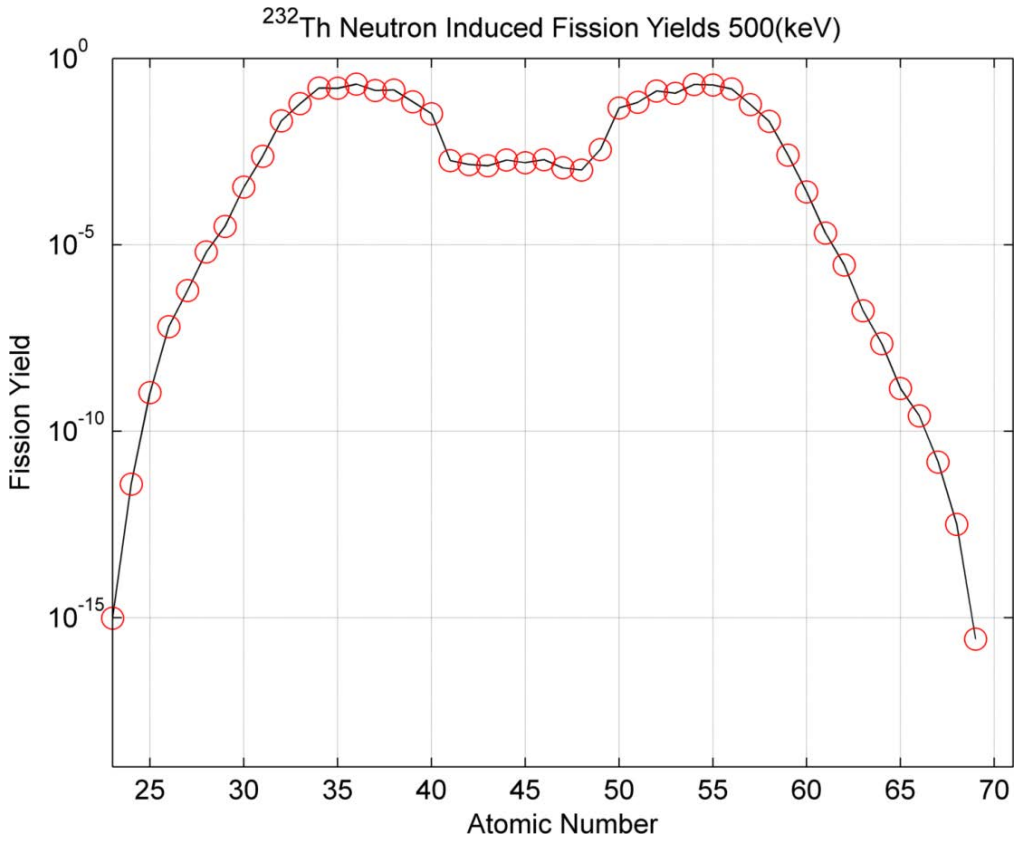

Figure 1.2: Yields of various fission products produced in the thorium fuel cycle [20].

1.6 Thesis summary

The work within this thesis concentrates on the study of pure thorium and uranium/plutonium doped thorium for potential use as a nuclear fuel. Benefits and drawbacks of the thorium fuel cycle have been discussed throughout with the aid of multiple simulated studies of many of the properties of the pure and mixed fuel. I hope that the work carried out in this study will contribute to further fuel simulations and aid in the progress of thorium dioxide as a potential nuclear fuel. Chapter 1 presents an introduction to the theory of the thorium fuel cycle along. Chapter 2 explains the methodology used throughout the calculations including the programmes GULP, METADISE and DLPOLY. In chapter 3, I discuss any existing potentials that have been derived and their uses in modelling the materials along with a description of the potential derivation processes used within my research. Chapters 4, 5 and 6 are results chapters in which I have used the potentials derived to investigate properties of the fuel including defect properties, surface properties and physical and mechanical properties.

Chapter 2

Computational Methodology

Contents

2.1 Introduction

Computational chemistry is extremely versatile and has been proven to be successful in modelling a range of materials from biological pathways to the engineering of buildings [21, 22, 23] with studies of current and next generation nuclear fuels being plentiful [24-27]. One of the main benefits of computational simulations is the ease of use when considering safety; many of the materials studied using computational simulations are either radioactive or incredibly hard to handle in the laboratory due to the protective measures that must be taken. Computational simulations can also be used, for example, to predict properties of materials with half lives of thousands of years which cannot be done experimentally within a realistic timescale. Computational findings can also be used alongside experimental work to validate or enhance our understanding of experimental findings.

Three different simulation codes are employed throughout this work; the general utility lattice program, GULP [28], is used for static lattice calculations including defect calculations. The surface code, METADISE [29], is used to simulate the surface of the material including the perfect and defective system. The molecular dynamics code, DL_POLY [30], is used to study the dynamics of the system in real time. The methodology for each of these codes is described, in turn, in this chapter.

To be able to describe a model accurately all of the interactions between the ions within the crystal must be considered. The simulations carried out within this work are based on the Born model [31] of ionic crystals in which each crystal consists

of discrete ions. These ions will interact with each other via electrostatic attractions and it is these interactions that determine the energetics of the system; for example, the lattice energy (U_L) of an ionic crystal is defined to be the energy required to form the ionic lattice from its gaseous ions from an infinite separation.

2.2 Potential model

The lattice energy of a system can be split into two interactions; the long range and short range interactions, shown in figure 2.

$$U_L \sum = \Phi\mathrm{SR} + \Phi\mathrm{LR}$$

Figure 2: Lattice energy equation as a sum of the long and short range interaction.

The interaction between the ions using this pair potential can be represented graphically (figure 2.5) showing the potential energy of the system as the ions are at long distances (~6Å) and as they approach each other until they are at very short distances (~1-2 Å).

2.2.1 The long range interaction

The long range interaction is the more dominant of the two interactions; in most ionic crystals it accounts for around 80% of the interactions. In simple terms it is the electrostatic interaction between two oppositely charged ions (*i* and *j*). The interaction will be attractive for two oppositely charged ions and repulsive for two ions of the same charge. This interaction can be represented by the equation shown in figure 2.1 which shows the charges of the ions q_i and q_j at a separation of $r_{ij.}$

$$\Phi_{LR}(r_{ij}) = \frac{q_i q_j}{4\pi\varepsilon_o r_{ij}}$$

Figure 2.1: Equation to represent the long range interaction between ions.

The direct summation of the long range interaction gives slow convergence and is computationally expensive due to the reciprocal distance term $\frac{1}{r_{ij}}$. The Ewald approach [32] can be used to estimate the Columbic interactions in order to solve these issues by using reciprocal space to speed up convergence and therefore enhance simulation times.

2.2.2 The short range interaction

The short range interactions combine a number of components such as the more important non-bonded interactions including that of electron cloud overlap, Van der Waals and Pauli repulsions. Electron polarisability is also considered within the short range interaction. A number of interatomic potentials describe the different forms of potential energy of a particular ionic or molecular system. The interatomic potentials are therefore categorized into how many particles are interacting within that system. Two body potentials include only the forces acting between two molecules or ions and can take many forms such as the Morse potential [33], the Lennard-Jones potential [34], Buckingham type [35] and the Born-Mayer potential [31]. The Buckingham and Born-Mayer type potentials are the most commonly used for ionic solids and are those used throughout this work. There are also three-body and mulit-body potentials but they are more suited to covalently bonded systems or systems that show strong covalent characteristics.

$$\emptyset^{\boldsymbol{Buckingham}}{}_{(rij)} = \; A_{ij} \exp\left(-\frac{rij}{\rho ij}\right) - C_{ij} r_{ij}^{-6}$$

Figure 2.2: An equation describing the short range interaction of ions where A, *p* and C are known as the potential parameters and they represent the interactions between the atoms.

The atomistic model combines these two expressions as shown in figure 2 and expressed in more detail in equation 2.3.

$$U(r) = \sum_{ij} \quad \frac{q_i q_j}{\varepsilon r_{ij}} + \sum_{ij} A_{ij} \exp\left(-\frac{r_{ij}}{\rho_{ij}}\right) - \frac{C_{ij}}{r_{ij}^6}$$

Figure 2.3: The Buckingham potential.

The Buckingham-4 potential, employed by Jackson et al [25], can also be used to describe ionic oxides as it can partition the analytical expression to avoid the unphysical attractive forces at very short distances by only applying the most appropriate terms over the relative distances.

$$\emptyset Buck4(r_{ij}) = \begin{cases} A_{ij} exp\left(-\frac{rij}{\rho ij}\right) & if\ r_{min} < r_{ij} \leq cut_{1,} \\ \sum_{m=0}^{5} a_m r_{ij}^m & if\ cut_1 < r_{ij} \leq r_{minimun,} \\ \sum_{n=o}^{3} b_n r_{ij}^n & if\ r_{minimum} < r_{ij} \leq cut_{2,} \\ -\frac{c_{ij}}{r_{ij}^6} & if\ cut_2 < r_{ij} \leq r_{max.} \end{cases}$$

Figure 2.4: the Buckingham four-range potential.

The interactions embodied within the Buckingham four-range potential are illustrated in figure 2.5.

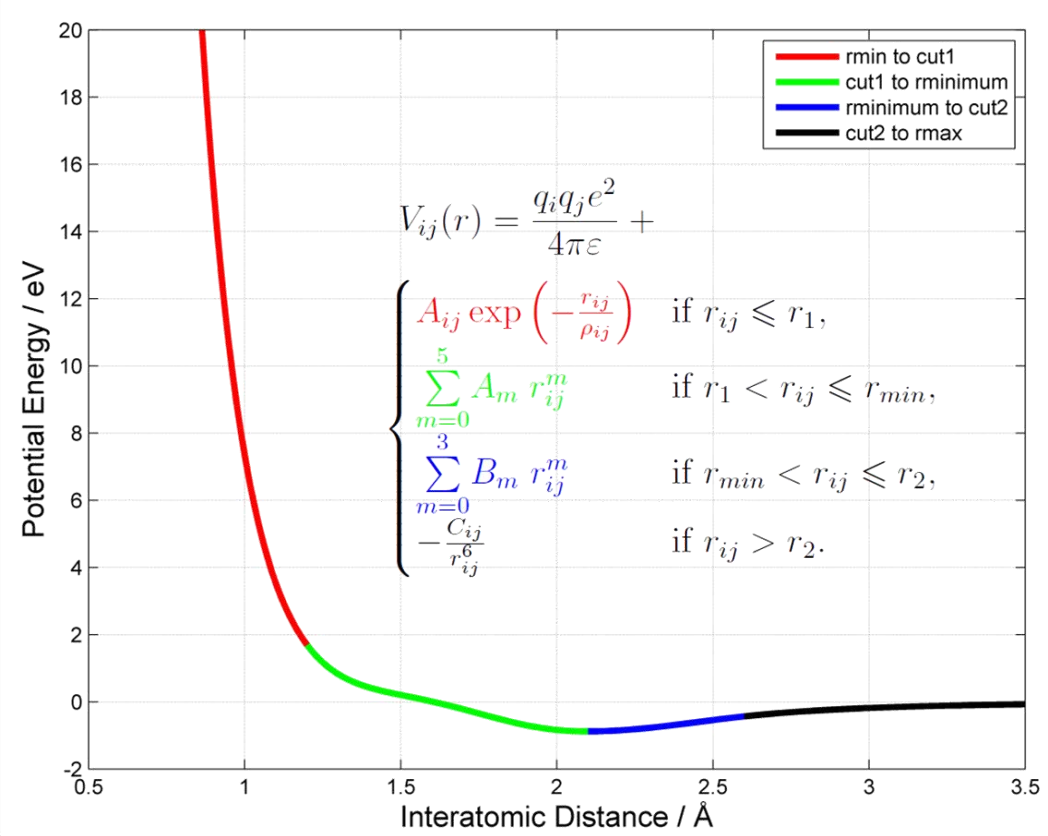

Figure 2.5: Plot showing the ranges in which the Buckingham four-range potential is applied.

The short range and long range interactions can be illustrated graphically (shown in figure 2.6). The plot shows how the potential energy changes with atomic

distance for the short range and long range interactions. The two interactions can also be combined to form an overall sum which is defined as the lattice energy.

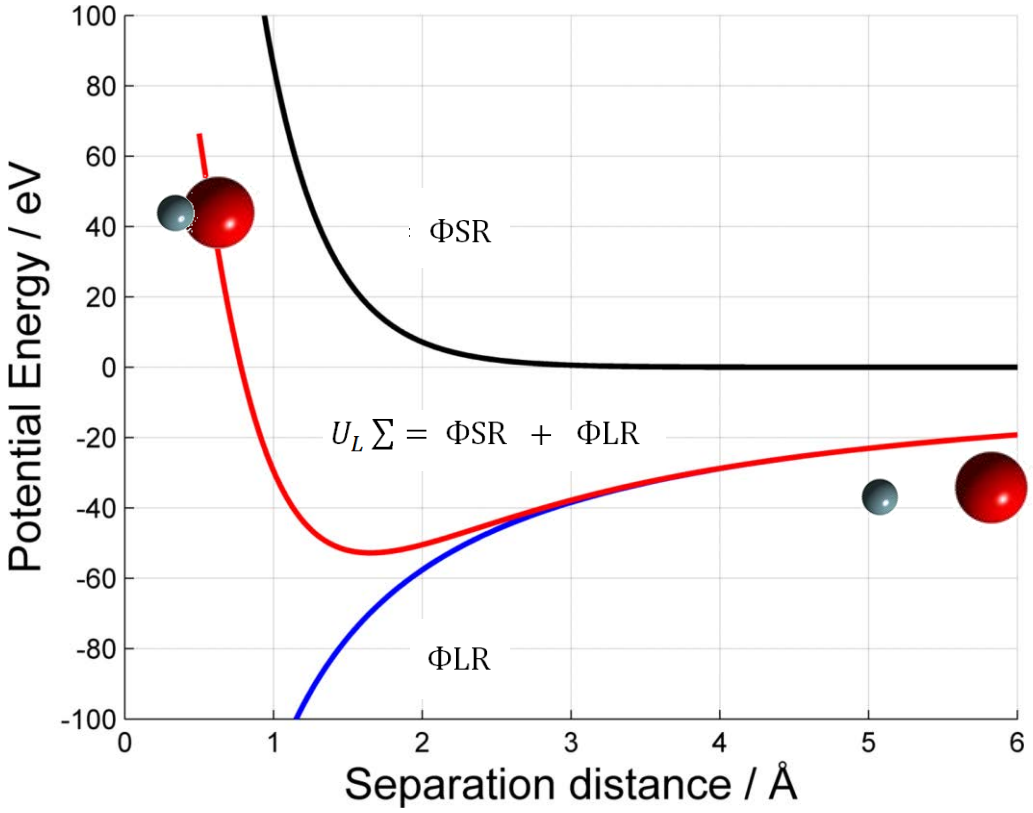

Figure 2.6: A plot illustrating the short range repulsion, coulombic interaction and the total energy of the interactions combined.

2.3 The shell model

In order to model the perfect and defected system correctly we must consider the polarizability of the atoms involved is considered. This is especially important when considering the effects of charged defects on the system.

Previously the rigid ion model has been used which does not account for the polarizability of the system. Although the rigid ion model has been successful in modelling some properties of the material it has not been able to sufficiently model other important properties such as dielectric constants, defect properties and phonon frequencies.

The shell model, derived by Dick and Overhauser [36], has been consistently successful in modelling the polarisability of many systems. The model considers the atom to consist of a massive charged core surrounded by a massless shell. The charge on the core is represented by *X* and the charge on the shell, *Y*. The shell and core are coupled together by a harmonic spring that has a force constant, *k*. Therefor the overall formal charge on the atom is represented by the charged on the core and the shell added together, *X*+*Y*.

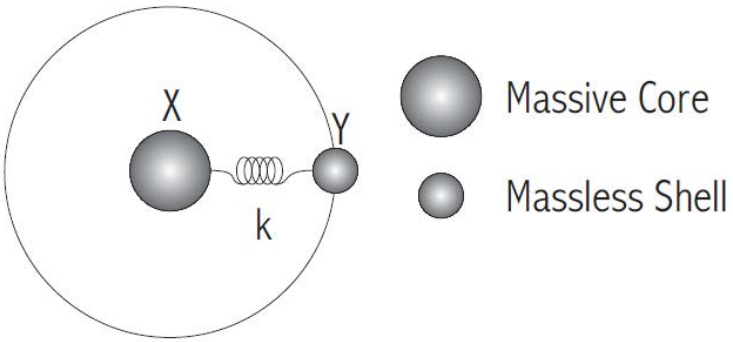

Figure 2.7: Representation of the shell model.

2.4 Static calculations

The term ‘static’ is used to describe the conditions under which the simulations are carried out; the Collins dictionary defines the term static as something that does not move or change. In computational simulations static calculations do not account for lattice vibrations or most forms of lattice entropy. This is beneficial as the ions are then stationary so are able to represent unique lattice positions within the structure.

2.4.1 Introduction to GULP

The methodology applied within this investigation is the same as that used by Read and Jackson [25] and all of the calculations used were embodied within the GULP code. Previously discussed lattice energy minimisation methods were used throughout to obtain information about the structure and energy of the material when the atomic coordinates and lattice parameters are relaxed. This will represent the interactions with the total internal energy at zero Kelvin.

The General Utility Lattice Programme (GULP) is a computational programme that was originally designed to derive interatomic potentials for various chemical systems. Today GULP is still widely used to derive interatomic potentials but has expanded significantly in its capabilities. The programme now has many applications including energy minimisation, structure manipulation and defect calculations. GULP has been widely used to investigate properties of a wide

range of materials from fuel cells and battery materials [37- 39] to nuclear materials [40].

2.4.2 Energy minimisation

When simulating any material the structural parameters must be adjusted in the initial stages to give the lowest energy configuration. This provides the most stable arrangement of the ions within the crystal and therefore the most stable structure. If calculations were not performed at this minimum the structure would be of higher energy and therefore much less stable. A number of minimisation algorithms are available but the most widely used ones are based on a gradient technique [41] in which the first derivatives of the energy functions of the structural parameters are used. The conjugant gradient method is a first-order algorithm that gradually changes the ionic coordinates of the system until a minimum is reached. This method takes a step approach towards the minimum point and can show oscillatory behaviour within the steepest descents but not within more narrow wells and therefore may not be able to find the lowest energy configuration. A more time consuming but more specific method is the Newton-Raphson method. This is a second-order method in which the first and second derivative of the energy function is used which can provide more information about the shape and curvature of the function itself. In order to find the minimum energy configuration within the least computational time, a combination of both of these methods is used with the conjugant gradient method being first followed by the Newton-Raphson method.

2.4.3 Defect calculations

Defects within any system will cause the surrounding system of the crystal to be disturbed. The disturbance is mainly due to coulombic interactions between the lattice ions and the defect. When investigating the effects of defects within a structure we must not only consider the defect itself but also the atoms that surround the defect. These surrounding atoms must be considered as they are included when the lattice relaxes around the defect. The Mott-Littleton method [42] employs the two region approach in which the material is separated into two parts; the inner region (region1) and the outer region (region 21 and 2b). A schematic of this approach is shown in figure 2.8.

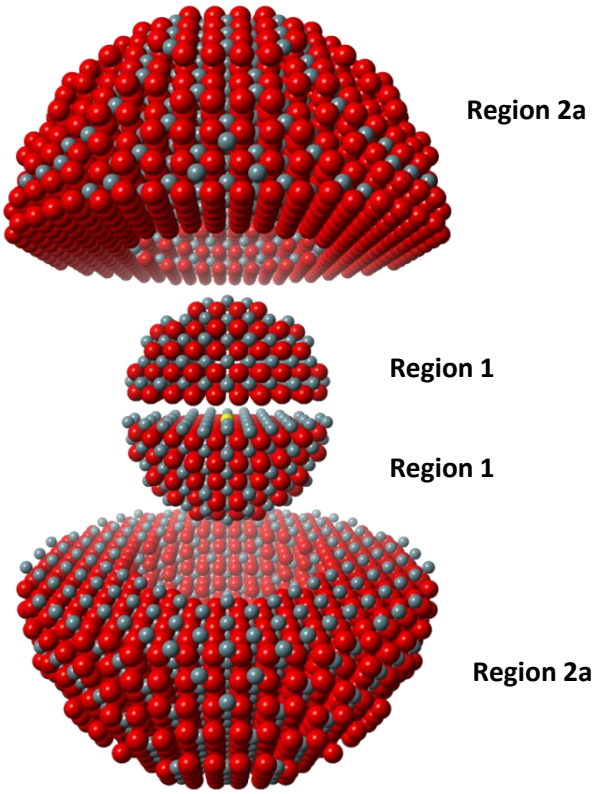

Figure 2.8: Illustration of the Mott-Littleton method of modelling defects.

Sourced from M.S.D.Read [25]

In the inner region (region 1) the atoms are strongly affected by the presence of a defect. The interactions between the ion pairs within region 1 are calculated using the specific interatomic potentials. It is important that the atoms within this region are relaxed until all of the atoms are at zero force; this causes the interactions between the atoms to become equal.

The outer region is split into two sections; region 2a and region 2b. The affects in the outer region are relatively weak as it is a further distance from the defect; the atoms in section 2b are considered to interact with any net charge on the defect and are treated as a dielectric continuum. The atoms within region 2a are weakly affected by the defect, more than region 2b but less than those in region 1. The Mott-Littleton approximation can describe the polarisation that occurs within the outer region from the effects caused on the inner region.

2.4.4 Mean field and supercell approach

Performing simulations using a repeated single unit cell allows us to use the symmetry of the cell, space group and therefore the perfect crystal structure of the cell which will allow an in depth look at many properties of the system. However, the mean field approach can also prevent difficulties such as partial occupancy of lattice sites upon doping of the material. This may be advantageous for producing an average energy for different defects but is not suitable when calculating small percentages such as 1% doping. A way to overcome this is to generate a supercell; a supercell is a periodic repetition of unit cells.

The generation of a supercell will allow a single point defect to be modelled more accurately as each ion is treated as a single ion and there is no partial occupancy.

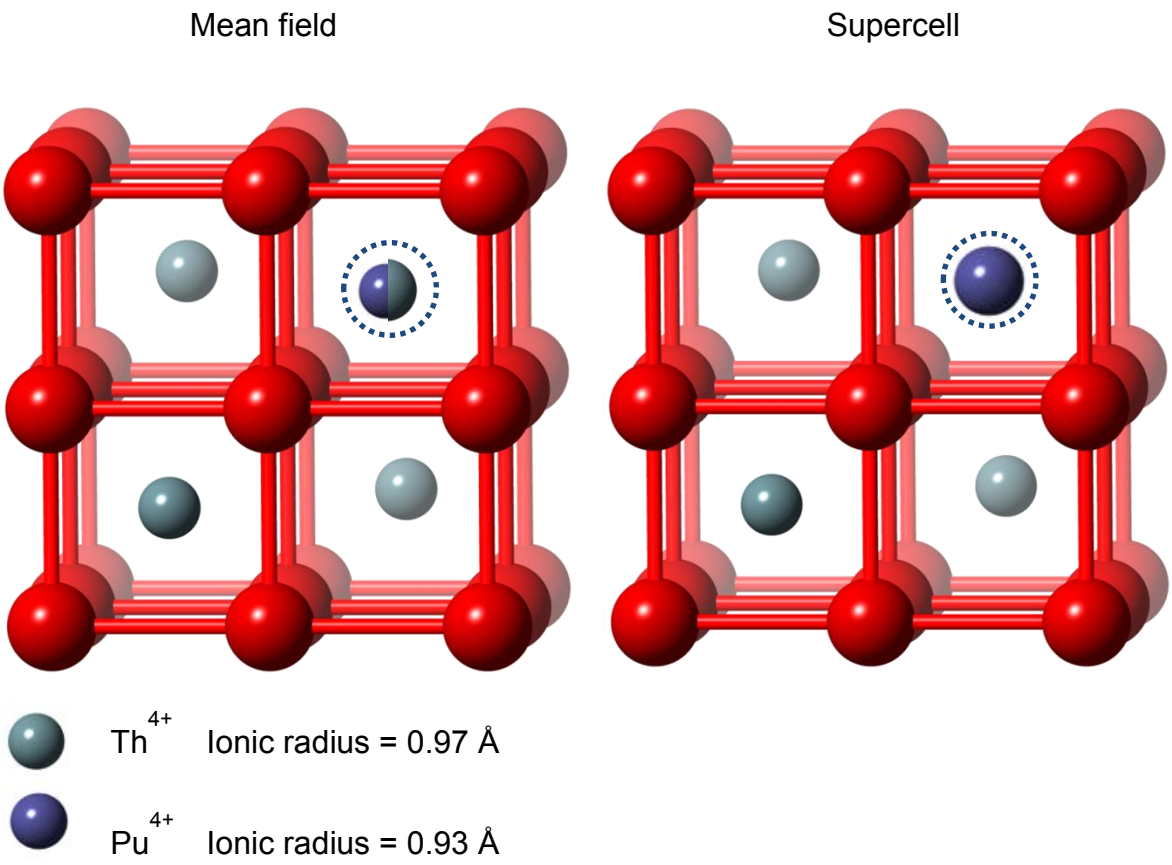

Figure 2.9: Illustration of 25% plutonium doping in the ThO_2 unit cell and supercell.

2.4.5 Free energy

The GULP code allows free energy calculations to be made in which the free energy of the system is minimised at given temperatures. The free energy is calculated from a combination of properties including the lattice energy and the entropy, in combination to form the equation for Gibbs free energy. This method is beneficial to use complimentary to MD simulations as it includes Gibbs free energy minimisation methods and takes into account factors that occur at lower temperatures such as zero point motions. These are factors that are ignored in high temperature MD simulations. Free energy calculations performed using the GULP code are viable to use as a starting point but must be treated with caution as the calculations can be sensitive to a number of factors; for example potentials with a short cut off distance can cause difficulties within the calculations due to the physical changes in structure or configuration that are produced by short cut off distances. The methods used within GULP to simulate free energy apply a quasi-harmonic-approximation [53] which assumes that the atoms within the system are vibrating purely harmonically.

2.5 Surface simulations

2.5.1 Introduction

The surface of a material is vital and essential area to study in order to gain an in depth look at the behaviour and characteristics of the material itself. Many of the reactions that take place happen on the surface and it is these reactions that account for many of the properties of the material itself.

Previous bulk simulations carried out throughout this work can be utilised within surface calculations but only to a certain extent as there will be many differences. In reality surfaces are not perfectly uniform; they may contain ledges or steps and in order to get a more realistic idea of the characteristics of the surface we must study them as they truly exist.

One of the first publications investigating surfaces was by Tasker et al in 1979 [43] who studied the stability of some ionic crystal surfaces including rock salt and fluorite crystals. Over the years the simulations involving surfaces have become more advanced with some of the later studies detailing the effects of temperature, pressure and the introduction of defects on the surface and the resulting effects on structure as a whole. There are few codes available to simulate surfaces including METADISE and MARVIN [44].

All of the surface simulations within this study were carried out using METADISE. This code was originally published by Watson et al in 1996 [45] and has since then been used in many surface simulations for many different applications [46, 47].

The interatomic potential sets used within the atomistic simulations performed in GULP can be transferred to METADISE without the need for adaption.

2.5.2 Perfect surfaces

In order to obtain an in depth understanding of the surface of a material we must first study the perfect surface; that without defects due to foreign atoms, temperature or pressure. Modelling the surface of a material involves cutting the unit cell at the miller index of interest for the space group of the system. The cuts are then investigated further to find the valid repeating units of the specified index. Valid cuts are cuts that do not produce a polar surface, these are the most real life surfaces as they are the lowest energy and therefor most valid surfaces. Polar surfaces can also be studied using METADISE but for the purpose of this study only the non-polar surfaces were investigated.

The surface unit is considered to be a stack of planes parallel to the surface that is periodic in two dimensions. This unit is then split into two regions. This approach is similar to the Mott-Littleton approach used in GULP in that the region surrounding the surface is split into two; region 1 and region 2. Region 2 is then split further into region 2a and 2b (see figure 2.10). Region 1 is the closest to the surface and is therefore relaxed explicitly. The sizes of the regions are modelled in such a way that none of the atoms in region 1 are affected by the atoms in region 2.

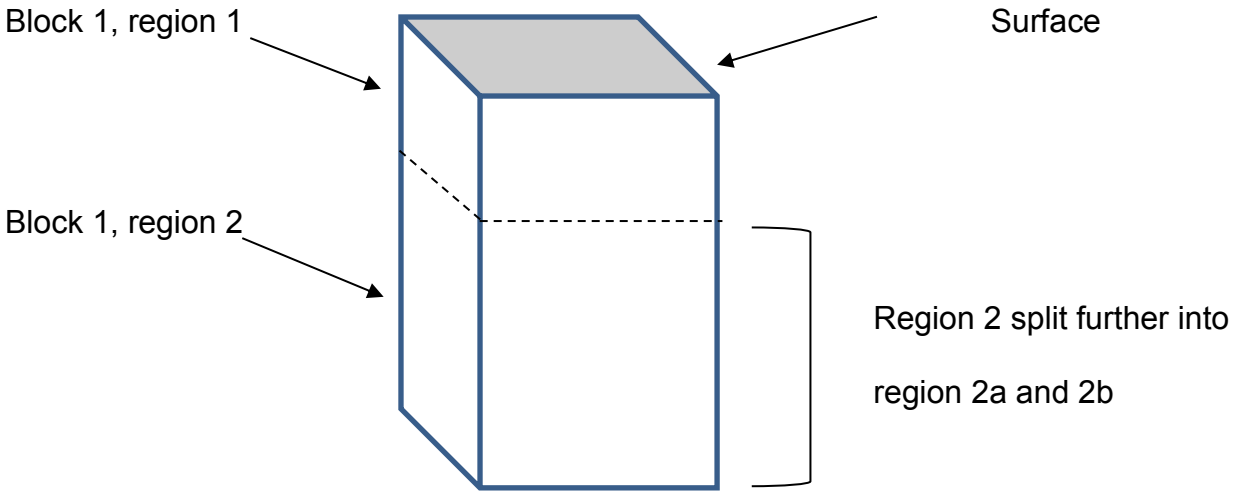

Figure 2.10: Figure showing the surface unit with regions 1 and region 2. Region 2 is split further into region 2a and 2b.

A surface is created when a cut is made at this surface that splits two blocks apart at an interface (shown in figure 2.11).

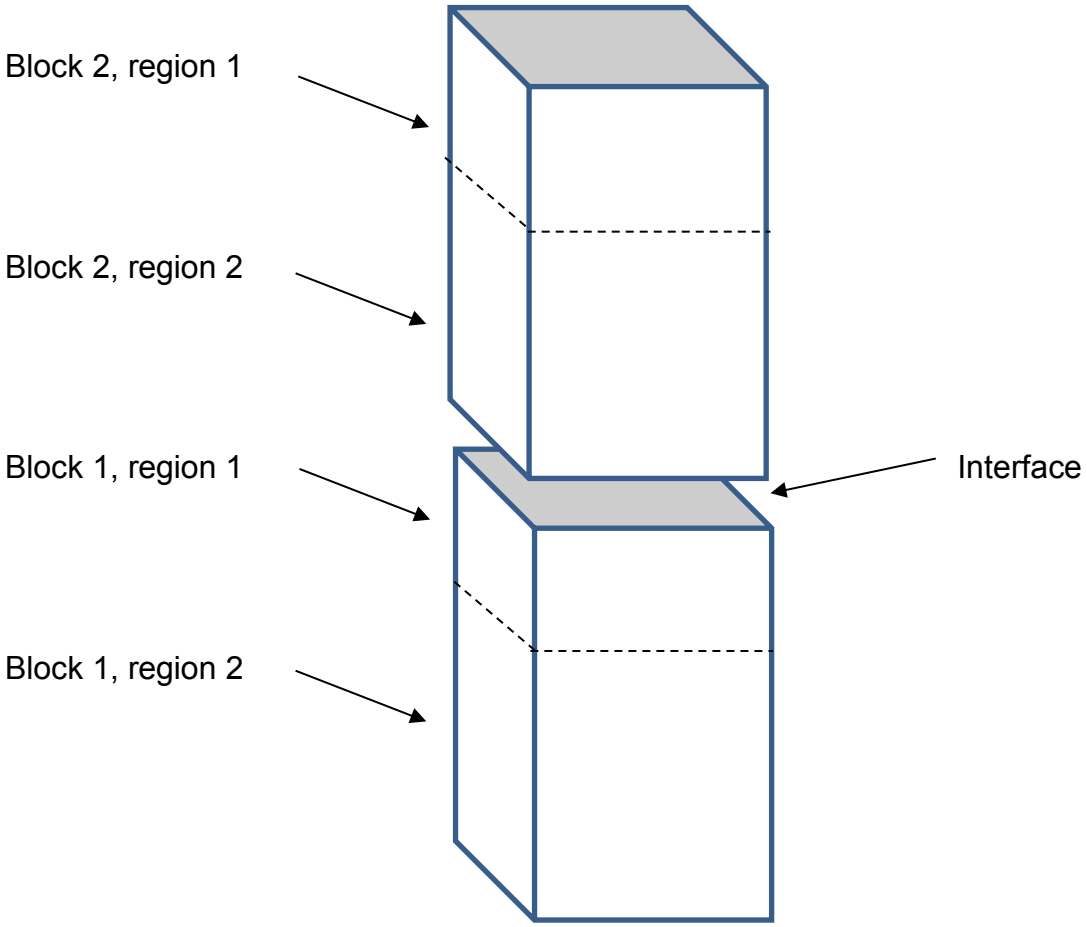

Figure 2.11: Figure showing how a surface is formed when a block is cut at the interface at the end the second block region 2.

Tasker et al [43] concluded that there are three types of surfaces (figure 2.12) that can be produced from making the cuts; each surface is considered as a stack of planes but it is the arrangement of the planes that determines the types of surface. Type I surface has planes that have alternating anions and cations and therefore no overall charge on the plane. The type II surface has stacked planes that are made up of the same charged particle and therefore each plane carries

a charge. The repeating unit of the planes overall, though, has no charge as the planes are stacked in a repeating symmetrical unit. Type I and II surfaces have no dipole perpendicular to the plane. Type III surface is the only surface that has a dipole perpendicular to the plane. The surface is arranged as alternating stacks of charged planes which cause an overall dipole at the surface.

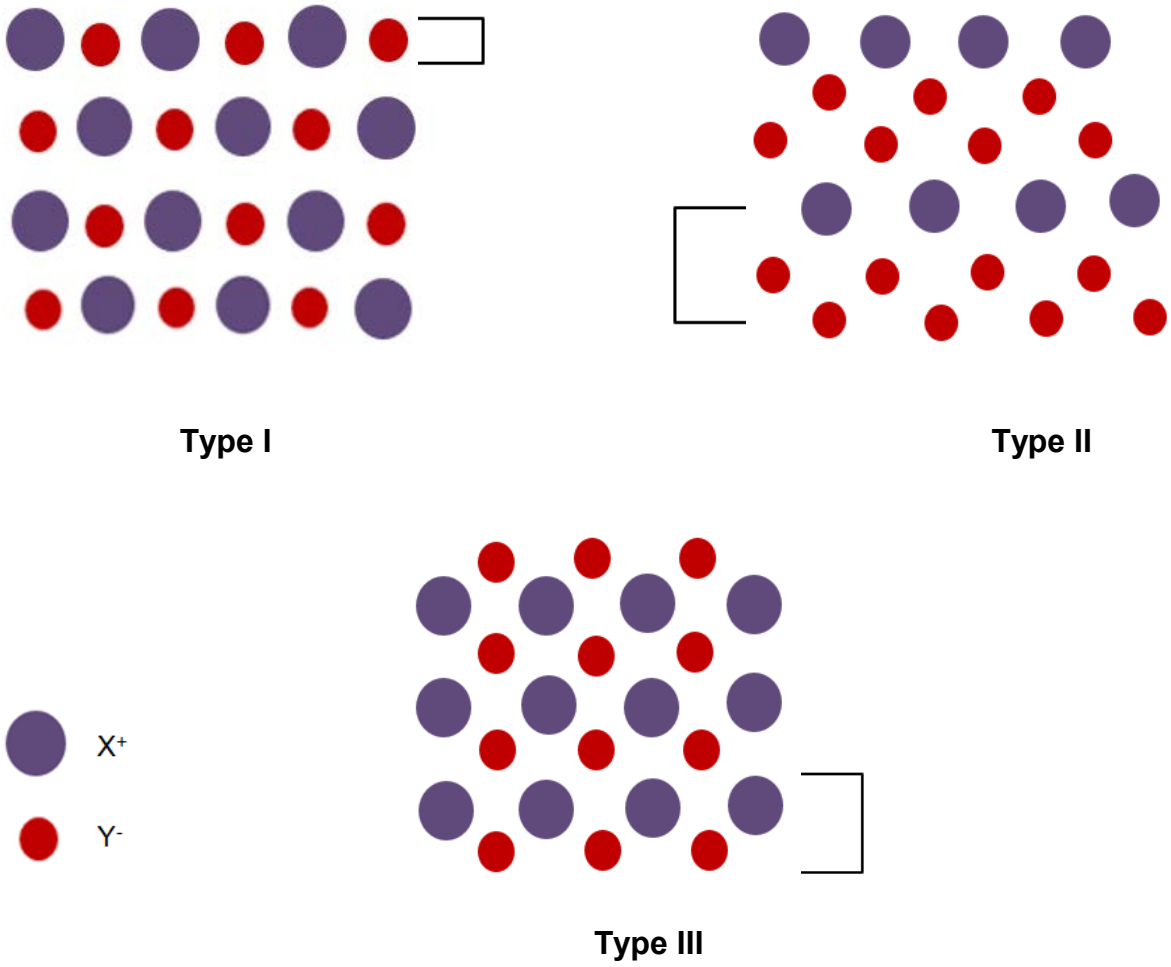

Figure 2.12: the three types of surfaces determined by Tasker et al. Type I and II have an overall neutral charge and no dipole moment perpendicular to the surface. Type III has an arrangement that causes a dipole perpendicular to the surface.

Once a valid cut has been determined the surface is then relaxed using energy minimisation methods to obtain a variety of information including surface energies and attachment energies. This provides a suitable starting structure for further defect calculations.

2.5.3 Surface energies

Surface energy is the most vital component required when modelling a surface; the surface energy tells us the energy per unit area needed to transform a bulk region into a surface region. The surface energy can be represented as the difference in energy between the bulk and the surface over the area of the surface as shown in figure 2.13.

$$Surface\ energy = \frac{\mathrm{E_{surf}} - \frac{1}{2}\mathrm{E_{bulk}}}{\mathrm{A}}$$

Figure 2.13: Equation to show the surface energy where A is the area of the surface area in question and E_{surf} and E_{bulk} are the energies of the regions.

The energy of the bulk is considered to be half that of the surface due to the number of atoms in the bulk being twice that of the surface.

Surface energy is a kinetic quantity and can be calculated directly through METADISE calculations in the perfect surface. A small, positive value indicates a stable and therefore favourable surface. One a surface energy is obtained it can be used to model a number of things including the morphology of the material.

2.5.4 Attachment energy

The attachment energy is defined as the energy released when a new layer of thickness is added to the surface. This method assumes bulk termination of the surface and is therefore not as reliable as the surface energy. The attachment energies can also be used to predict morphologies of the material that, although not entirely satisfactory, can back up the model when comparing to experimental values.

2.5.5 Crystal morphology

The morphology of a system is one of the surface simulations that can be compared to experimental work. It predicts the structure of the material in terms of surface coverage with the lowest energy indexes dominating the structure. The morphology can be simulated using the calculated surface energies or the

attachment energies. The surface energies will provide a structure with the highest percentage of coverage coming from that of the lowest energy index. The attachment energies will predict a structure with the highest percentage coverage with the index with the lowest attachment energy and therefore easiest surface to add to.

Wulf [48] and Gibbs [49] also worked on the theory that the morphology of a system was directly related to the lowest energy surfaces and this theory has been used successfully in predicting the morphology of many materials for many applications [50-52].

2.5.6 Defective systems

The method of the incorporation of defects into a crystal surface is similar to the two-region approach taken when simulating bulk properties (see section 2.4.3).

The defects must first be introduced into the surface of the material and defect energies calculated. Segregation of the defect to the surface of the bulk can then be determined by comparing the defect energy at the surface to that of the bulk.

2.6 Molecular dynamics simulations

2.6.1 Introduction

The simulations described so far have been sufficient in modelling the materials at zero Kelvin but have not yet been able to accurately model any significant temperature effects. Modelling the effects on the material under high temperatures is essential when looking at what goes on within the reactor core; the fuel will be exposed to temperatures above 1000°c and we must understand how this will affect the characteristics of the material. The molecular dynamics technique embodies within the DL_POLY code calculates the forces between the ions within the crystal and allows the computational progression of the motion of these ions to be simulated. Molecular dynamics simulations can provide a detailed illustration of the how the system evolves over time under a variety of different conditions.

2.6.2 Molecular dynamics methodology

Molecular dynamics techniques rely upon a robust potential model that is able to be taken forward into more complex mechanical calculations. This will allow details of the thermodynamics of the system to be modelled when exclusive temperature affects are applied. The molecular dynamics technique introduces a kinetic term as well as a potential term which allows the simulation of ion motion and temperature effects. Within the programme Newton's equations of motion

are essentially integrated to provide successive configurations of the system. The resulting positions and velocities of the system can then be identified at various time intervals.

At the start of any calculation a time step, ΔT, is specified, This time step must be smaller than any time step of an important process within the system for example, a femtosecond (10^{-15} seconds). The interatomic potentials are then used to calculate the force F_1, acting on a particle of mass m_1, in order to generate a value for the position X_1 and velocity V_1 at each time step thereafter. Figure 2.14 show how these values are calculated.

$$x_1(t + \Delta t) = x_1(t) + v_1(t)\Delta t$$

$$v_1(t + \Delta t') = v_1(t) + \frac{F_1}{m_1}(t)\Delta t$$

Figure 2.14: Equations used to calculate the velocity of a particle in molecular dynamics simulations.

Initial ion positions, X_1, are those used in the static simulations formulated from the crystal data. The initial ion velocities are obtained by random selection from a Maxwell-Boltzmann distribution at the temperature required. The Maxwell-

Boltzmann distribution will provide a probability of an ion having a certain velocity in the direction *X* at a temperature *T*.

Equilibration time is the time needed at the start of any MD simulation for the system to reach a thermodynamic equilibrium state. It is vital that the system reaches this equilibrium before any calculations begin. The equilibrium stage is normally assigned a time step of up to 10 picoseconds depending up on the individual simulation. Following the equilibrium stage the simulation can take place, usually in time periods of 1 nanosecond. As the simulation proceeds the positions and velocities of the ions are updated for each time step where the interactions of the ions with each other can be integrated to provide the total force upon that ion. The accelerations of the ions are then calculated from these force values and combined with the position and velocity of that ion at each time step.

2.6.3 Periodic boundary conditions

Employing the correct boundary conditions allows us to investigate the macroscopic properties of a material only using a small number of ions. This has many benefits with the main one being computational time. The application of periodic boundary conditions to a supercell creates an unbound system and eliminates any surface effects. It also ensures that the number of ions within the simulation box stays constant by replacing any ions that leave the box with an identical ion with the same trajectory. An illustration of the period boundary conditions applied is shown in figure 2.15.

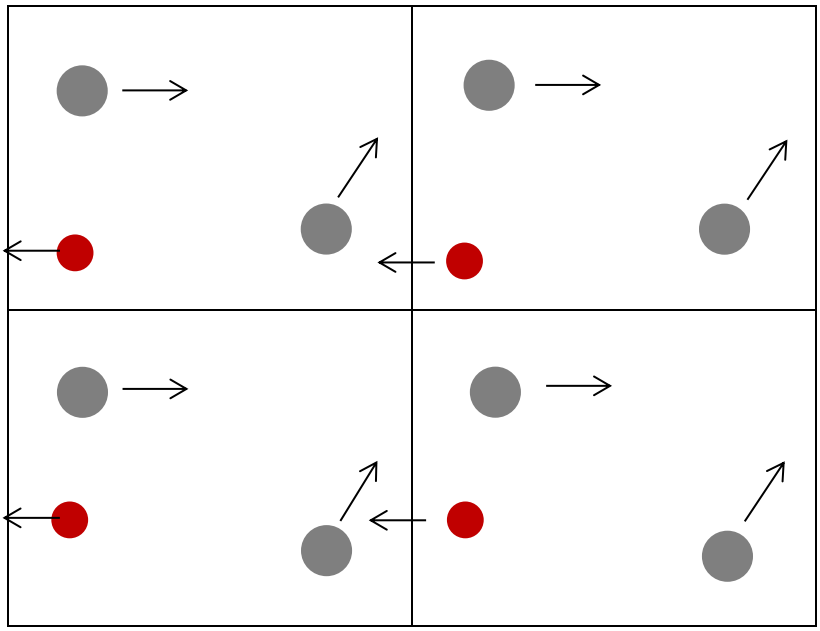

Figure 2.15: Illustration of the periodic boundary conditions within an MD simulation.

Molecular dynamics simulations can be carried out under a number of ensembles [54-57]. Ensembles state the conditions of the simulation and tend to consist of three components. The most commonly or traditional is the NVE ensemble in which the number of ion, *N*, the volume of the system, *V,* and the energy of the system are all constant. If the energy of the system is not kept constant then there can be an exchange of energy between the system and its surroundings which may or may not be beneficial depending upon the calculation. There are a number of other ensembles that can be used including NPT [55], NVT, NST ensembles where *T* represents temperature, *S* represents entropy and *P* represents pressure.

2.6.4 Shell model molecular dynamics

Incorporation of polarisability into molecular dynamics simulations is done through the dynamic shell model, a method originally derived by Fincham et al [58]. The abiabatic shell model is encoded within the DL-POLY code and works on the principles of assigning a fraction of the atomic mass (x) to the shell in order to permit a dynamical description of the overall ion. In a similar way to the shell model mentioned in section 2.3, the ion consists of a core and shell that are connected by a harmonic spring. However, in this method careful consideration must be made with regards to the partitioning of the core and shell; the frequency of the harmonic spring must be above that of the frequency of vibration of the whole ion. This is essential for the core-shell unit to maintain a constant state of net polarisation.

2.6.5 Information from molecular dynamics

A vast amount of useful information about a material can be obtained from a molecular dynamics simulation as it allows the generation of detailed configurations and dynamics of a system to be connected with time. Two of the most valuable properties however are radial distribution function (RDF) and mean square displacements (MSD). The radial distribution function describes how atoms or ions within a system are packed around each other; the probability of finding the centre of a particle a given distance away from the centre of another particle is calculated and a radial average is generated. For a perfect crystalline solid, the RDF plot will have sharp well defined peaks as the atoms are fixed in

their lattice positions. Liquids do no have this ordered fixation of lattice positions and therefore the RDF has more broad undefined peaks. As the structure of the material changes through various conditions such as high temperatures or doping for example, the RDF plots will also change. Mean square displacement is a measure of how the position of a particle deviates from a reference position over time. In a perfect lattice a particle will oscillate about its lattice position allowing a mean MSD value to be found. Defective systems however can show the movement of particles away from the reference positon; sometimes particles may migrate throughout the lattice resulting in the value of the MSD increasing over time.

Chapter 3

Derivation of Enhanced Interatomic Potentials

Contents

3.1 Thorium Dioxide Interatomic Potentials

3.1.1 Introduction

Within this section, two potential derivation methods are described. Method 1 is that derived and previously used by Read et al. to derive potentials for both UO_2 [25] and PuO_2 [59]. The method uses available experimental data do derive an initial solution set that fits to crystal data. The solution set is then taken forward and fit to elastic constants and then dielectric properties. This method will be used to developed a Th-O potential. Method 2 is a Monte-Carlo type python code that was derived by the Read group. It also fits to available experimental data but uses a weighting least square fit to different factors that can be specified by the user. These factors can include crystal data such as lattice constants or bulk properties such as bulk modulus or elastic constants. This method will be used to derive a Gd-O potential.

3.1.2 Literature review

Computational and experimental studies of thorium dioxide have been plentiful since the 1950s with studies including crystal properties such as lattice parameters and lattice energies, elastic properties including bulk modulus and elastic constants and also studies as to how the material will react under pressure, temperature and radiation using XRD, neutron diffraction and many other techniques.

Within this section, literature that has simulated the ThO_2 structure computationally has been considered. Interatomic potential parameters describing the Th-O interaction that have been derived from the literature are listed in Table 1.2 and potentials derived from existing UO_2 potentials are listed in Table 1.3.

One of the first papers to evaluate the interatomic potentials of the ThO_2 model was by Benson et al. [60], where the rigid ion model was used to derive a set of interatomic potentials to calculate properties including elastic, cohesive and surface energies. As is the case with Mackrodt et al. [61] and Colbourn at al. [62], who also studied ThO_2 computationally, derived interatomic potentials but no potentials were published within the literature. Mackrodt et al. also used the rigid ion model to derive potentials for a number of crystals including ThO_2, MnO and NaCl, which were then used to investigate the lattice constants, cohesive energies and also energies for the given materials. Colbourn et al. used their derived potentials to study the defect structures within thorium dioxide extensively, providing useful figures including lattice energies, defect energies and elastic constants. They also doped the ThO_2 crystal with different ions such as magnesium and barium to look at how these defects effect ion conductivity.

Many authors used the shell model to represent their materials including Clausen et al. [63] and Nadeem at al. [64]. Clausen used elastic neutron scattering to determine phonon energy dispersions of both ThO_2 and CeO_2 and then used this experimental data to construct a set of potential parameters for each of the materials. Both the shell model and the rigid ion models were used to simulate the crystal. The parameters were published within the paper in the form of

Elcombe and Pryor [65]. The authors found that for ThO_2, the rigid ion model gave only a reasonable fit for the parameters and the best fit was obtained using the shell model. Nadeem et al. aimed to derive interatomic potential's for binary oxides including ThO_2, SnO_2 and ZrO_2, and test the reliability of the potentials by comparing calculated defect energies and crystal properties with experimental data.

Other methods have also been used to study the interatomic potentials of ThO_2 including molecular dynamics; Osaka et al. [66] investigated gadolinium-doped thoria using MD simulations. The authors derived their own interatomic potentials for the thorium and gadolinium that included a set of Morse potentials. Changes in the lattice parameter of the crystal were considered with changes in gadolinium concentration and various temperature ranges. Oxygen diffusion coefficients were also investigated within the doped material.

H. Y. Xiao et al. [67] studied ThO_2 along with CeO_2 and ZrO_2 from an *ab initio* molecular dynamic perspective. This research studied the behaviour of the materials under low energy recoil events and determined a number of properties including threshold displacement energies and defect configurations.

The most recent paper to investigate ThO_2 potentials using molecular dynamics is by Martin et al. [68], where Th-O and O-O Buckingham potentials from Catlow et al. [69] were used to investigate pure thoria and uranium doped thoria. They investigated properties such as thermal expansion and heat capacity. Cywinski et al. also studied thorium using molecular dynamics to investigate the rate of conversion of fertile thorium to fissile uranium in different fuel rod geometries [70].

One of the most informative papers related to derived Th-O potentials is the review paper by Bahera et al. [71] which discusses two sets of existing thoria potentials [14, 66] and potentials derived from a number of UO_2 oxygen potentials, including those determined by Tharmalingham [72] and Walker [73]. The authors develop and discuss potentials they derived using the rigid ion model. The review paper aims to compare the potentials by comparing them directly with each other, as well as experimental data. Potentials are listed within the literature along with properties such as bulk modulus, elastic constants and defect energies. Literature that has provided some information about calculations from their own potentials may not have listed all the properties required for the in depth comparison of this paper, such as defect energies of elastic properties for example, so the authors have calculated them using the potentials given. The experimental papers used as a comparison range significantly in their year of publication; the literature used for the cell parameters is from 1956 (S.M. Lang [74]) when there are many other papers that have published cell parameters more recently such as Idiri et al [75]. Experimental literature used as comparisons for this paper and also other computational papers have been considered within this review.

Potentials	Nadeem [15]	Osaka [66]	Martin [68]
Charge			
Th core	4.64	2.4	4
Th shel	-0.64	/	/
O core	0.513	-1.2	-2
O shell	-2.513	0.0	0.0
O-O Buckingham			
***A* /eV**	25.41	2346.1488	22764.0
***P* /Å**	0.6937	0.32	0.149
***C* /eV Å^6**	32.32	17.33936	27.88
***D* /eV Å^8**	0.0	0.0	0.0
Th-O Buckingham			
***A* /eV**	8638.5	61.4295	1144.6
***P* /Å**	0.2856	0.57	0.3949
***C* /eV Å^6**	70.0	0.0	0.0
***D* /eV Å^8**	0.0	0.0	0.0
Th-Th Buckingham			
***A* /eV**	0.0	17.0261	0.0
***P* /Å**	0.0	0.82	0.0
***C* /eV Å^6**	0.0	0.0	0.0
***D* /eV Å^8**	0.0	0.0	0.0
Th-O Morse			
***D* /eV**	0.0	1.215	0.0
***Bij* /Å^{-1}**	0.0	1.9	0.0
***r*ij* /Å**	0.0	2.36	0.0

Table 1.2: Interatomic potentials derived for ThO_2.

It must be noted that within the above table of potentials the cation-cation interactions are only predicted for use in molecular dynamics simulations. They are not needed for static calculations as there is no chance of an interaction

between neighbouring cations. This implies that the authors intend to use the potentials for more detailed calculations; only Osaka [66] and Basak [76] quote Morse potentials and both of these papers are molecular dynamic simulations. They both study semi-ionic systems and describe the terms within the Morse potential as a way of identifying the shape and depth of the potential.

Quantum mechanical methods such as density functional theory are also a very popular way of predicting mechanical properties of materials but their results must be approached with caution; they do not rely on the derivation of interatomic potentials and this, in turn, has consequences on the reliability of the results especially when concerning larger atoms with 5f electrons. Research that has used DFT to study thoria includes Y. Lu et al. [78], Kanchana et al. [79], P.J Kelly et al. [80], H.Y. Xiao [81] and Boudjemline [82].

P.J. Kelly (1987) used DFT to calculate a range of properties including bulk modulus and cohesive energies for a collection of actinide dioxides including ThO_2. H. Y. Xiao studied ThO_2 in terms of the diffusion of elements including bromine and caesium into the ThO_2 and CeO_2 structures.

DFT methods have also been frequently used to investigate thermodynamic properties of ThO_2 and doped derivatives of ThO_2. Y. Lu et al. [78] used DFT to study the thermodynamic and structural properties of thoria including defect formations and diffusion of helium into the structure. They calculated such properties as the bulk modulus, specific heat capacity and thermal expansion coefficients. This paper has been used as a comparison paper in literature from

Martin et al. [68] for values of thermal expansion coefficients. Lu et al. used the work of Boudjemline et al. as a reference for comparison of values for elastic and optical properties calculated within the research; Boudjemline uses DFT to study the dependence of pressure on various properties of the CeO_2 and ThO_2 crystals.

The importance of comparing calculated results with experimental values is essential as it gives an idea as to whether the computational findings are reliable or not; the potentials must be able to model the crystal structure and bulk properties accurately. Many of the computational papers have used experimental data to either fit the parameters or to check if the parameters are reproducing adequate values for crystal properties, defect properties and so on. The experimental papers considered in this have been used as references within any of the discussed literature and have been compared to the values calculated within this work in table 1.7.

When considering potential parameters Behera at al. [71] is a very important paper to consider as it provides an assessment of the calculated potentials by comparing them to a number of experimental papers including Iridi et al. [75] and Olsen et al. [84] Idiri et al. investigated ThO_2 and UO_2 under pressure using x-ray diffraction and were therefore able to give experimental results for compressibility factors, bulk moduli and changes in structural parameters. Olsen et al. also studied ThO_2 using XRD but specifically focused on the bulk modulus of the material. Other experimental papers that use XRD to investigate crystal properties of ThO_2 include Momin et al. [85] and Baghat et al. [86]

Potentials	Tharmalingham1[72]	Tharmalingham2[72]	Walker [73]	Lewis [69]	Karakisidis [83]	Basak [76]	Arima1 [77]	Arima2 [77]
Charge								
Th core	4.0	4.0	4	4	4	2.4	4	2.7
O core	-2.0	-2.0	-2	-2	-2	-1.2	-2	-1.35
O-O Buckingham								
***A* /eV**	-93.3	36.1	5029.34	22764.3	11272.6	1633.6666	22517.53	919.17
***P* /Å**	0.398	0.382	0.15285	0.149	0.1363	0.32702	0.149	0.332
***C* /eV Å^6**		16.85	72.65339	112.2	134	3.95063	27.59	17.36
***D* /eV Å^8**		11.86	0	0	0	0	0	0
Th-O Buckingham								
***A* /eV**	2207.565	1896.302	1379.866	1978.75	1042.528	1081.0004	1594.996	27166.11
***P* /Å**	0.369615	0.37396	0.398673	0.38774	0.408121	0.33059	0.393955	0.224857
***C* /eV Å^6**	36.715	0.31	49.22	244.941		0	73.96	12.8
***D* /eV Å^8**	257.96	42.63	0	0	1042.528	0	0	0
Th-Th Buckingham								
***A* /eV**	0	0	8.5215	/	/	11464.0507	9.815	/
***P* /Å**	0.398	0.382	0.16666	/	/	0.15984	0.315062	/
***C* /eV Å^6**	170	244.18	1530.173	/	/	0	2593.118	/
***D* /eV Å^8**	20370.45	31974.16	0	/	/	0	0	/
Th-O Morse								
***D* /eV**	/	/	/	/	/	1.00879	/	/
Bij /Å^{-1}	/	/	/	/	/	1.60473	/	/
r*ij /Å	/	/	/	/	/	2.369	/	/

Table 1.3: table of interatomic potentials from the Bahera et al. review paper

Maceado et al. [87] specifically studied the elastic constants of single crystal thoria at 25°C. This is a very valuable paper as it is the only experimental paper that lists results for the elastic constants.

J. D. Axe et al. [88] was used as a reference paper by the ThO_2 review paper by Bahera et al. specifically using the values created for the static dielectric constant and the high frequency dielectric constant. Infra-red spectroscopy was used to study the infrared dielectric dispersion of uranium dioxide and thorium dioxide. There are not many values predicted for the static dielectric constant as you need the shell model to predict it and most of the literature uses the rigid ion model to obtain the parameters.

M. Ishigame [89] also used spectroscopy to study ThO_2 but they used Raman spectroscopy to obtain values for phonon energies of the material. This paper has also been used as a reference paper in the review paper by Bahera et al. M. Sarsfield et al. [90] also studied ThO_2 using Raman spectroscopy. R. Agarwal et al. [91] also studied ThO_2 experimentally but using high temperature calorimeters to investigate the heat capacity, enthalpy increment and thermal conductivity of pure ThO_2 and uranium doped ThO_2. S. Dash et al. [92] also used high temperature calorimeters to study the thermodynamics of the pure and uranium doped ThO_2 system using three temperature ranges: 127-305K for the pure system, and 305-845K and 891-1698K for the uranium doped system.

K. Bakker et al. [93] produced a critical evaluation of available thermodynamic data for ThO_2 and its mixed fuel derivatives by comparing the results produced

for heat capacity measurements, oxygen potentials, thermal conductivity and linear thermal expansion. In this review, the work of Springer et al. was found to be in disagreement with the other literature compared.

3.1.3 The anion-anion potential

The anion-anion potential used throughout this work is that of Catlow and Jackson et al. [94] This potential has previously been used successfully in modelling some binary oxides [69], UO_2 [25] and ThO_2 [83]. It can be used for the ThO_2 system as the thorium dioxide crystal is isostructural to UO_2. The atoms also have the same coordinate positions so can be considered to be in the same environment. The potentials are shown in table 1.4.

Interaction	**A /eV**	***p*/Å**	**C /eVÅ^{-6}**	**Y |e|**	**K_2 /eVÅ^{-2}**
O- O	11,272.6	0.1363	134.0	-4.4	296.2
	r_{min} /Å	**Cut 1 /Å**	**r_{min} /Å**	**Cut 2 /Å**	**r_{max} /Å**
	0.0	1.2	2.1	2.6	15.0

Table 1.4: Buckingham four range potential set for the anion-anion interaction, Y is the charge on the ion, K_2 is the spring constant and r_{max} is the cut-off point.

3.1.4 Methodology

As the Buckingham four-range potential cannot be applied to the cation-anion potential due to the absence of a stationary point within the function, the C term must be set to zero so that the unphysical attractive forces at short distances can be avoided. This provides a Born-Mayer form of the potential in which only the A and *p* terms are used to describe the material.

The derivation process assumes no prior starting values and begins with the screening of a set of A and *p* parameter values against lattice parameter. The solution set will show the combinations of the potentials *A* and *p* that will give the lattice constant closest to the observed value. Figure 3.0 shows the plot of lattice constant against A with the solution set shown in red.

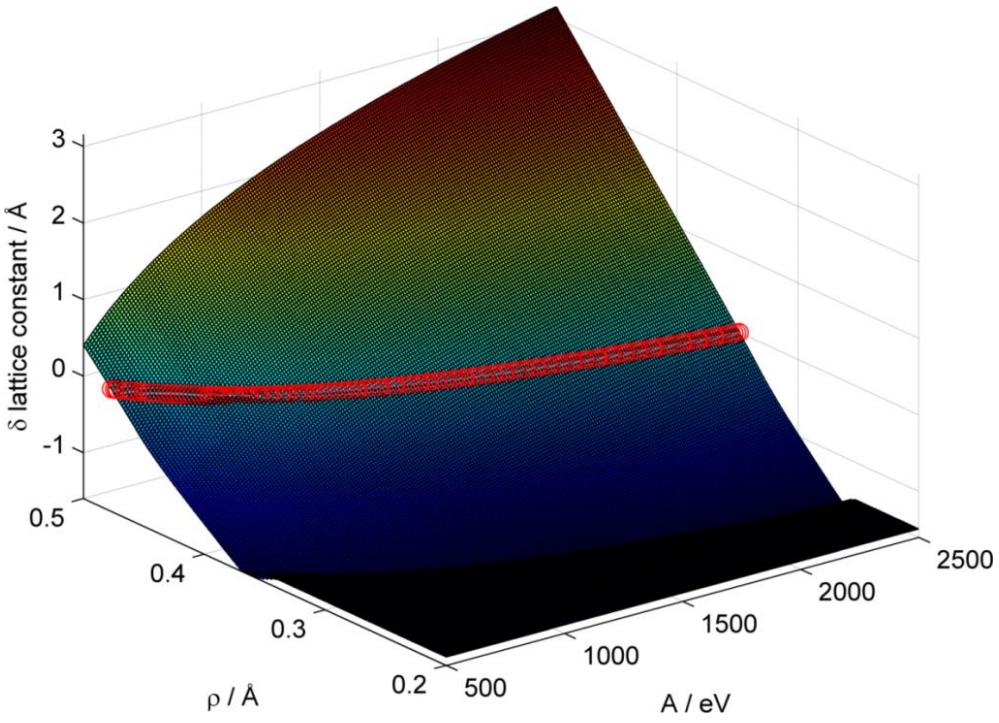

Figure 3.0: Surface plot representing the difference between the A and *ρ* and the observed Th-O lattice constant.

This method will produce a number of combinations that exactly reproduce the crystal structure. This set of is then screened once again to fit to bulk properties; elastic constants are used as they describe the response of the lattice with respect to deformation of the material. As the material is cubic symmetry reduces the unique elastic constants to C_{11}, C_{12} and C_{44}. Figure 3.1 shows a plot of the elastic constant value against the A parameter.

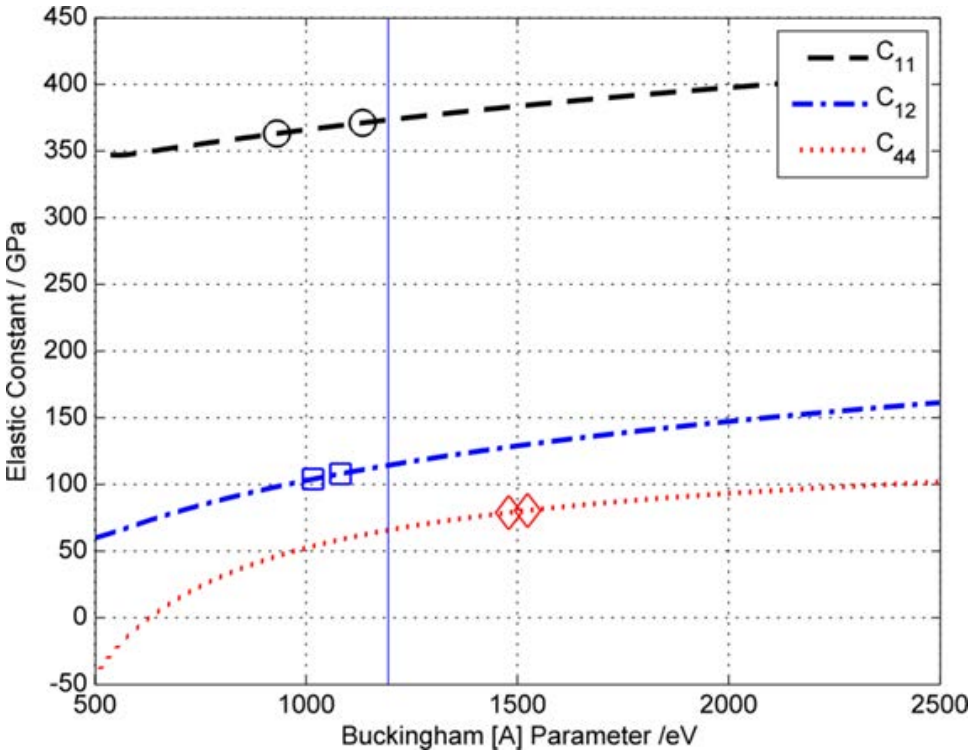

Figure 3.1: Predicted and experimental elastic constants plotted against the potential parameter (A).

Three initial sets of potentials were produced, each with different fits to the elastic constants. Set 1 was fitted using a least squares difference to all three of the elastic constants, set 2 was fit to just C11 and C12 and set 3 used an unweight mean approach to fit to all three of the constants. The three initial sets are shown in table 1.5.

	A /eV	*p* /Å	C /eVÅ^{-6}	Y |e|	K_2 /eVÅ-2
Set 1	1394.4724	0.3861	0.00	-2.54	91.9415
Set 2	1047.7387	0.4078	0.00	-2.54	129.5660
Set 3	1193.9986	0.3975	0.00	-2.54	105.7408

Table 1.5: Three sets of Buckingham potentials for the thorium cation-anion interaction.

In order to select a set of parameters to carry forward a least squares approach was used to fit across the range of elastic constants. The next step involved adjusting the spring constant to fit the dielectric properties of the material. This is so that the potentials will simulate the material and its polarisability accurately when calculating defect properties within the structure. This is shown in figure 3.2, which also shows the available experimental values.

This procedure provided a potential set that accurately described the lattice parameters (Δ0.0%) bulk properties, and dielectric properties (Δ 4.5—6%) of the material. The potential set is shown in table 1.6 and has then been taken forward for validation and used in simulation of defect properties and free energy calculations in chapter 4.

Interaction	A *(eV)*	*P (Å)*	C *(eVÅ^{-6})*	Y *(|e|)*	K_2 *(eVÅ^{-2})*
Th-O	1193.9986	0.3975	0.0	6.54	105.7408

Table 1.6: The derived potential for the Th-O interaction where Y is the shell charge and K_2 is the spring constant.

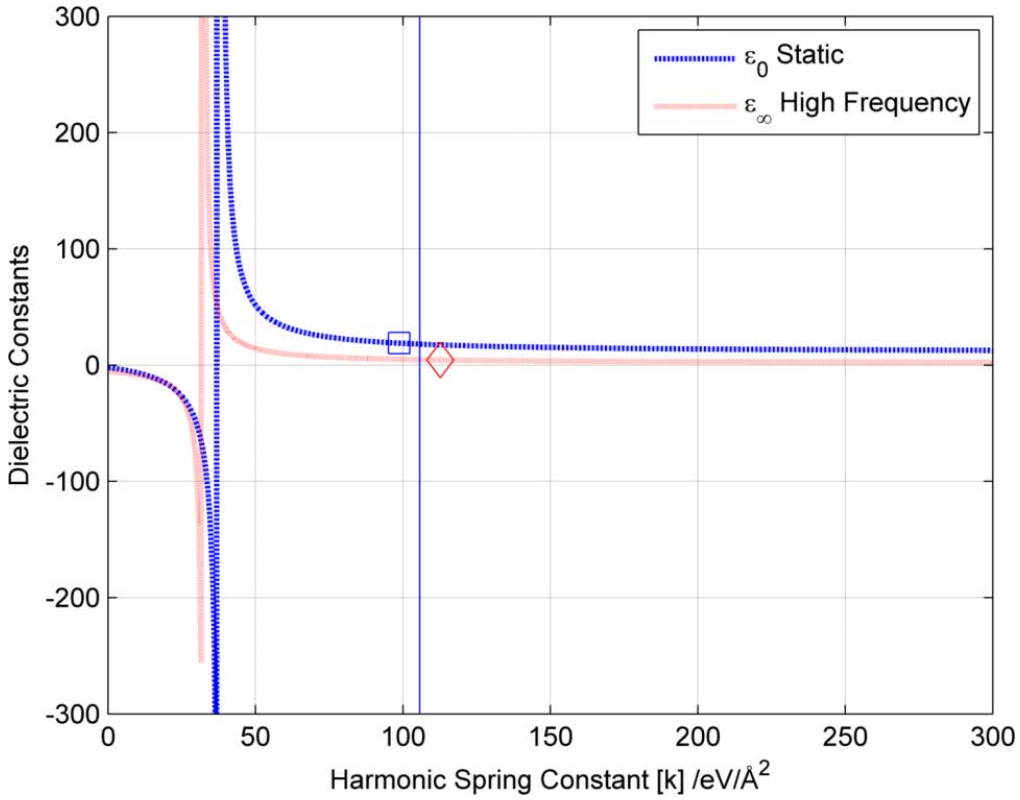

Figure 3.2: Dielectric constants as a function of the spring constant, K_2.

3.1.5 Validation of interatomic potentials

Thorium dioxide has the cubic fluorite structure with the thorium atoms occupying the face centred position and oxygens at the tetrahedral sites.

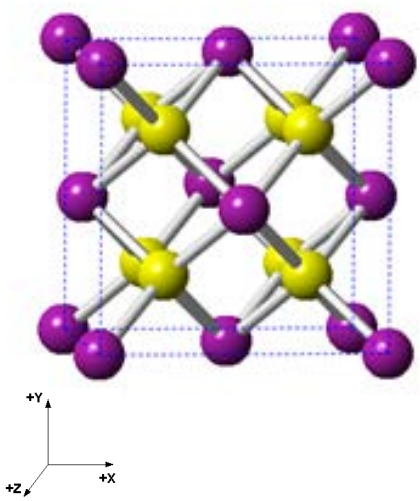

Atom	Oxidation state	X	Y	Z
Thorium	+4	0.0000	0.0000	0.0000
Oxygen	-2	0.2500	0.2500	0.2500

Figure 3.3: ThO_2 unit cell at atom coordinates [75]

The bulk properties of the material calculated using the potential derived was compared with experimental values (shown in table 1.7). There is excellent agreement over the range of properties shown. This proves that the potentials are robust and can be used with confidence for further calculations.

Property	Observed	Calculated	% Difference
Lattice constant (Å)	5.6001	5.6001	0
Lattice energy (eV)	-104.64	-100.33	4.11
Elastic constants /Gpa			
C_{11}	367 ± 4.0	373.23	-1.69
C_{12}	106 ± 2.0	114.36	-7.92
C_{44}	79.7 ±0.8	65.82	17.44
Moduli			
Bulk	193	200.65	-3.96
Shear	95.6-100.6	81.93	14.30
Youngs	256,270	319.58	-24.84
Poissons Ratio	0.22	0.23	-6.64
Dielectric constants			
Static	18.9	18.1	4.23
High frequency	4.4	4.7	-6.82
Phonons at 298K			
L mode	269.2/279	271.37	-0.81
T mode	569.8/567	425.48	25.33

Table 1.7: Comparison of calculated and experimental bulk properties.

3.2 Gadolinium oxide interatomic potentials

3.2.1 Introduction

Gadolinium has been of interest for many years as it has the highest neutron cross section of any other natural element. This intriguing property has caused it to become of interest in many areas including cancer research [95] and nuclear technology [66].

If a material has a high neutron cross section it means that the interaction between the target nucleus and an incoming neutron is favourable and it relies on many factors including the energy of the incident neutron and the type of target atom. Gadolinium is well known as a 'fuel poisoner' due to this high neutron cross section. Free within a nuclear fuel, it will absorb the neutrons needed for the fission reaction to occur and ultimately stop the reaction. Usually this would be highly unfavourable but if used correctly the waste gadolinium fuel produced in the nuclear process can be used to control the speed of a fission reaction in the form of a control rod. Control rods can be inserted or removed from the reactor accordingly.

Incorporating gadolinium into the pure ThO_2 and mixed Thoria fuels will allow simulations of real conditions within a reactor core when gadolinium impurities are present.

3.2.2 Literature review

There are four sets of interatomic potentials (shown in table 1.8) currently published that describe the interactions between gadolinium and oxygen atoms within the Gd_2O_3 system. Catlow et al. [69] derived sets of potential models for a number of ionic oxides including Gd, Hf and Th. They use three different derivation methods within their work with the Gd-O potential being derived by fitting the structural information to the parameters. They assume that the cation-anion interaction is in the Born-Mayer form, which is in agreement with our work, but the potential set that they derive is in the rigid ion form.

Bush et al. [96] again derived a number of potential sets for some binary and ternary oxides including Gd_2O_3. They fit the potentials to available experimental lattice properties using a least squares method in which the difference in crystal structure, relative permeabilitys and elastic constants are considered. The potentials are derived using the shell model with a good fit to the lattice parameter (0.29%) and lattice energy (0.0%).

Grimes at al. [40] also derived a set of potentials that described the Gd-O system [97] but the most advanced investigations using a derived set of potentials are by Osaka et al. [66]. They investigate the molecular dynamics of gadolinium doped thoria using a range of temperatures from 298 to 1200K. The defect structures of the doped material and their effects upon the lattice parameter are considered along with diffusion coefficients of the oxygen ions within the material.

Potentials	Catlow [69]	Bush [96]	Grimes [40]	Osaka [66]
Charge				
Gd core	3.00	-0.973	3.00	1.8
Gd shel	-	3.973	-	-
O core	-2.00	0.04	0.513	-1.2
O shell	-	-2.04	-2.513	-
Gd-O Buckingham				
***A* /eV**	1336.8	866.339	1885.75	9218.1595
***P* /Å**	0.3551	0.3770	0.3300	0.08
***C* /eV Å^6**	0.0	0.0	20.34	0.0
***D* /eV Å^8**	0.0	0.0	0.0	0.0
Spring constant				
K_2 /eV Å^{-2}	-	299.96	-	-

Table 1.8: Interatomic potentials derived for Gd_2O_3.

S. Yamanouchi et al [99] studied the material experimentally investigating the effects on melting temperature of UO_2 fuel pellets when doped with gadolinium. They found that at less than 2% gadolinium there was no change in melting temperature. F. X. Zhang [102] also studied Gd_2O_3 experimentally determining the phase transitions of the material at high pressures using X-ray diffraction.

There have already been many studies of the effects of doping nuclear fuels with gadolinium including that of Matthews et al [100] and those already mentioned [66, 68]. Matthews et al used various experimental methods to investigate the

phase relations and linear thermal expansion of cubic solutions of $Th_{1-x}M_xO_{2-x/2}$ in which M = Eu, Gd and Dy.

3.2.3 Methodology

Using a Monte-Carlo type python code developed by the Read group a set of Gd-O potentials were derived through fitting to the available experimental data which, unfortunately due to limited experimental work, only includes the lattice parameter reported by Pires et al [101] and the Bulk modulus from Zhang et al [102]. The bond distances were also generated from Gulp using the available experimental data and then used in the fitting procedure. The shell charge and spring constant were that used by Bush et al [96] and they remained constant throughout the derivation process.

An initial starting potential was required to begin the scan, the ThO_2 potential described within this work was used and the scan started from there. A range of *A* parameter from 500 to 4000eV and *p* parameter from 0.1 to 0.5Å were used.

The code used a weighted least squares method in which the percentage differences of the properties to the experimental data are weighted differently to each property. This was specified by the user at the time; for the Gd_2O_3 potential the weighting factor was highest for the lattice constants with a weighting factor of 50. A weighting factor of 6 was used for the bulk modulus along with a weighting factor of 2 for the bond lengths. The number of runs and cycles per run was also specified by the user, in this case there were 10 runs with 2000 cycles

per run. This means that for each run 2000 moves were made resulting in 2000 areas being sampled.

$$LSq_w = \alpha \sum (y_{l\ calc} - y_{l\ exp})^2 + \sum_j \beta_j \sum \frac{1}{y_{j\ exp}} \left(y_{j\ calc} - y_{j\ exp}\right)^2$$

Figure 3.4: equation used to describe the least squares method within the Monte-Carlo potential fitting code. α and β are the weighting factors for the lattice parameters and other experimental data respectively.

There was also an exception factor included within the code. The exception factor used in this case was 0.1 which means 10% of the unfavourable moves are accepted and become the new reference state.

This method produced a set of Gd-O potentials that fit well to the lattice constants (0.047%), bond lengths and bulk modulus (1.52%). The potentials were then taken forward for further validation and used in bulk, defect and free energy simulations. The interatomic potential derived are shown in table 1.9.

Interaction	A *(eV)*	*P (Å)*	C ($eVÅ^{-6}$)	Y *(|e|)*	K_2 ($eVÅ^{-2}$)
Gd-O	2962.90599	0.31441	0.0	3.973	299.96

Table 1.9: Interatomic potential for the Gd-O interaction where Y is the shell charge and K_2 is the spring constant.

3.2.4 Validation of interatomic potentials

Pires et al [101] used XRD and Rietveld refinement methods to determine the crystal structure of Gd_2O_3. They quote a lattice constant of 10.722 Å and coordinate positions for two gadolinium atoms and one oxygen position shown in figure 3.5.

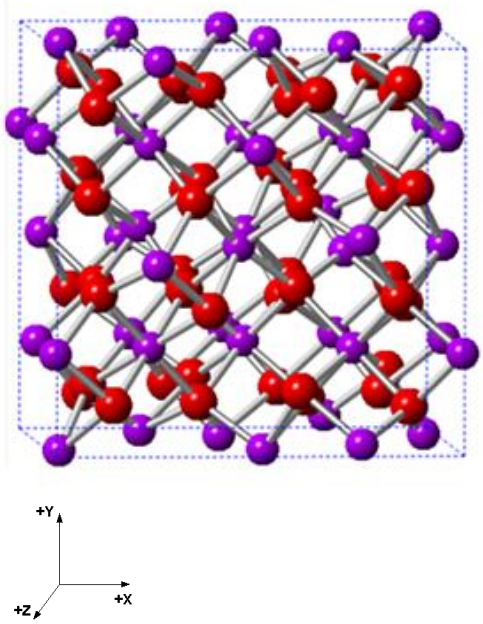

Atom	Oxidation state	X	Y	Z
Gadolinium 1	+3	0.0000	0.0000	0.0000
Gadolinium 2	+3	0.2824	0.0000	0.2500
Oxygen	-2	0.0982	0.3590	0.1255

Gadolinium

Oxygen

Figure 3.5: Gd_2O_3 unit cell with the body centred cubic arrangement. Space group Ia-3 (206) and the corresponding atom coordinates.

The bulk properties of the material calculated using the potential derived were compared with literature and experimental values where possible (shown in table 2.0). There is excellent agreement over the range of properties shown. This proves that the potentials are robust and can be used with confidence for further calculations.

Property	Observed	Calculated	% Difference
Lattice constant (a_0) /Å	10.722 [71]	10.727	0.047
Lattice energy /	-	1087.144	-
Elastic constants /GPa			
C_{11}	-	260.225	-
C_{12}	-	156.193	-
C_{44}	-	90.925	-
Moduli			
Bulk	188.0 [70]	190.871	1.52
Shear	-	72.673	-
Youngs	-	143.05221	-
Poissons Ratio	-	0.37509	-
Dielectric constants			
Static	-	4.779	-
High frequency	-	1.776	-
Bond lengths /Å			
Gd1 – Gd2	3.553	3.528	-0.712
Gd2 –Gd2	3.570	3.544	-0.737
Gd1 –O	2.279	2.285	0.2589
Gd2 – O	2.320	2.283	-1.608
O-O	3.221	3.199	-0.686

Table 2.0: Calculated and literature bulk properties for Gd_2O_3.

3.3 Chapter summary

This chapter has described two interatomic potential techniques that have been used to derive potentials for ThO_2 and Gd_2O_3. The potentials have then been validated using the crystal structure of the material along with the bulk properties.

Both methods have been successful in deriving a set of potentials that correctly fit the bulk properties of the material and have therefore been taken forward to simulate other properties including thermophysical and defect properties.

Chapter 4

Static calculations

Contents

4.1 Introduction

In order to model the pure and defected thoria system a robust set of potentials is required. The derivation method for the interatomic Th-O potentials used within this work is outline in chapter 3 along with the validation of the potentials using bulk properties. Within this chapter the pure thorium dioxide system is analysed in more depth with regards to the crystal structure and bulk properties. Fission products produced within the fuel cycle are then doped into the thorium dioxide structure and various bulk properties investigated. Thermodynamic properties of the pure and doped materials are also predicted with increasing temperature effects. Finally, the pure system is then doped to create a MOX fuel containing either plutonium or uranium. Once doped, bulk properties were then investigated with increasing dopant percentage.

4.2 The pure system

In order to carry out any defect or thermodynamic simulations the correct crystal structure must first be generated. The original crystal structure atomic coordinates were taken from the studies of Idiri et al [75] and combined with the potentials shown in table (1.6) to reproduce the crystal structure shown in figure 4.0.

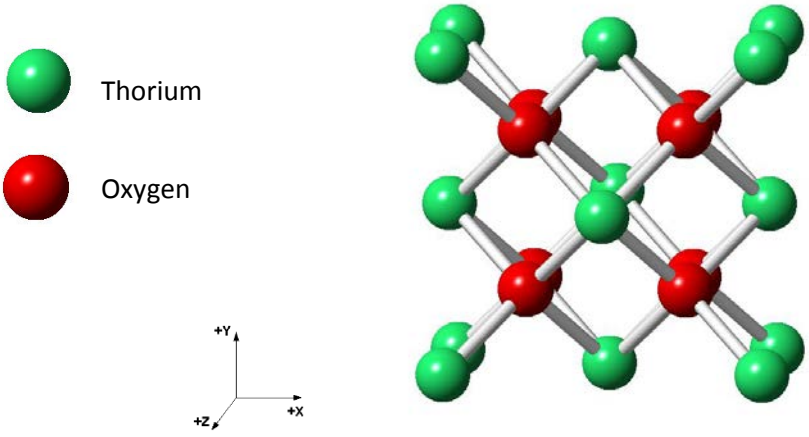

Figure 4.0: ThO_2 unit cell.

4.2.1 Crystal structure and bulk properties

Thorium dioxide has the cubic fluorite structure and belongs to the Fm3m space group. The thorium ions are arranged in a face centred cubic structure whereas the oxygen atoms have a simple cubic structure.

As previously mentioned the thorium fuel requires a neutron source and in industry this is supplied by either uranium or plutonium. The percentage of doped uranium or plutonium within the thorium fuel varies from 5-15%. One unit cell of thorium dioxide contains a total of fourteen thorium atoms and eight oxygen atoms. Therefore it is impossible to model such small concentrations of dopant ions and obtain any reliable results. It is therefore vital that a supercell is generated containing enough atoms for the small concentrations of dopant ions to be investigated and robust results produced. A supercell can be grown in either

direction e.g 1x1x2 but for this study all supercells were grown at equal distances in all directions.

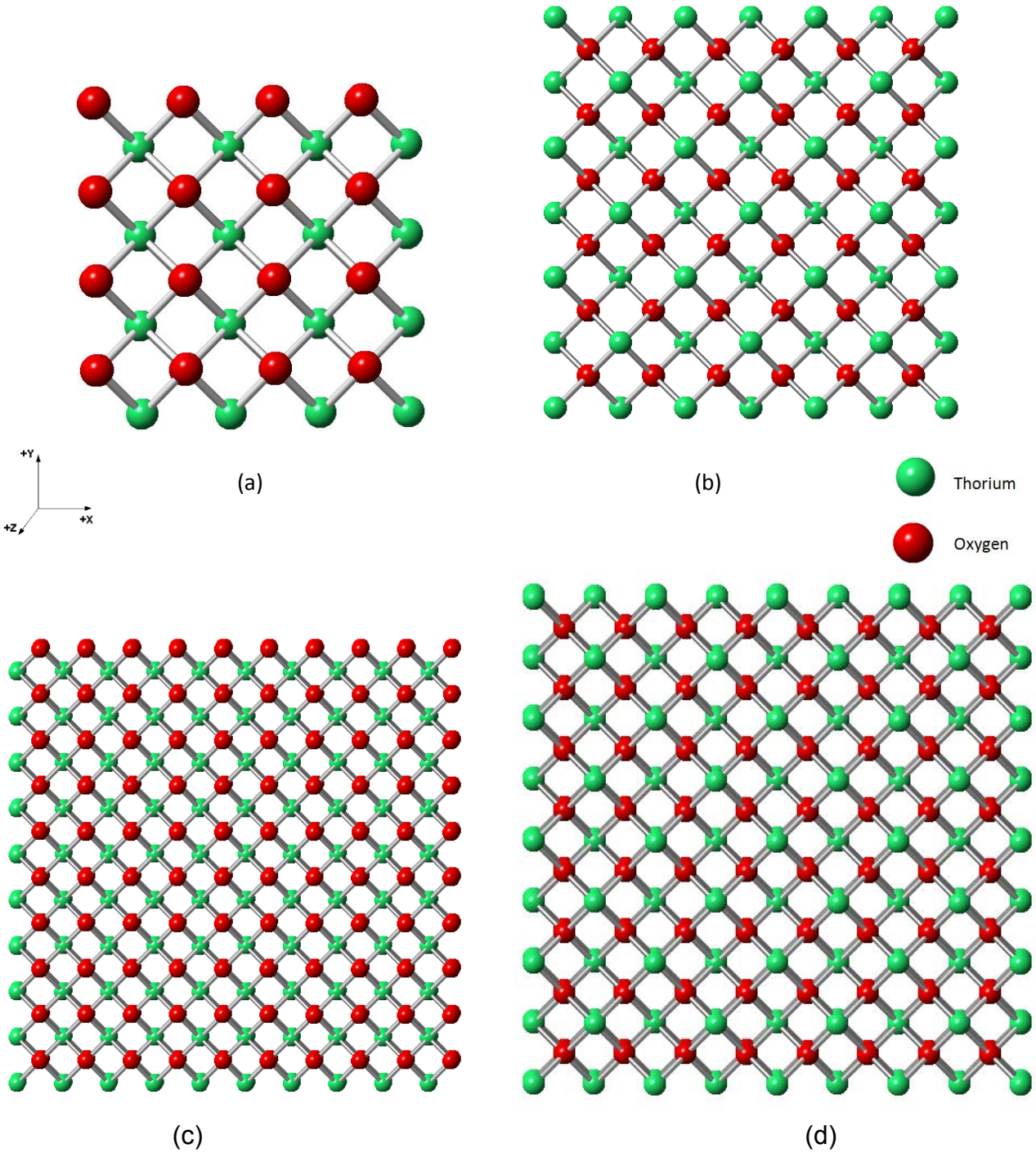

Figure 4.1: Various supercell sizes for the ThO_2 cell. (a) 2x2x2 (b) 3x3x3 (c) 4x4x4 (d) 5x5x5

All of the supercell sizes mentioned above except the 5x5x5 cell were able to reproduce the bulk properties and crystal structures accurately. The 4x4x4 supercell was used throughout the following investigations as it allowed the simulation of many ions with a relatively low computational time. Table 2.1 shows the values for the bulk properties with varying supercell size.

Property (normalised)	**1x1x1**	**2x2x2**	**3x3x3**	**4x4x4**	**5x5x5**
Formula	Th_4O_8	$Th_{32}O_{64}$	$Th_{108}O_{216}$	$Th_{256}O_{512}$	$Th_{500}O_{1000}$
Lattice parameter *(Å)*	5.60	5.60	5.60	5.60	*Unable to optimise*
Lattice energy *(eV)*	100.33	100.33	100.33	100.33	
C11 *(Gpa)*	373.24	373.23	373.23	373.23	
C12 *(Gpa)*	114.38	114.37	114.36	114.36	
C44 *(Gpa)*	65.83	65.82	65.82	65.82	
Bulk modulus *(Gpa)*	200.66	200.65	200.65	200.65	
Shear modulus *(Gpa)*	81.93	81.93	81.93	81.93	
Youngs modulus *(Gpa)*	319.58	319.58	319.58	319.58	
Poisson ratio	0.24	024	0.24	0.24	
Static dielectric constant	18.08	18.07	18.07	18.07	
High frequency dielectric constant	4.67	4.67	4.67	4.67	
Phonons at 298K					
L mode *(cm^{-1})*	271.37	271.37	271.37	271.37	
T mode (*cm^{-1}***)**	425.8	425.8	425.8	425.8	

Table 2.1: Comparison of bulk properties for varying supercell sizes for the ThO_2 cell.

4.2.2 Thermophysical properties

An understanding of the temperature dependant properties of a fuel during irradiation through experimental and computation simulations allows us to predict its behaviour with confidence, which is of vital importance when designing a nuclear reactor and its components. The properties of the fuel including melting point, thermal expansion and thermal conductivity must be accurately known in order to ensure the correct reactor design e.g fuel rods and fuel cladding [103]. Fuel performance and safety analysis can also be determined.

Thorium dioxide has been reported to be more chemically stable than uranium dioxide; it has higher thermochemical conductivity and lower co-efficient of thermal expansion [104]. This coupled to the favourable thermochemical and thermophysical properties of thorium dioxide leads to a better in-pile performance than that of uranium dioxide.

Many properties of the fuel will change upon heating and may change significantly with the introduction of defects. Therefore, it is vital that the thermophysical and thermochemical properties of the fuel are determined for a range of temperatures and defects. Initial thermodynamic simulations of pure and defected system including thermal expansion and heat capacity were run using GULP using the free energy methods mention in chapter 2. The simulations were run within the temperature range of 0-4000K in order to model the fuel under conditions within the reactor core and also conditions just above the fuels melting temperature.

The thermal expansion of the fuel is of the most importance as it leads to many safety issues with respect to fuel swelling and pressure build up. It also allows us to gain an initial idea of the melting point of the material. The melting point of a fuel plays a vital role in determining the operating temperatures of the reactor core and it also limits the

energy that can be extracted from the fuel. Bohler et al [105] studied the melting and solidification behaviour of thorium and its mixed uranium/plutonium fuels using laser heating and found that the addition of thorium to uranium fuel would cause the melting point to increase. These findings are beneficial when we consider the mixed fuel as higher operating temperatures can be used which will increase the fuel performance.

The first steps taken within this research to investigate the thermophysical properties of the fuel included predicting changes to the lattice parameter with temperature change. This also allowed us to determine a preliminary melting point. Figure 4.2 demonstrates the change in lattice parameter with temperature. The lattice parameter shows slight expansion (0.035%) from 1500K to 3750K and then a sudden increase (0.07%). This would suggest that the material has reached its melting temperature and that the lattice has become distorted.

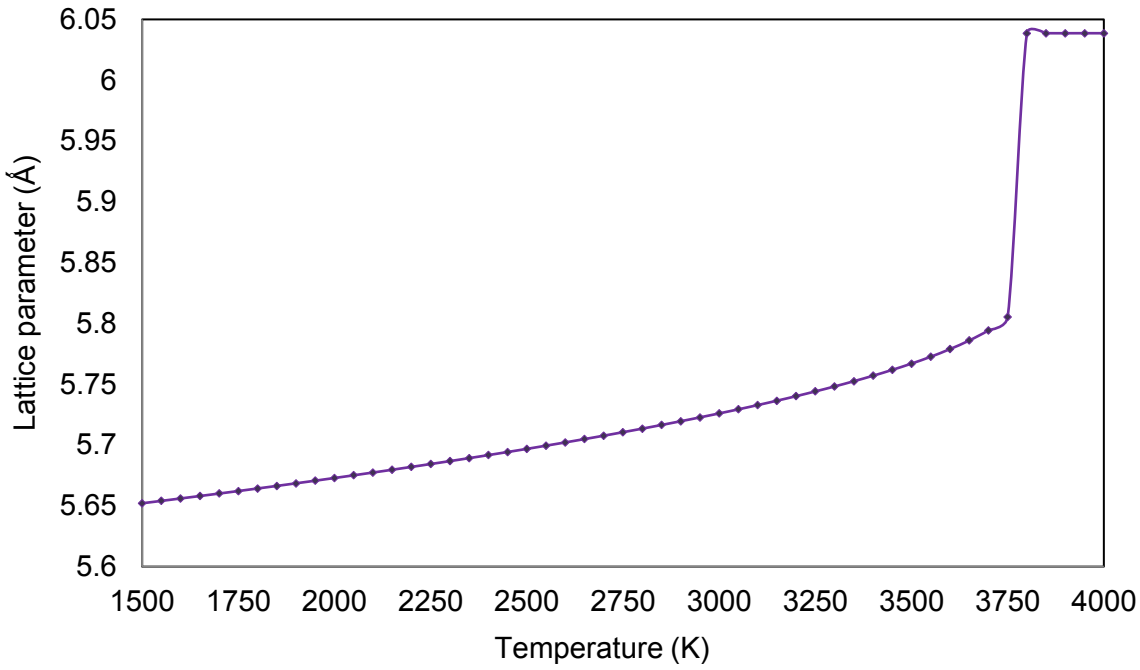

Figure 4.2: Change in lattice parameter against temperature for the pure ThO_2 system.

The melting point calculated within this work for the pure thoria system is in agreement with the value reported by Bohler et al. Table 2.2 compares the melting point for pure thoria calculated in this work with a number of other experimental values.

Melting temperature *(K)*	**This work**	**Bohler et al** [105]	**Ronchi et al** [106]	**Benz et al** [107]
Pure ThO_2	3750	3624 +/- 86	3651 +/- 17	3663 +/- 100

Table 2.2: Melting temperature for pure ThO_2 calculated in this work compared to literature.

Figure 4.3 shows the changes in lattice parameter with temperature for this work compared to a number of literature values. There is a good agreement between the values calculated in this work and the literature values.

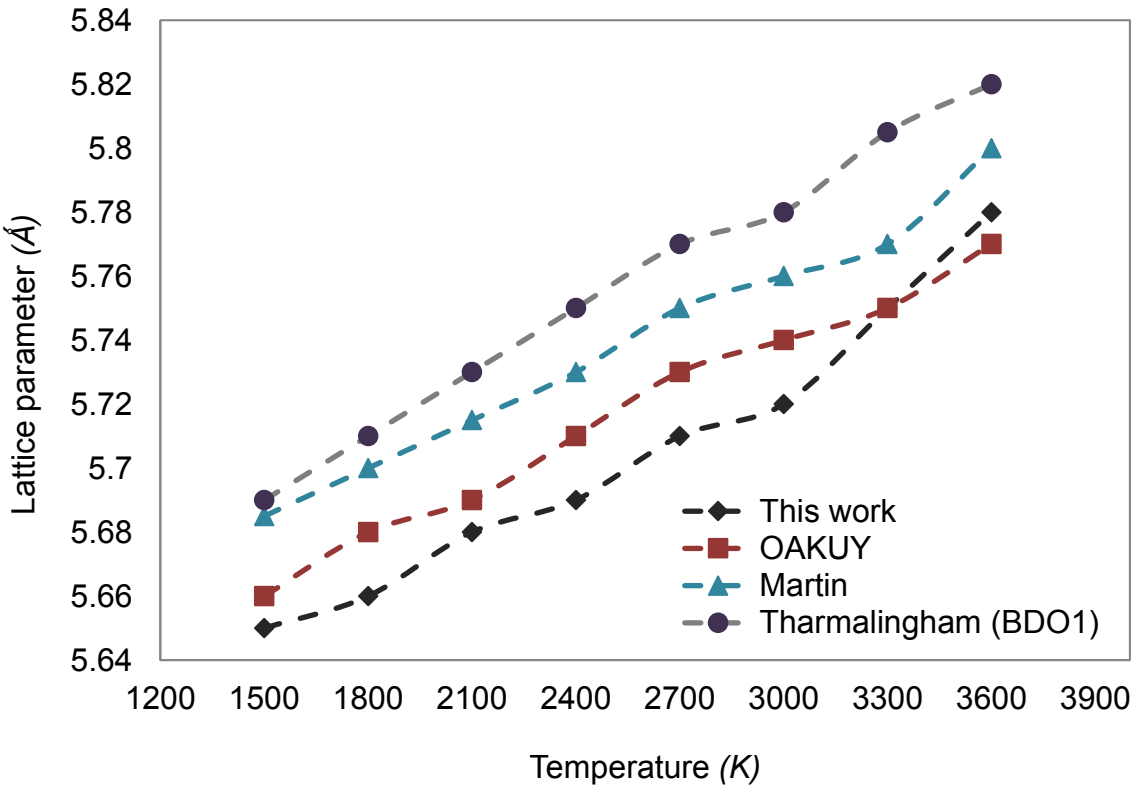

Figure 4.3: Plot of lattice parameter against temperature for this work and a number of computational literature papers.

The thermal expansion of a material is defined as the change in shape, area and volume of that material in response to a change in temperature through heat transfer [8]. Thermal expansion is caused by the increased kinetic energy of the atoms or ions

within the material when they are exposed to an increase in temperature. The ions will vibrate more causing them to have a larger average separation. A property later investigated in more detail using radial distribution function (chapter 6).

The volume of the system at each time step was used to calculate the thermal expansion of the system (shown in figure 4.4).

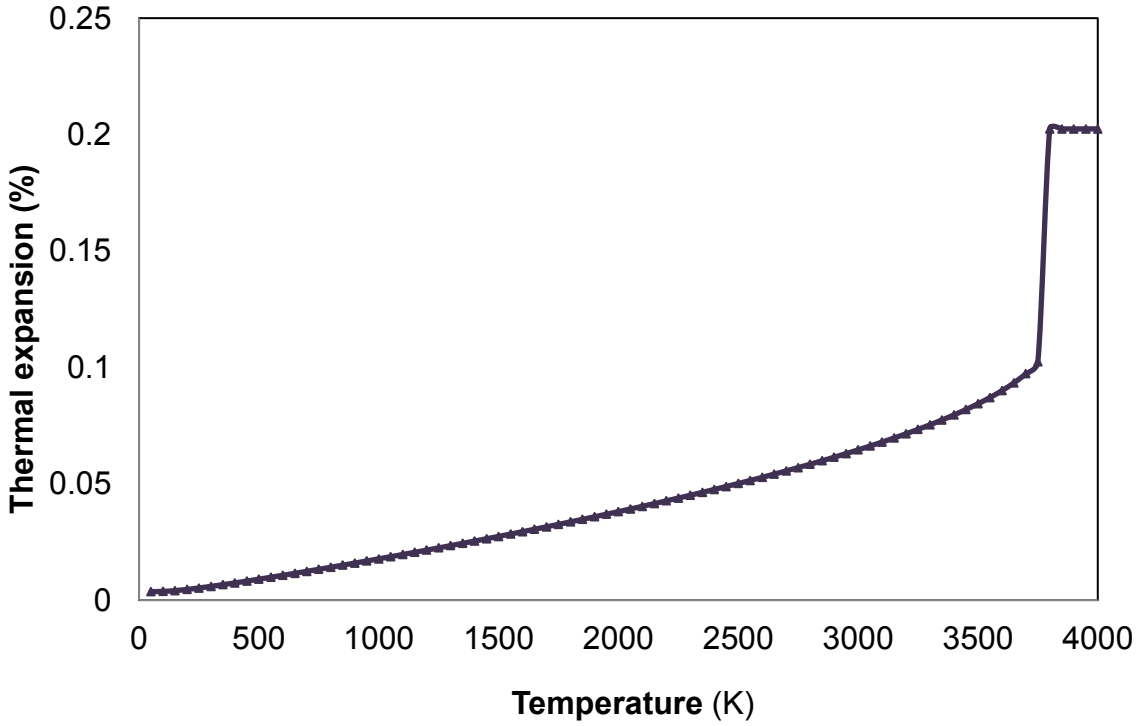

Figure 4.4: Plot of the temperature dependence of the thermal expansion of the pure ThO_2 cell.

The values of the thermal expansion calculated within this work (shown in figure 4.4) also show a melting temperature of 3750K.

The coefficient of thermal expansion calculated within this work is 1.96×10^{-5} at 300K. Experimental values for the coefficient of thermal expansion include Marples et al [109] who reported a value of 7.3×10^{-6} K^{-1} and Yamashita et al [110] who reported a value of 8.43×10^{-6} K^{-1}. The Coefficient of thermal expansion as a function of temperature is shown in figure 4.5.

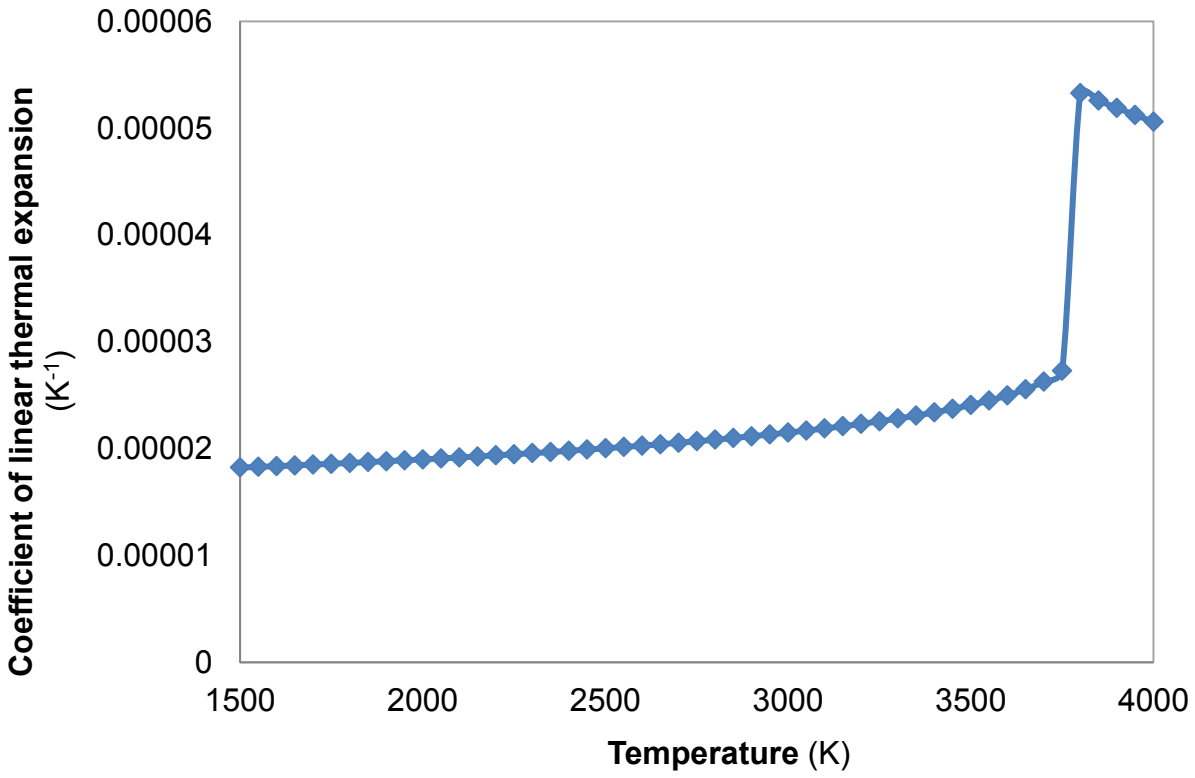

Figure 4.5: Coefficient of thermal expansion for pure ThO_2 as a function of temperature.

Changes in lattice parameter and thermal expansion calculated within this work are in agreement with the available computational and experimental values reported. These initial calculations of the pure system have been able to provide some information about the properties of the system but in order to get a more realistic look at the thermal properties of the system we need to include defects as above 0K the structure is no longer a perfect crystal.

4.3 Defective system

All solids at temperatures above 0K will contain intrinsic defects and as temperature increases more defects are formed. Therefore, it is vital that simulations are carried out on the defected structure where possible.

During all defect calculations, the ions surrounding the defect were allowed to relax in the energy minimisation procedures outlined in the methodology section.

4.3.1 Intrinsic defects

Isolated point defects were the first intrinsic defect calculations performed on the thorium dioxide crystal structure. The formation energy calculated for a vacancy defect relates to the removal of an ion from its lattice position within a perfect crystal to infinity. Formation values calculated for interstitial defects correspond to the addition of an ion into the lattice from infinity.

Defect	Literature Formation energy *(eV per defect)* [62]	Coordinate position	Calculated Formation energy *(eV per defect)*
Th^{4+} vacancy	84.66	(0,0,0)	78.05
O^{2-} vacancy	15.83	(0.25,0.25,0.25)	16.15
Th^{4+} Interstitial	-64.86	(0.5,0.5,0.5)	-59.13
O^{2-} Interstitial	-9.82	(0.5,0.5,0.5)	-11.06

Table 2.3: Vacancy and interstitial formation energies compared to experimental energies.

Initial simulations suggest that the thorium vacancy is the most energetically unfavourable defect with the largest positive formation energy and the thorium interstitial is the most energetically favourable defect with the largest negative formation energy. However, isolated defects do not tend to form as they are often combined into cluster defects. Therefore, Frenkel and schottky defects have also been calculated later on in this chapter.

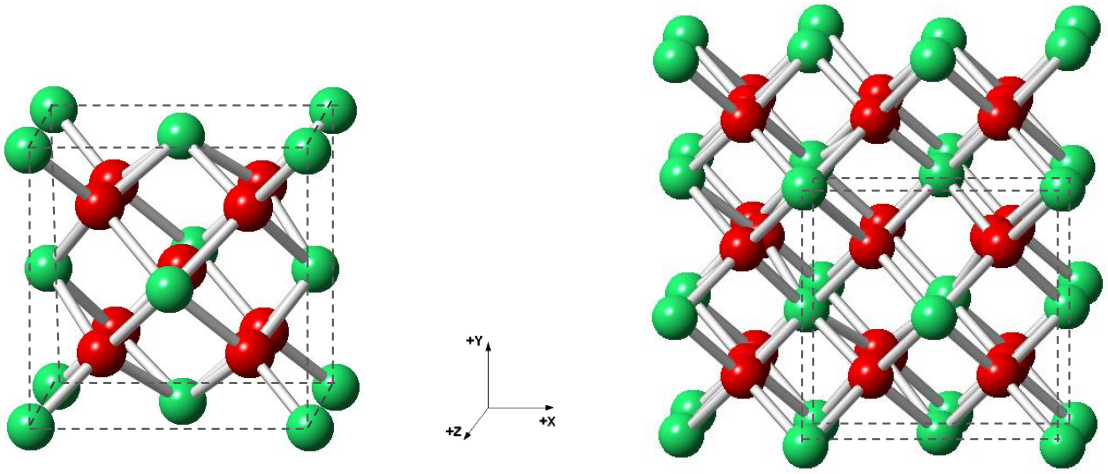

(a) (b)

Figure 4.6: Illustration of (a) oxygen interstitial (b) oxygen vacancy

Once simple point defects have been calculated then more complex cluster type calculations can be made. These calculations include Frenkel and Schottky defects. Frenkel defects involve the formation of a vacancy and an interstitial; an ion will move from its lattice position and migrate to an interstitial position. Schottky defects arise when a formula unit of the material, in this case ThO_2, is removed with each ion coming from their fixed lattice position to infinity. Both of these defects maintain charge neutrality within the lattice. The Kroger-Vink notation [111] for the intrinsic Frenkel and Schottky defects is shown in figure 4.7.

$$Th_{Th}^{x} \rightleftharpoons V_{Th}'''' + Th_{i}^{\cdots}$$

$$O_{O}^{x} \rightleftharpoons V_{\ddot{O}} + O_{i}''$$

$$Th_{Th}^{x} + 2O_{O}^{x} \rightleftharpoons V_{Th}'''' + 2\,V_{\ddot{O}} + ThO_2$$

Figure 4.7: Kroger-Vink notation for Frenkel and Schottky defects in the ThO_2 system.

The values for the Schottky and Frenkel defects can be calculated in two ways; the individual point defects can be combined using the equations shown in figure 4.3 which assumes infinite dilution or a cluster can be simulated. Table 2.4 shows the values calculated using the point defects compared with literature values.

Defect	Literature formation energy *(eV per defect)* [62]	Calculated formation energy Infinite dilution *(eV per defect)*
Th Frenkel	19.80	18.92
O Frenkel	6.01	5.09
Schottky trio	11.93	10.02

Table 2.4: Frenkel and Schottky defects compared with experimental values.

.

This method does not specify lattice positions with relation to each other; the distance between the ions is not defined. The distance between the defecting ions will have an effect on the value of the formation energy so must be considered. For simulations carried out in this way a cluster is created and specific defect positions are defined for a number of different configurations. The defect formation energy and binding energy are then calculated. The binding energy is the difference in energy between the unbound defects at infinite dilution and the bound defects in a cluster. Table 2.5 displays the results of the oxygen Frenkel pair formation with specific coordinates for each vacancy and interstitial shown.

Defect	Vacancy position	Interstitial position	Formation energy *(eV per defect)*	Binding energy *(eV per defect)*
OFP1	(-0.25,-0.25,-0.25)	(0.5,0.5,0.5)	3.73	1.22
OFP2	(-0.25,-0.25,0.25)	(0.5,0.5,0.5)	4.00	0.95

Table 2.5: Defect formation energy and binding energy for oxygen frenkel pair defect.

Initial results predict that the OFP1 defect would be the most energetically favourable with the smallest formation energy.

Thorium Frenkel defect energies were also investigated and the binding energies calculated. The thorium vacancy remained the same but the position of the interstitial varied. Table 2.6 shows the formation and binding energies of the thorium Frenkel defects along with vacancy and interstitial positions.

Defect	Vacancy position	Interstitial position	Formation energy *(eV per defect)*	Binding energy *(eV per defect)*
THF1	(1.0, 1.0, 0.0)	(1.0, 1.0, 0.375)	19.22	0.33
THF2	(1.0, 1.0, 0.0)	(1.0, 1.0, 0.675)	18.99	0.07

Table 2.6: Defect formation energy and binding energy for thorium Frenkel pair defect.

Initial calculations show that the THF2 configuration would be the most energetically favourable with the smallest defect formation energy and the smallest binding energy.

A number of configurations for Schottky defects were also considered with the thorium and 1st oxygen vacancy position remaining the same but the position of the 2nd oxygen vacancy changing. The resulting formation and binding energies are shown in table 2.7.

Defect	**Position of thorium vacancy**	**Position of oxygen 1 vacancy**	**Position of oxygen 2 vacancy**	**Formation energy** *(eV per defect)*	**Binding energy** *(eV per defect)*
Sch1	(0.0, 0.0, 0.0)	(0.25, 0.25, 0.25)	(-0.25,-0.25,-0.25)	5.64	-1.46
Sch2	(0.0, 0.0, 0.0)	(0.25, 0.25, 0.25)	(-0.25,0.25,-0.25)	5.57	-1.48
Sch3	(0.0, 0.0, 0.0)	(0.25, 0.25, 0.25)	(-0.25,0.25,0.25)	5.99	-1.34

Table 2.7: Defect formation and binding energy for three Schottky configurations.

In summary, for the unbound defects, the oxygen Frenkel was predicted to have the lowest energy of formation of 5.09 eV which is half the Schottky formation energy (10.02 eV) which itself is much lower than the thorium Frenkel of 18.92 eV. Thus for any given temperature the equilibrium concentration of defects is predicted to be predominantly oxygen Frenkels. The cluster calculations show that there is little difference in energy for the bound thoria Frenkel (18.99 eV), the oxygen Frenkel reduces slightly to 3.73 eV but the bound Schottky has roughly half the value of the unbound defect (5.57 eV) predicting the equilibrium concentration of defects to have a significant proportion of Schottky cluster vacancies in addition to oxygen Frenkels.

4.3.2 Extrinsic defects and fission products

Extrinsic doping of different substances into the thorium dioxide crystal can change its properties and characteristics. Doping thorium dioxide with uranium or plutonium (discussed in section 4.4) creates a mixed oxide fuel that can be used within the reactor as the main fuel. Doping with fission materials or materials introduced to the fuel such as components of a fuel rod will ensure a more realistic simulation of the fuel contents during the fuel cycle. Some of the most common fission products and products of most concern were considered within this research but unfortunately, some of the fission products such as xenon and caesium do not have any consistent potentials available. Two fission products including barium [69] and strontium [112] have published potentials available in the literature. A potential set for gadolinium was derived within the group (see chapter 3). All of the potentials used in this section are shown in table 2.8.

Interaction	A *(eV)*	*P (Å)*	C *(eVÅ^{-6})*	Y *(|e|)*	K_2 *(eVÅ^{-2})*
Gd-O	2962.90599	0.31441	0.0	3.973	299.96
Sr-O	959.1	0.3721	0.0	3.251	71.7
Ba-O	905.7	0.3976	0.0	9.203	459.2

Table 2.8: Interatomic potentials for fission products.

A single ion was first placed into the lattice as an interstitial defect at the 0.5, 0.5, 0.5 position and the defect energy calculated (shown in table 2.9).

The solution energy for the interstitial defects were also calculated using the equations shown in figure 4.8.

$$E_{soln} = E(M''_{Th}) + \ E(V_O^{\bullet\bullet}) + \ U_{latt}(ThO2) - U_{latt}(MO)$$

Where M = Sr or Ba

$$E_{soln} = 2E(M'_{Th}) + \ E(V_O^{\bullet\bullet}) + \ 2U_{latt}(ThO2) - U_{latt}(M_2O_3)$$

Where M = Gd

Figure 4.8: Kroger-Vink notations for the solution energies of doping various fission products into the ThO_2 unit.

Defect	Charge on system	Formation defect energy *(eV per defect)*	Solution energy *(eV per defect)*
Strontium substitution	-2	-12.37	0.98
Barium substitution	-2	-7.69	4.15
Gadolinium substitution	-1	-38.34	2.15

Table 2.9: Formation defect energy and solution energy values for various fission product substitutions.

The initial calculations show that gadolinium has the most negative substitutional formation energy, implying that it is the most energetically favourable defect to form. However, the value for the solution energy for gadolinium is a little higher than that of strontium. The solution energy depends upon a number of aspects including charge on the ions within the lattice and the dissociation energy required to break apart the dopant lattice. Figure 4.9 shows a plot of solution energy as a function of ionic radius for each of the three dopant ions.

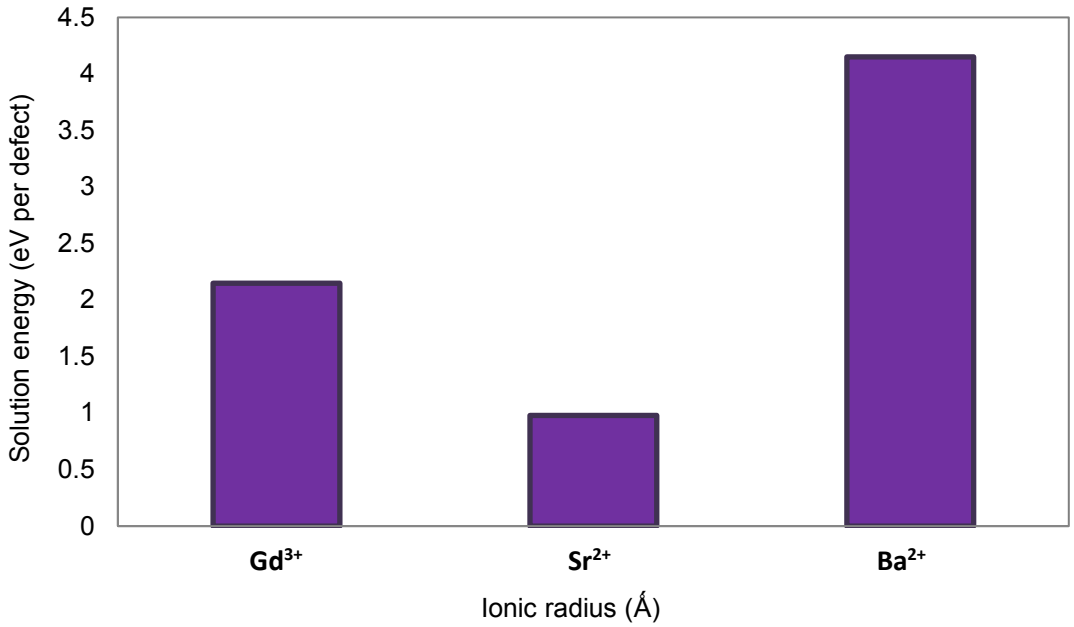

Figure 4.9: Plot of solution energy as a function of ionic radius for strontium, barium and gadolinium

Gadolinium is of particular interest as it has the highest neutron cross section of any other natural element which makes it useful within the control rods to control the nuclear cycle within the reactor core. Gadolinium is also produced as a fission product in the fuel cycle and due to its neutron absorbing properties can affect the fuel cycle significantly more than any of the other products by absorbing many of the neutrons needed for the fission process to occur. Previous research in this area on gadolinium has been described in section 3.2.1 of chapter 3.

One of the most informative research papers is that of Osaka et al [66] who investigated the molecular dynamics of gadolinia-doped thoria. The research conducted within this paper focussed on the defect positions of the gadolinium and

how they affected properties of the fuel including lattice parameter, thermal expansion and diffusion coefficients. Defects investigated include the simple gadolinium interstitial and the double gadolinium interstitial oxygen vacancy charge neutral defect (shown in figure 4.10).

$$Gd'_{Th}$$

$$\{Gd'_{Th}\ V_O^{\bullet\bullet} Gd'_{Th}\}$$

Figure 4.10: Kroger-Vink notation of gadolinium defects simulated in the work of Osaka et al. and in this work.

Some of the defect calculations carried out by Osaka et al. were repeated and adapted using the 4x4x4 super cell in this work, and where possible, compared to the literature. The results are shown in table 3.0.

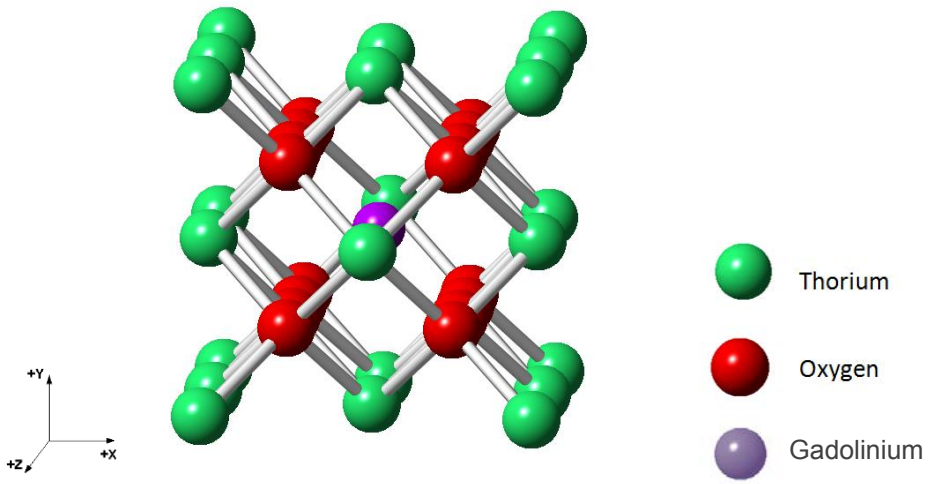

Figure 4.11: Gadolinium interstitial within the ThO_2 crystal

Defect	Configuration	Defect formation energy *(eV per defect)*	Binding energy *(eV per defect)*
Gd'_{Th}	/	24.89	/
$\{Gd'_{Th}\ V_O^{\bullet\bullet} Gd'_{Th}\}$	1	65.30	0.63
	2	63.32	2.61
	3	63.12	2.81
	4	64.91	1.02

Table 3.0: Defect formation and binding energy of various gadolinium defects within the ThO_2 crystal.

Fission products have been found to form clusters when produced within a crystal [113-115] structure and it is the formation of these clusters that can cause significant physical changes within the material. The cluster formation of four gadolinium interstitials at positions within the plane and out of the plane were investigated (illustration shown in figure 4.12). The results are shown in table 3.1.

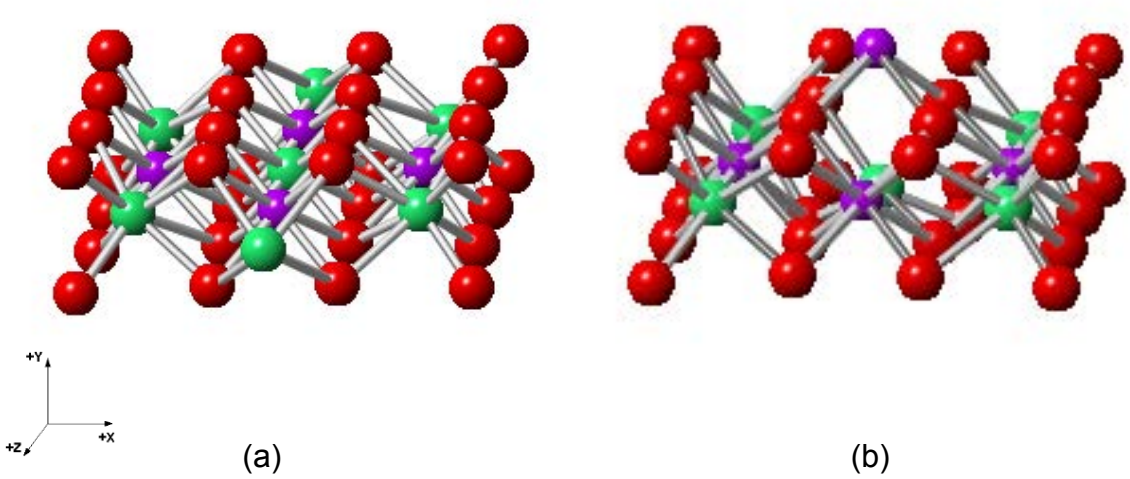

Figure 4.12: Relaxed structure of gadolinium cluster formation in ThO_2 (a) in the plane and (b) out of plane.

Defect	**Defect formation energy** (eV per defect)	**Binding energy** (eV per defect)
Gadolinium cluster (a)	-144.83	8.55
Gadolinium cluster (b)	-147.35	6.02

Table 3.1: Defect formation energy and binding energy of two gadolinium clusters in ThO_2.

The results shown in table 3.1 suggest that the more energetically favourable cluster is configuration *b* as it has the most negative defect formation energy and the smallest value for the binding energy.

In order to investigate the structural effects of gadolinium doping, a number of different percentage compositions of gadolinium were investigated with relation to changes in the lattice parameter of the unit cell (shown in table 3.2). The gadolinium ions were placed on thorium vacancy positions leaving behind a single positive charge per ion.

Percentage gadolinium	**Overall charge on crystal**	**Lattice energy** *(eV)*	**Lattice constant** *(Å)*		
			a	**b**	**c**
0	0	-100.330	5.600	5.600	5.600
25	-8	-3018.981	5.553	5.553	5.553
50	-16	-2838.999	5.486	5.504	5.504
75	-24	-2784.326	5.415	5.419	5.419

Table 3.2: Change in lattice parameter and lattice energy with percentage gadolinium.

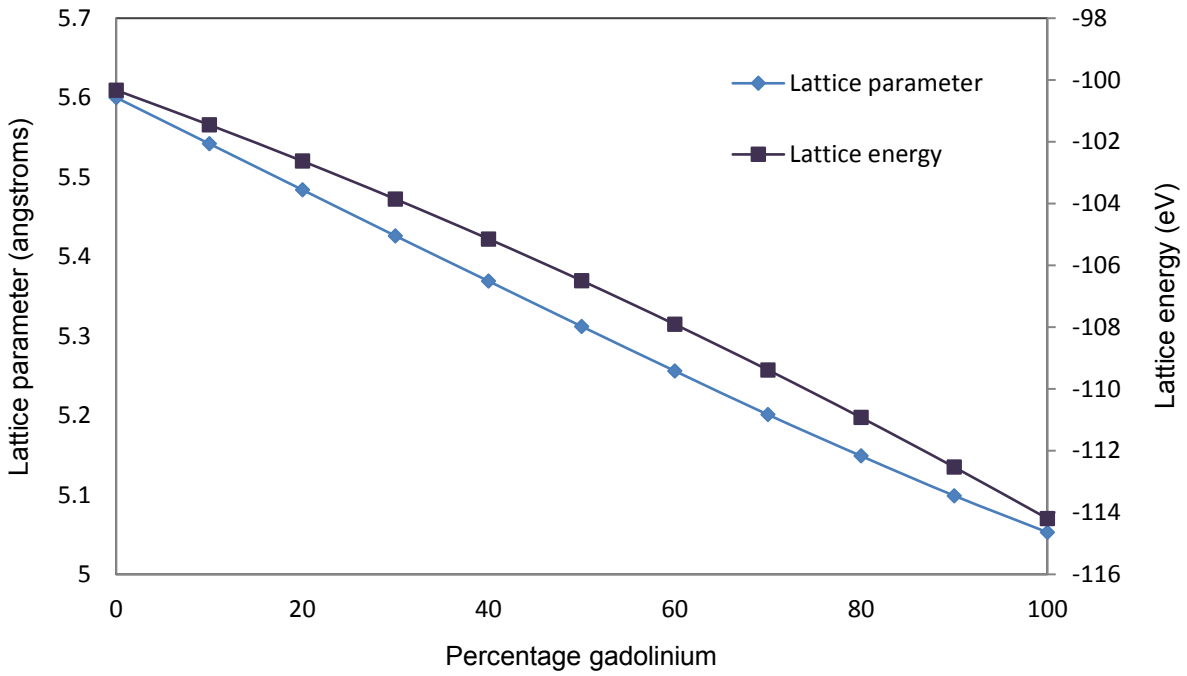

Figure 4.13: Lattice parameter and lattice energy against percentage dopant gadolinium.

Increased gadolinium concentration causes a decrease in lattice parameter and lattice energy. This implies that the fuel pellets may shrink upon prolonged gadolinium exposure. Further simulations could be carried out as to the segregation of gadolinium defects and their movement within the structure and how this affects the thermophysical properties of the fuel.

4.4 The mixed oxide fuel

4.4.1 Introduction

As thoria is fertile rather than fissile there must be a neutron source added to the fuel to begin the nuclear process. This neutron source is commonly uranium or plutonium. Creating a mixed fuel with uranium or plutonium has added benefits; the uranium or plutonium can be that produced as waste from another nuclear cycle and would therefore be recycled in the process. This will help to eliminate any uranium or plutonium waste storage issues. According to the world nuclear association [62] mixed oxide fuel already currently provides almost 5% of the world's energy implying that thorium mixed fuels would be a viable future option.

There has already been a considerable amount of research conducted using mixed thorium fuels and the thermodynamics of the newly formed system including the previously mentioned computational studies of Martin et al [68]. Experimental studies of thorium mixed fuels have also already been discussed in chapter 4 with research from Agarwal et al., Dash et al. and the review provided by Bakker et al. [59].

S. Liu et al [116] and Guangwen et al [117] have both studied the design of a mixed thorium fuel reactor with Guangwen also investigating the spent fuel characteristics and concluding that a uranium/thorium mixed fuel would prove to be beneficial in many ways including conservation of current uranium stores. All of these have only studied the mixed UO_2/ThO_2 fuels. Unfortunately, there is very little literature data available for PuO_2/ThO_2, with most of the available experimental data being compared in the review paper by Bakker. Hubert et al. [118] completed experimental XRD work on doped thoria investigating a number of properties including an in depth study of the changes in bond lengths between atoms upon doping.

Throughout this section the mixed oxide fuels ThO_2-PuO_2 and ThO_2-UO_2 have been investigated individually as to their changes in bulk properties and defect energies with dopant ion concentration. The interatomic potentials used throughout this investigation are those published by Read et al [25, 59] and are shown in table 3.3.

Interaction	**A** *(eV)*	***P*** *(Å)*	**C** *($eVÅ^{-6}$)*	**Y** *(|e|)*	**K_2** *($eVÅ^{-2}$)*
Pu-O	1116.3317	0.3926	0.0	6.54	206.77
U-O	1027.5967	0.402616	0.0	6.54	110.75343

Table 3.3: Interatomic potential for the plutonium oxygen and uranium oxygen interactions.

In order to simulate the mixed fuel the dopant ion was doped into the thorium interstitial sites at a number of different percentages and the defect formation energy and solution energy calculated (results shown in table 3.4). The equations used to calculate the solution energy are shown in figure 4.14.

$$E_{soln} = E(Pu_{Th}^{x}) + U_L(PuO_2) - U_L(ThO_2)$$

$$E_{soln} = E(U_{Th}^{x}) + U_L(UO_2) - U_L(ThO_2)$$

Figure 4.14: Solution energy calculations for the doping of a single ion at the thorium position.

Dopant ion	**Lattice position**	**Defect formation energy** *(eV per defect)*	**Solution energy** *(eV)*
Pu^{4+}	0.0, 0.0, 0.0	-51.95	3.02
U^{4+}	0.0, 0.0, 0.0	-60.90	1.58

Table 3.4: Defect formation energy and solution energy for the doping of plutonium and uranium into the ThO_2 lattice.

Initial defect formation energies suggest that it is more energetically favourable to dope the uranium ion into the thorium position than plutonium, which is in agreement with the solution energy trends shown in the table above.

4.4.2 ThO_2 - PuO_2 mixed fuel

In February 2005 the parliamentary office of science and technology issued a statement about the management of the UK's plutonium stockpile [119]. They discussed how the stocks of plutonium have built up due to it being produced as a waste product in the uranium fuel cycle. They quote a value of 70 tonnes of plutonium currently in stock in the UK and estimate that will increase to around 100 tonnes in the next ten years. The statement also suggests some solutions to the large plutonium stock pile including the creation of a thorium/plutonium mixed fuel.

Research into a thorium/plutonium mixed fuel has not been as prevalent as thorium/uranium mixed fuels but there have been some interesting studies into the effects that plutonium may have on the thorium fuel when a mixed fuel is generated. Kutty et al. [120] carried out a detailed study into the thermophysical properties of pure thorium oxide fuels along with uranium and plutonium mixed fuels. They concluded that more in depth research is needed with regards to the mixed oxide fuels performance is necessary before they are tested in nuclear reactors.

In order to investigate the bulk properties in more detail the supercell was doped with varying concentrations of plutonium and uranium in the range of 0-60%. This range goes above what is used in real MOX fuels (5-15%) but useful for initial predictions. Figure 4.15 illustrates the supercell with varying plutonium dopant percentage.

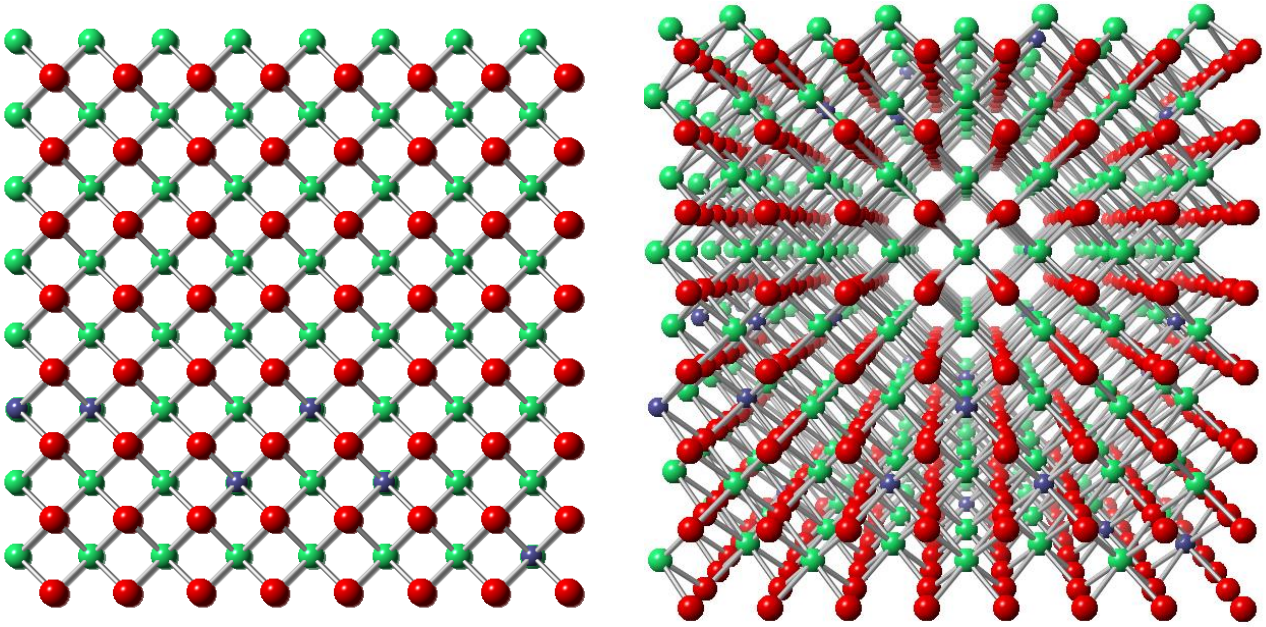

(a)

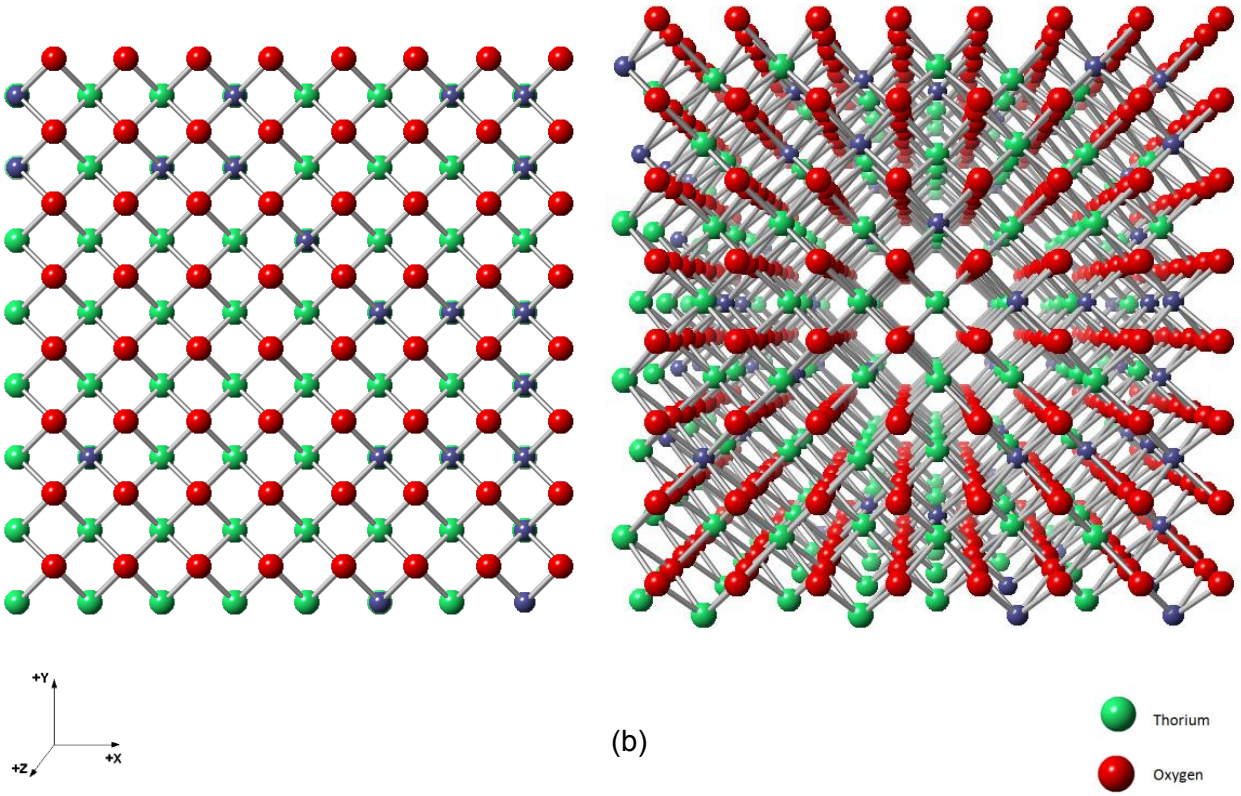

(b)

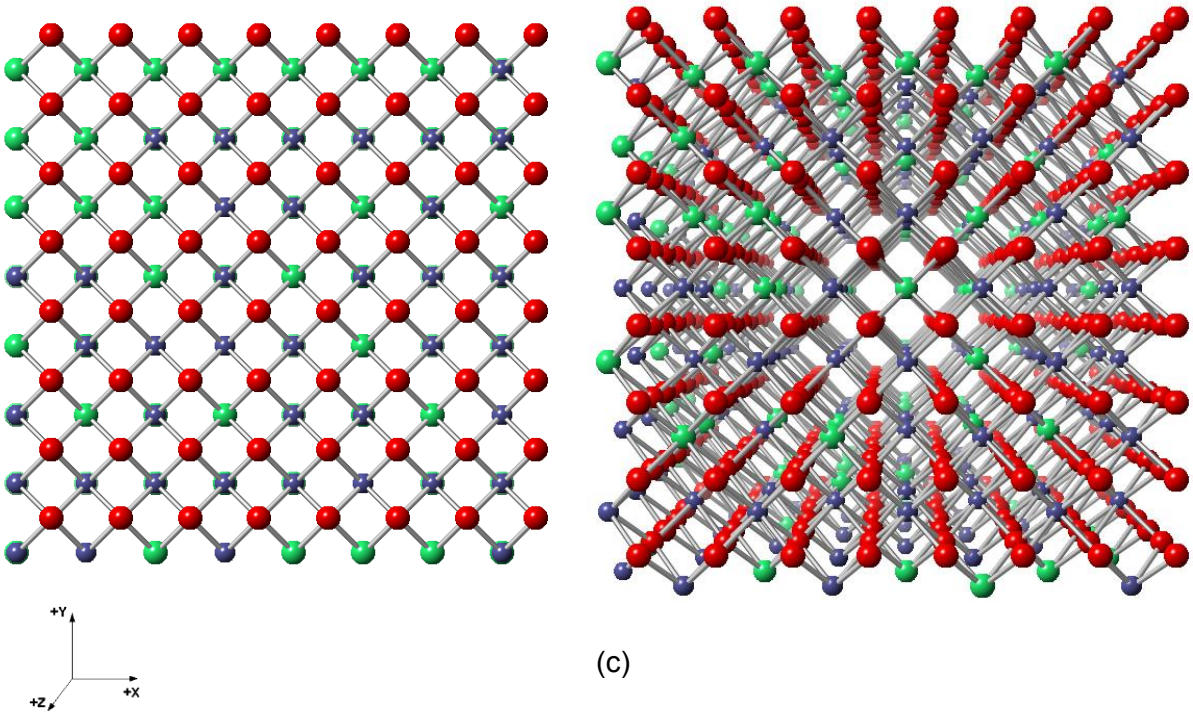

Figure 4.15: 4x4x4 ThO_2 cell with (a) 10.16% plutonium doped (b) 30.08% plutonium doped (c) 60% plutonium doped

A random number generator was used to ensure that each cell was randomly doped with the correct concentration of dopant ions. The results of the random plutonium doping are shown in table 3.5. Figure 4.16 shows the change in lattice parameter and lattice energy upon increasing plutonium dopant concentration. These initial calculations demonstrate a decrease in lattice parameter and lattice energy of the thorium cell with increasing plutonium doping. Plutonium has slightly smaller ionic radius (0.887Å) than thorium (0.972Å) which could explain the decrease in lattice parameter.

The solution energy for a single plutonium ion at the thorium vacancy position was also calculated for each of the dopant ion concentrations. The results are shown in figure 4.17.

% dopant	Formula	Lattice energy (eV)	Lattice constant (Å)	C11	C12	C44	Bulk modulus (GPa)	Shear modulus (GPa)	Youngs modulus (GPa)	Static dielectric constant	High freq dielectric constant
0	$Th_{256}O_{512}$	-100.33	5.60	373.23	114.37	65.82	200.65	81.93	319.58	0.23	18.07
1.17	$Th_{253}Pu_3O_{512}$	-100.37	5.60	373.52	114.51	65.75	200.85	81.88	319.79	0.23	18.23
1.95	$Th_{251}Pu_5O_{512}$	-100.39	5.60	373.72	114.60	65.71	200.97	81.84	319.92	0.23	18.34
3.13	$Th_{248}Pu_8O_{512}$	-100.43	5.60	374.00	114.74	65.64	201.16	81.79	320.13	0.23	18.49
3.91	$Th_{246}Pu_{10}O_{512}$	-100.45	5.59	374.20	114.83	65.60	201.29	81.76	320.26	0.23	18.60
5.08	$Th_{243}Pu_{13}O_{512}$	-100.49	5.59	374.49	114.98	65.54	201.48	81.72	320.47	0.23	18.75
5.86	$Th_{241}Pu_{15}O_{512}$	-100.51	5.59	374.69	115.07	65.49	201.61	81.69	320.61	0.23	18.86
7.03	$Th_{238}Pu_{18}O_{512}$	-100.55	5.59	374.97	115.21	65.43	201.79	81.65	320.82	0.24	19.01
7.81	$Th_{236}Pu_{20}O_{512}$	-100.57	5.59	375.16	115.30	65.40	201.92	81.62	320.95	0.24	19.09
8.98	$Th_{233}Pu_{23}O_{512}$	-100.61	5.58	375.44	115.43	65.36	202.10	81.58	321.15	0.24	19.25

10.16	$Th_{230}Pu_{26}O_{512}$	-100.64	5.58	375.74	115.58	65.31	202.30	81.55	321.36	0.24	19.36
14.84	$Th_{218}Pu_{38}O_{512}$	-100.79	5.57	376.92	116.14	65.13	203.07	81.42	322.20	0.24	19.90
19.92	$Th_{205}Pu_{38}O_{512}$	-100.95	5.56	378.18	116.74	64.96	203.89	81.33	323.11	0.24	20.48
25	$Th_{192}Pu_{64}O_{512}$	-101.10	5.55	379.49	117.31	64.84	204.71	81.27	324.08	0.24	20.96
30.08	$Th_{179}Pu_{77}O_{512}$	-101.26	5.54	380.86	117.97	64.75	205.59	81.24	325.07	0.24	21.37
35.16	$Th_{166}Pu_{90}O_{512}$	-101.42	5.53	382.29	118.59	64.67	206.50	81.24	326.13	0.24	21.86
39.84	$Th_{154}Pu_{102}O_{512}$	-101.57	5.52	383.64	119.21	64.67	207.37	81.28	327.11	0.24	22.18
44.92	$Th_{141}Pu_{115}O_{512}$	-101.73	5.51	385.24	119.93	64.66	208.37	81.34	328.29	0.24	22.49
50	$Th_{128}Pu_{128}O_{512}$	-101.89	5.50	386.92	120.66	64.70	209.41	81.44	329.53	0.24	22.71
55.08	$Th_{115}Pu_{141}O_{512}$	-102.06	5.49	388.66	121.46	64.76	210.53	81.56	330.81	0.24	22.99
60.16	$Th_{102}Pu_{154}O_{512}$	-102.22	5.48	390.42	122.22	64.84	211.63	81.74	332.14	0.24	23.24

Table 3.5: Bulk properties for various plutonium dopant concentrations.

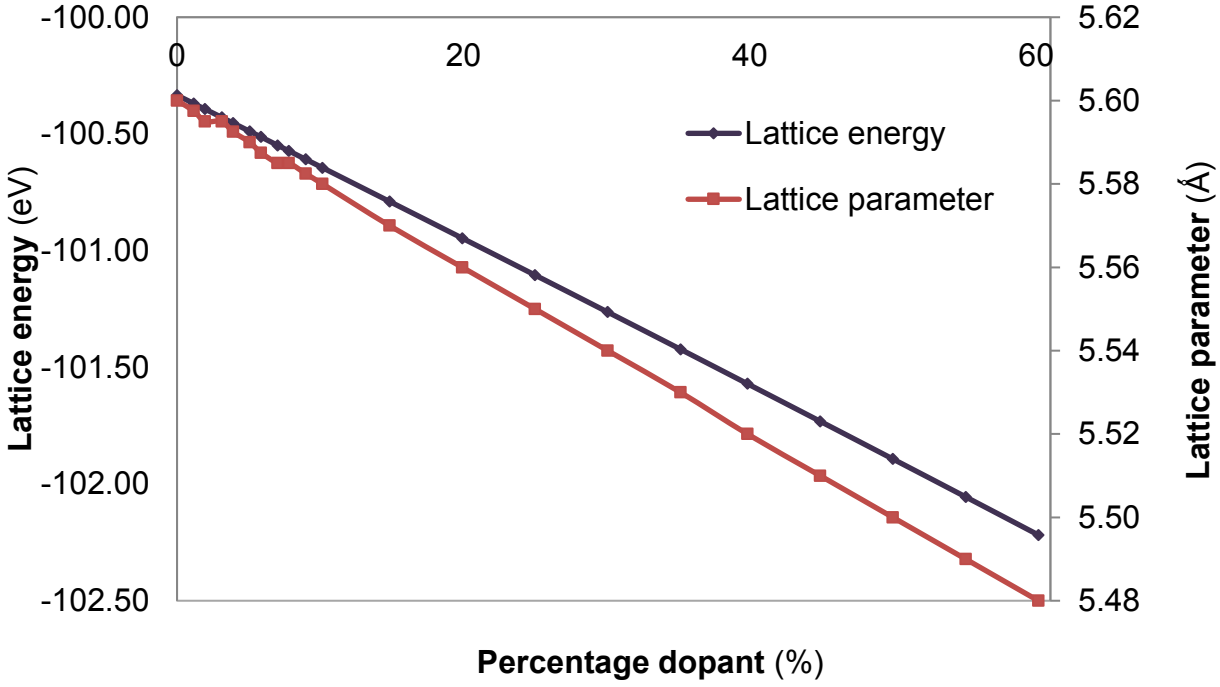

Figure 4.16: Lattice parameter and lattice energy changes with percentage plutonium doping.

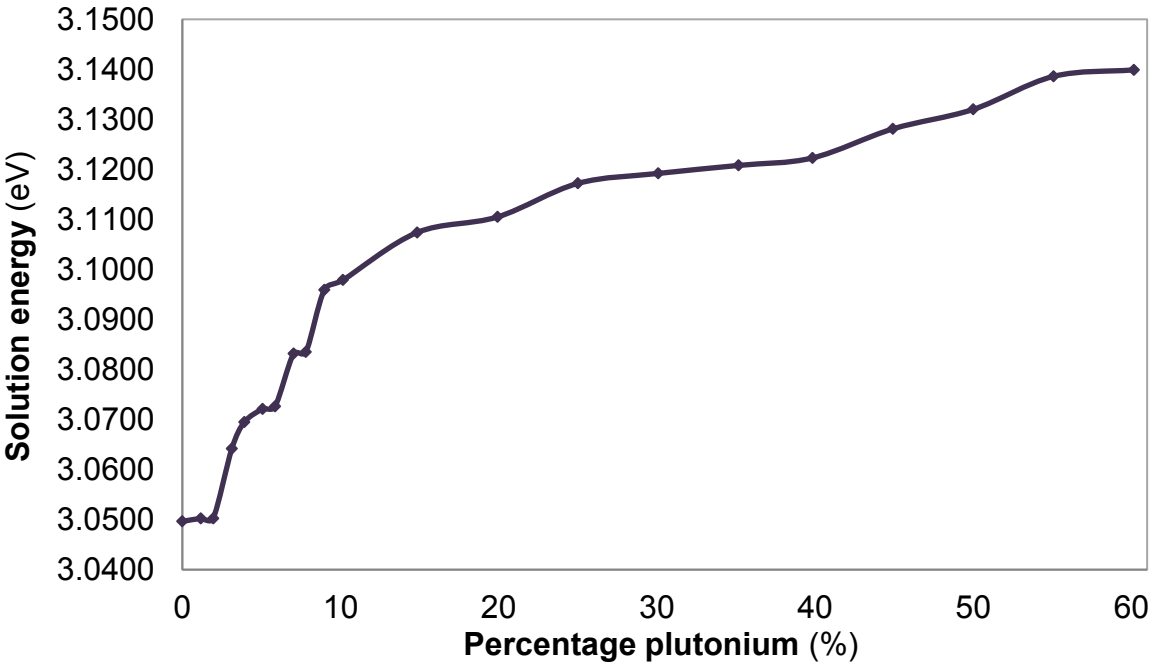

Figure 4.17: A plot of the solution energy against percentage plutonium concentration.

Initial defect simulations were run on the doped system to investigate any changes in defect energy with percentage dopant for up to 5% plutonium. For each percentage dopant the configuration with the lowest lattice energy was chosen to complete the defect calculation. The results of the vacancy defect calculations are shown in table 3.6. Upon increased plutonium doping the energy for an oxygen vacancy formation increases slightly. For the formation of a thorium and plutonium vacancy the defect energy decrease slightly.

Percentage plutonium (%)	**Defect energy** (eV)		
	Oxygen vacancy	**Thorium vacancy**	**Plutonium vacancy**
0	16.15	78.05	-
1.17	16.16	78.03	80.17
1.95	16.16	77.99	80.15
3.13	16.17	77.96	80.11
3.91	16.18	77.93	80.08
5.08	16.19	77.90	80.01

Table 3.6: Simple vacancy defects in the plutonium doped ThO_2 system with varying dopant percentage.

4.4.3 ThO_2 – UO_2 mixed fuel

As current nuclear reactors are powered by uranium oxide fuels the natural option for the creation of a mixed oxide thorium fuel would be with uranium. Uranium is fissile so would be an excellent source of neutrons for the thorium nuclear cycle to begin. Research into the generation of a thorium/uranium mixed fuel has been plentiful but as reported by Kutty et al. [120] more research into the behaviour of the mixed fuel is required before it can be utilized.

As with the plutonium investigations carried out in section 4.4.2 the 4x4x4 thorium dioxide cell was doped with varying concentrations of uranium and various bulk properties were investigated. Figure 4.18 illustrates the crystal structure upon random uranium doping.

The results of the random uranium doping are shown in table 3.7. Figure 4.19 shows the change in lattice parameter and lattice energy upon increasing uranium dopant concentration. These initial calculations demonstrate a decrease in lattice parameter and lattice energy of the thorium cell with increasing uranium doping. Uranium has a smaller ionic radius (0.520Å) than thorium (0.972Å) which could explain the decrease in lattice parameter.

The solution energy for a single uranium ion at the thorium vacancy position was also calculated for each of the dopant ion concentrations. The results are shown in figure 4.18.

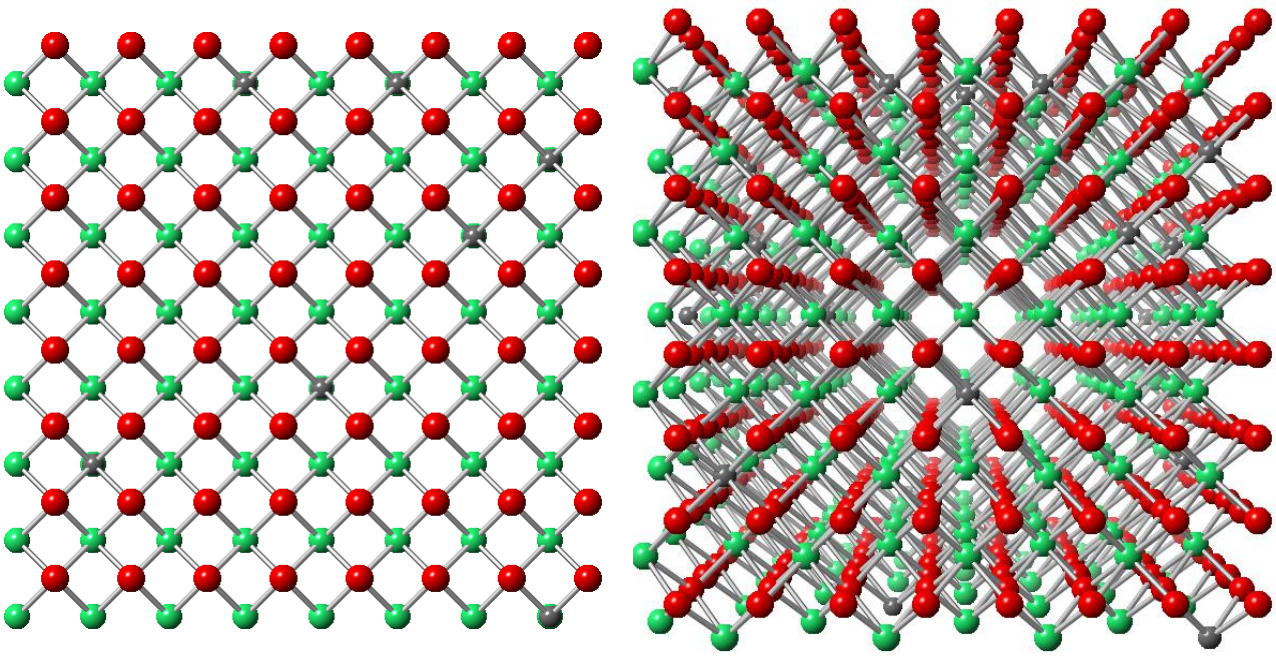

(a)

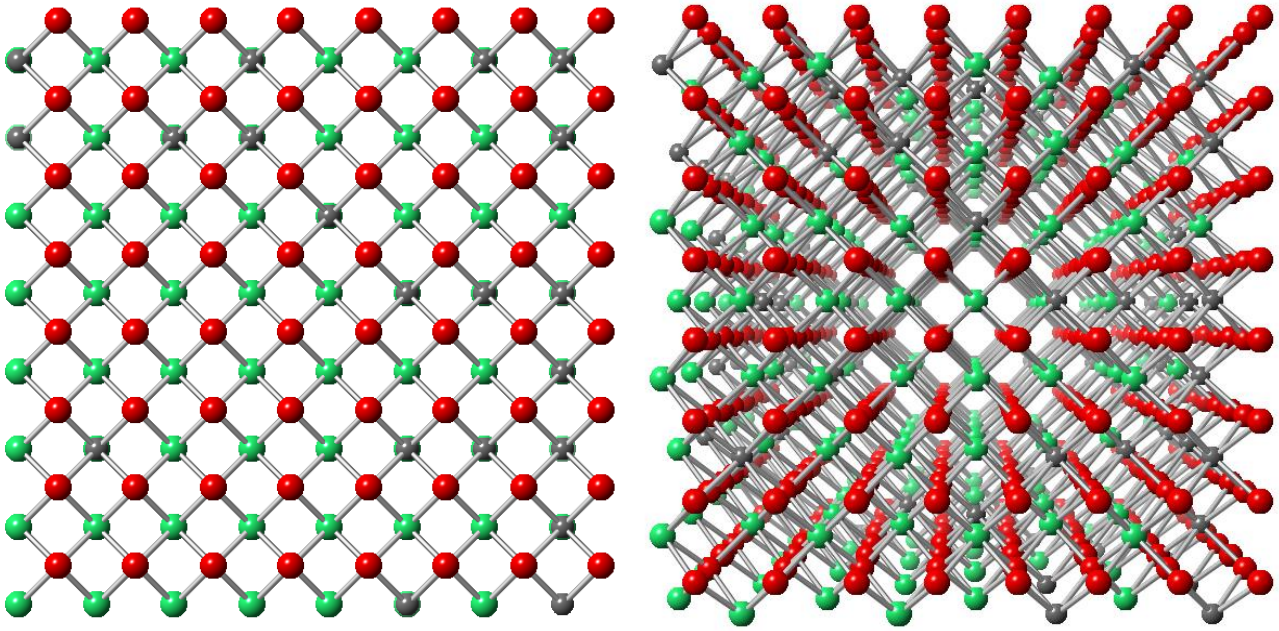

(b)

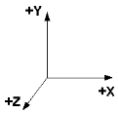

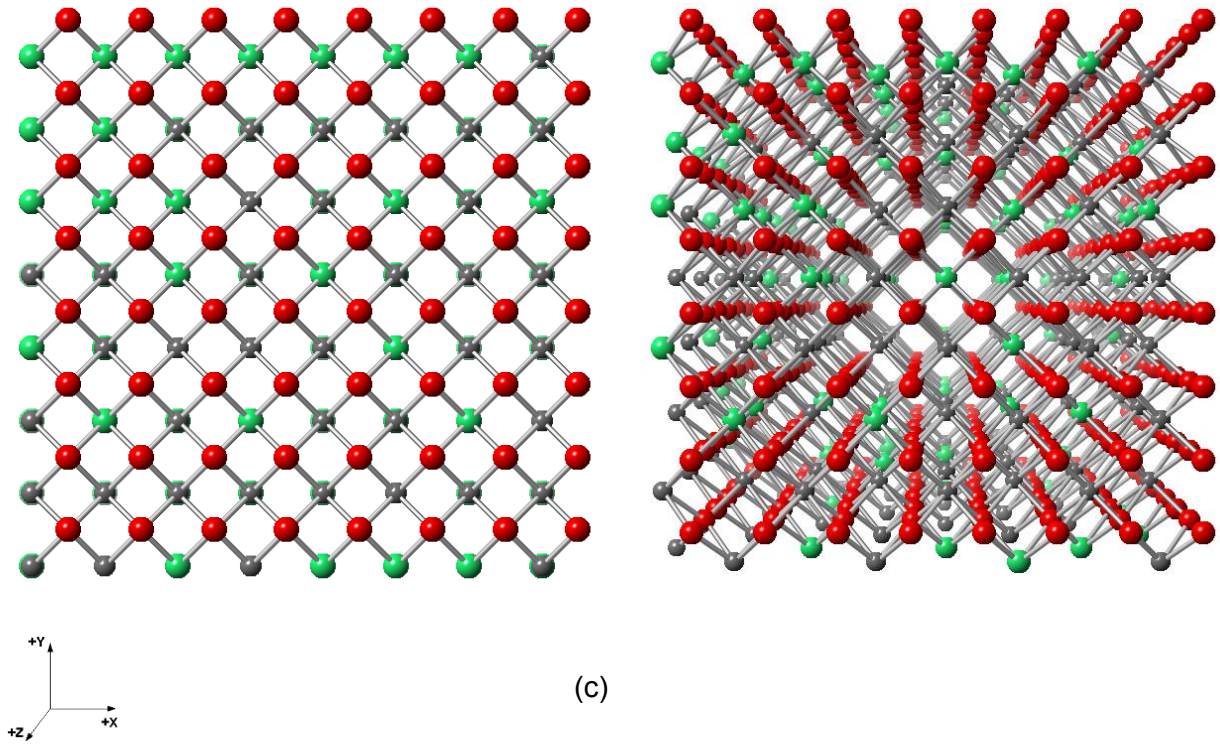

(c)

Figure 4.18: 4x4x4 ThO_2 cell doped with (a) 10.16% uranium doped (b) 30.08% uranium doped (c) 60% uranium doped

% dopant	Formula	Lattice energy (eV)	Lattice constant (Å)	C11	C12	C44	Bulk modulus (GPa)	Shear modulus (GPa)	Youngs modulus (GPa)	Static dielectric constant	High freq dielectric constant
0	$Th_{256}O_{512}$	-100.33	5.60	373.23	114.37	65.82	200.65	81.93	319.58	0.23	18.07
1.17	$Th_{253}U_3O_{512}$	-100.35	5.60	373.39	114.38	65.68	200.72	81.80	319.74	0.23	18.19
1.95	$Th_{251}U_5O_{512}$	-100.37	5.60	373.49	114.40	65.59	200.76	81.72	319.85	0.23	18.27
3.13	$Th_{248}U_8O_{512}$	-100.38	5.60	373.65	114.41	65.44	200.83	81.60	320.01	0.23	18.39
3.91	$Th_{246}U_{10}O_{512}$	-100.40	5.60	373.76	114.43	65.35	200.87	81.52	320.12	0.23	18.47
5.08	$Th_{243}U_{13}O_{512}$	-100.42	5.59	373.92	114.44	65.21	200.94	81.40	320.28	0.23	18.59
5.86	$Th_{241}U_{15}O_{512}$	-100.43	5.59	374.01	114.45	65.13	200.97	81.34	320.37	0.23	18.65
7.03	$Th_{238}U_{18}O_{512}$	-100.44	5.59	374.14	114.47	65.02	201.03	81.24	320.51	0.23	18.75
7.81	$Th_{236}U_{20}O_{512}$	-100.45	5.59	374.24	114.48	64.94	201.06	81.17	320.60	0.23	18.80
8.98	$Th_{233}U_{23}O_{512}$	-100.47	5.59	374.37	114.49	64.83	201.12	81.07	320.74	0.23	18.91

10.16	$Th_{230}U_{26}O_{512}$	-100.48	5.59	374.51	114.51	64.71	201.18	80.98	320.88	0.23	19.01
14.84	$Th_{218}U_{38}O_{512}$	-100.55	5.58	375.06	114.57	64.28	201.40	80.60	321.44	0.23	19.38
19.92	$Th_{205}U_{38}O_{512}$	-100.62	5.58	375.68	114.66	63.83	201.66	80.22	322.06	0.23	19.80
25	$Th_{192}U_{64}O_{512}$	-100.69	5.57	376.32	114.75	63.42	201.95	79.87	322.69	0.23	20.16
30.08	$Th_{179}U_{77}O_{512}$	-100.75	5.57	376.93	114.83	63.04	202.19	79.54	323.31	0.23	20.49
35.16	$Th_{166}U_{90}O_{512}$	-100.82	5.56	377.59	114.88	62.60	202.45	79.18	324.00	0.23	20.86
39.84	$Th_{154}U_{102}O_{512}$	-100.89	5.56	378.23	114.93	62.24	202.70	78.87	324.66	0.23	21.17
44.92	$Th_{141}U_{115}O_{512}$	-100.96	5.55	378.94	115.02	61.90	202.99	78.56	325.38	0.23	21.47
50	$Th_{128}U_{128}O_{512}$	-101.03	5.55	379.66	115.09	61.54	203.29	78.30	326.12	0.23	21.82
55.08	$Th_{115}U_{141}O_{512}$	-101.10	5.54	380.45	115.21	61.24	203.63	78.03	326.89	0.23	22.07
60.16	$Th_{102}U_{154}O_{512}$	-101.17	5.53	381.25	115.31	60.96	203.96	77.80	327.70	0.23	22.31

Table 3.7: Bulk properties for various uranium dopant concentrations.

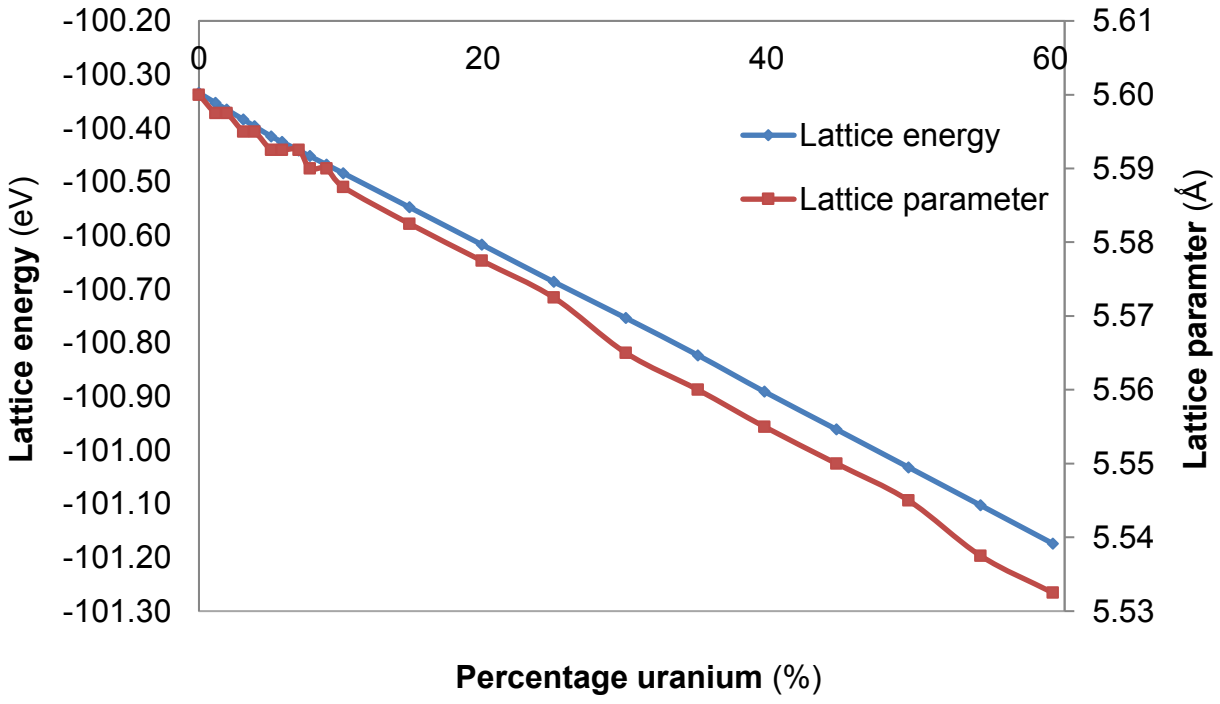

Figure 4.19: Lattice parameter and lattice energy changes with percentage uranium doping.

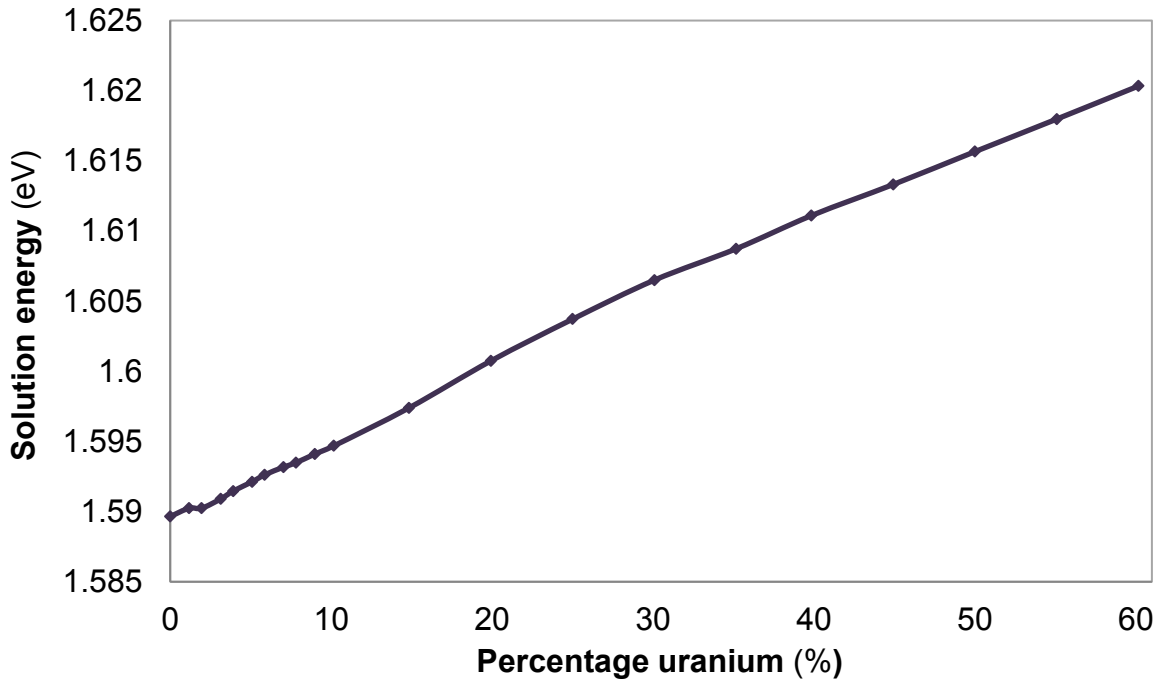

Figure 4.20: A plot of the solution energy against percentage plutonium concentration.

Initial defect simulations were run on the doped system to investigate any changes in defect energy with percentage dopant for up to 5% uranium. For each percentage dopant the configuration with the lowest lattice energy was chosen to complete the defect calculation. The results of the vacancy defect calculations are shown in table 3.8. Upon increased uranium doping the energy for an oxygen vacancy formation increases slightly, the value for the formation of a thorium and uranium vacancy also decreases.

Percentage plutonium (%)	**Defect energy (eV)**		
	Oxygen vacancy	**Thorium vacancy**	**Uranium vacancy**
0	16.15	78.05	-
1.17	16.16	78.01	78.12
1.95	16.17	77.98	78.08
3.13	16.17	77.93	77.99
3.91	16.18	77.87	77.82
5.08	16.18	77.85	77.80

Table 3.8: Simple vacancy defects in the uranium doped ThO_2 system with varying dopant percentage.

Upon doping with both plutonium and uranium, a decrease in lattice parameter and lattice energy is seen. The same trend in vacancy defect energies is also seen throughout the increase in dopant concentration. The 4x4x4 supercell has been sufficient in modelling low percentage compositions and has provided accurate details of the defect and solution energies associated with plutonium and uranium doping.

Chapter summary

The defect formation energies of simple intrinsic defects within the thorium dioxide crystal were investigated including vacancies, defects, Frenkel and Schottky defects. More complex extrinsic defects were also simulated including the doping of fission products such as strontium and barium into interstitial lattice sites. Gadolinium defects were investigated including cluster formation and the effects of percentage gadolinium doping on the lattice parameter of the cell. Initial calculations showed that it was more energetically favourable for the gadolinium cluster to be further apart rather that clustered together. Initial mixed oxide fuel investigations were also carried out in which varying percentages of plutonium and uranium were added to the thorium dioxide supercell. In each case a decrease in lattice parameter and lattice energy was observed. The solution energies for the doping of the plutonium and uranium ions showed in increase in value as doping concentration increased. Simple defect vacancies were calculated for up to 5% dopant concentration within the lowest energy configurations.

Further work

Further work that could be done within this chapter include further investigations into the doping of various fission products into the thorium dioxide fuel including xenon and caesium which would depend upon the derivation of new interatomic potentials. The effects of cluster formation and ion migration could also be investigated for each of the fission products. These calculations could be carried out using molecular dynamics simulations to allow RDF's and MSD's to be investigated.

More in depth defect formation energies could be investigated the in the mixed oxide fuels including the doping of fission products. Thermophysical properties of the mixed oxide fuel such as thermal conductivity and heat capacity calculations would be valuable investigations to take out as it would enable the prediction of the fuel properties under high temperatures.

Chapter 5

Surface Simulations of ThO_2

Contents

5.1 Introduction

The surface chemistry of a material can control many different properties. For many processes the surface of the material will be the first point of contact for example the surface will be the first to interact with in incoming extrinsic defect. In fact, the surface of a nuclear fuel pellet is where corrosion initiates and sits at the interface between the fuel and cladding in a reactor core. Therefore, it is vital to study the surface of a material in order to gain a better understanding of the materials properties and how they can be manipulated. The surface calculations performed and reported in this chapter have all been conducted using the computational atomistic code METADISE. The methodologies behind the workings of this code have been outlined in chapter two.

There has been much interest and research into the surface chemistry of nuclear fuels with particular research into the ThO_2 surface being sparse. The most informative paper published is by Bahera et al. [71] who used all of the thorium dioxide potential published at the time to carry out a number of calculations including surface simulations. Within the research conducted by Bahera et al. they investigated the lower miller index surfaces [111], [110] and [100]. They reported the surface energies within the [111] surface being the lowest energy and therefore the most stable. They also looked into the relaxation of the different surface in depth; studying how the atom positions vary upon relaxation of the surface. Bahera concluded that the most robust potentials used throughout the review were that of Nadeem et al. [26], Osaka et al. [66] and Tharmalingham [72].

In this chapter the surface and attachment energies of the lower index surfaces studied by Bahera et al. have been calculated for comparison. This information has then been

taken forward to investigate the morphology of the crystal and defects within the lowest energy surface.

5.2 The perfect surface

At the start of the simulation the bulk system was generated using the thorium dioxide potential set derived and used throughout the bulk simulations for consistency and the direct comparison of energies with the bulk system. The size of the supercell used within the simulation is critical; a supercell containing too few ions may not give for a realistic simulation and conversely, too many ions may have a considerably long computational time. Therefore, the cell must first be tested for convergence; various properties of the material such as lattice energy were tested against unit cell size until convergence was obtained. Once the correct supercell was selected, the cell was oriented in the correct Miller index and then 'cut' at a non-polar termination of the bulk. A range of Miller indices were cut and surface energies determined (shown in table 3.9) but only the lowest miller index surfaces were taken forward for comparison with other computational work. The lower Miller index surface cut are shown in figure 5.0.

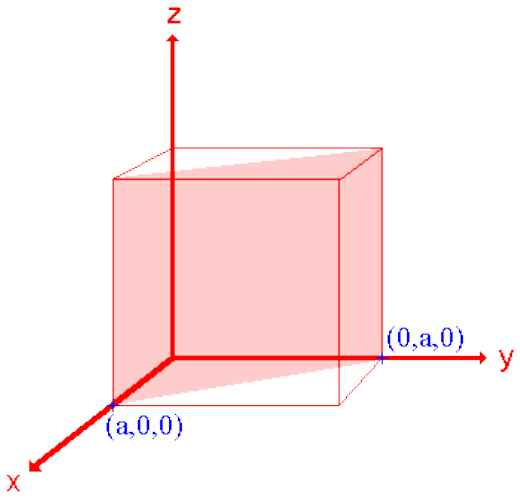

[110]

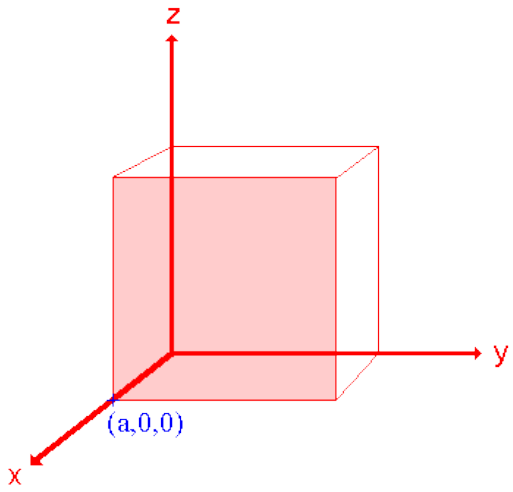

[100]

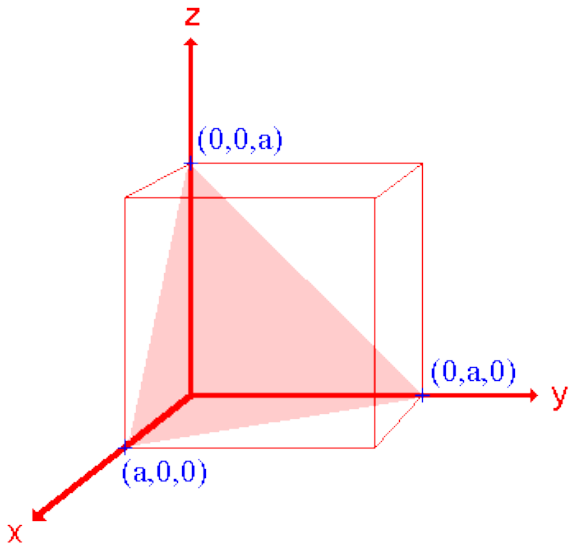

[111]

Figure 5.0: Schematic of the three lower miller index surfaces of the cubic structure

[121]

The maximum cells size for convergence was the 3x3x3 supercell; any expansion on this size caused a significant increase in computational time. The 3x3x3 supercell size allows no deviation from any bulk or surface properties with the advantage of more atoms for the simulation. The studies contained within the Bahera et al. review paper showed a convergence cell size of 40 unit cells. This is much smaller than the 3x3x3 supercell created in this study but to ensure the same supercell size was used throughout this investigation it was important to use a cell size big enough to enable molecular dynamics simulations to be formulated. A plot of convergence values for the lattice parameter and lattice energy with supercell size is shown in table 3.9.

Number of ThO_2 units	Lattice parameter / Å	Lattice energy / eV
4	5.6001	-100.33
32	5.6001	-100.33
108	5.6001	-100.33

Table 3.9: Convergence of supercell size with lattice parameter and lattice energy.

Once the correct supercell size was determined the surfaces were then cut. Figure 5.1 shows the surface structure for the three lowest miller index surfaces.

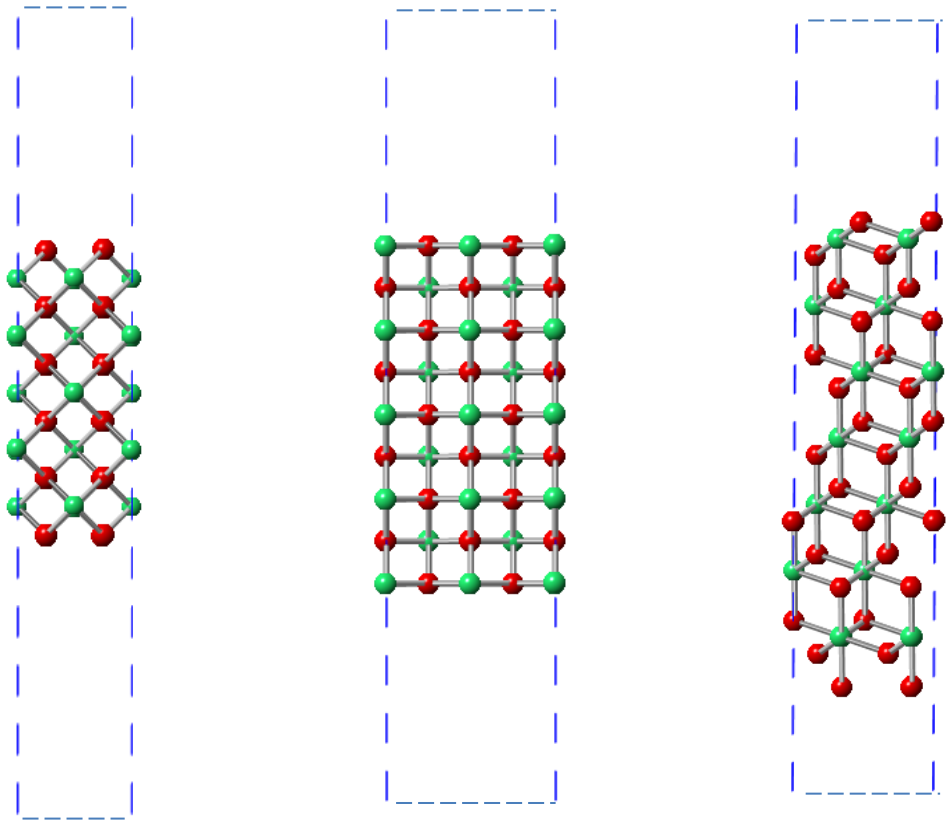

Figure 5.1: Schematic of the three low miller index surfaces used in this study. All surfaces have been relaxed.

The [100] surface has a layer of oxygen atoms at the surface followed by alternating thorium oxygen layers. The [110] surface has alternating oxygen thorium atoms at the surface and in each layer thereafter. The [111] surface has a layer of oxygen atoms on the surface followed by alternating oxygen and thorium layers. The [111] surface does not have as defined layers as the other two surfaces.

5.2.2 Surface and attachment energies

Once the surfaces had been cut the structures were allowed to relax fully using the energy minimisation methods outlined in chapter 2. This caused movement of the ions within the surface of the material. The unrelaxed and relaxed structures for the [111], [100] and [110] surfaces are shown in figures 5.2-5.4. The values for the surface energy for the unrelaxed and relaxed surfaces are shown in table 4.0 along with the attachment energies.

Miller	Unrelaxed surface energy *(Jm^{-2})*	Relaxed surface energy *(Jm^{-2})*	Reference surface energy *(Jm^{-2})*	Attachment energy *(Jm^{-2})*
111	1.50	1.14	1.05 [66] 0.90 [26]	-0.41
100	5.67	2.27	2.25 [66] 2.94 [26]	-0.92
110	3.05	1.77	1.71 [66] 1.43 [26]	-0.69
211	5.93	1.97	-	-2.96
221	7.52	2.17	-	-4.87
010	7.94	2.91	-	-1.29
021	9.15	2.16	-	-4.34
121	5.93	2.02	-	-0.92
210	9.15	2.64	-	-4.34

Table 4.0: Surface and attachment energies for a number of miller indices.

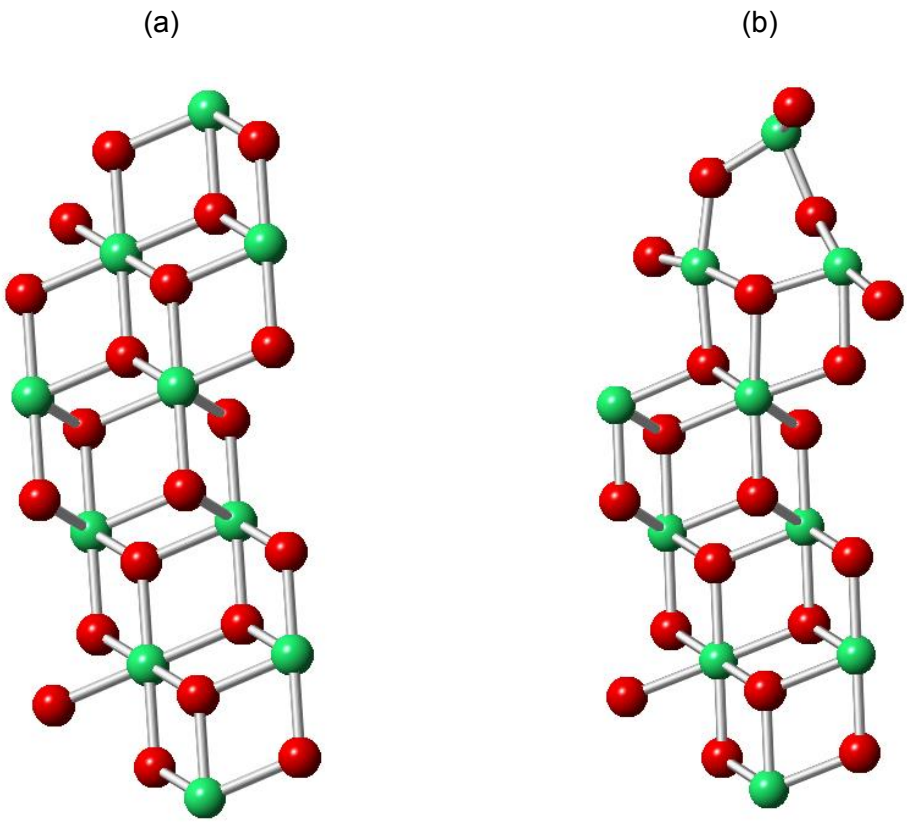

Figure 5.2: Surface structures (a) before and (b) after relaxation of the [111] surface.

The [111] surface ion moved the most upon relaxation with the top uppermost layer distorting a significant amount. The oxygen ions tended to move towards the bulk except for the oxygen that moved to the surface. Even though there was lots of movement of the ions the unrelaxed and relaxed surface energies of the [111] surface do not differ in value a substantial amount (1.50-1.14).

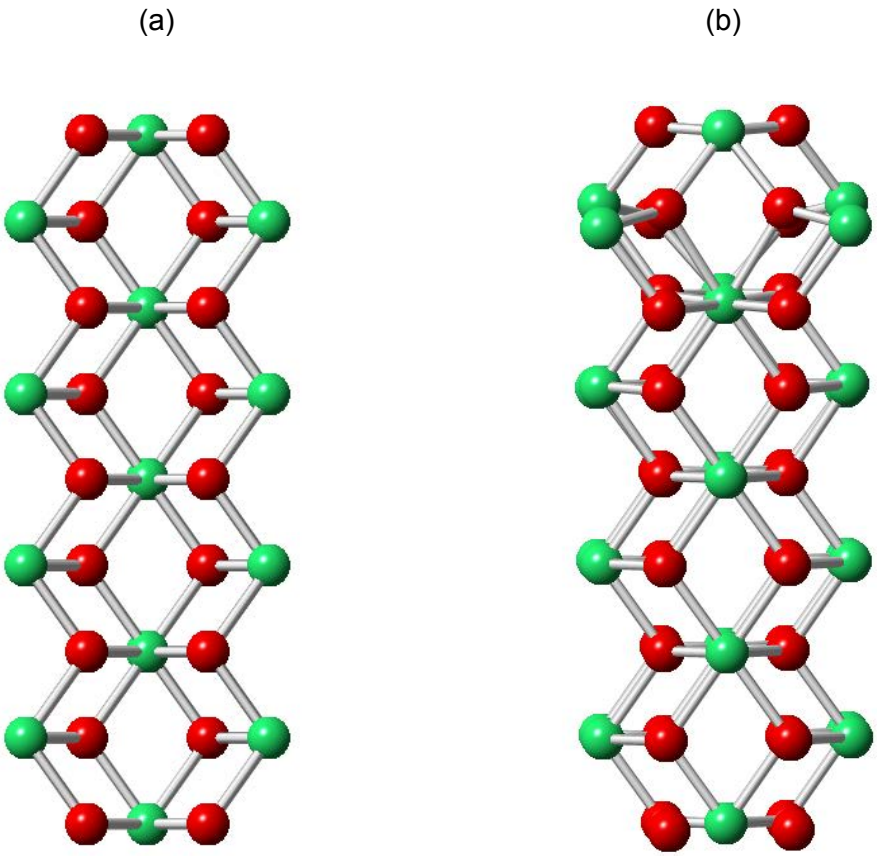

Figure 5.3: Surface structures for (a) before and (b) after relaxation of the [110] surface.

The [110] surface atoms moved slightly upon relaxation with the oxygen atoms adjusting towards the surface and the thorium atoms moving slightly downwards towards the bulk. The relaxed and unrelaxed surface energies of the [110] surface vary a significant amount (3.05-1.77).

(a) (b)

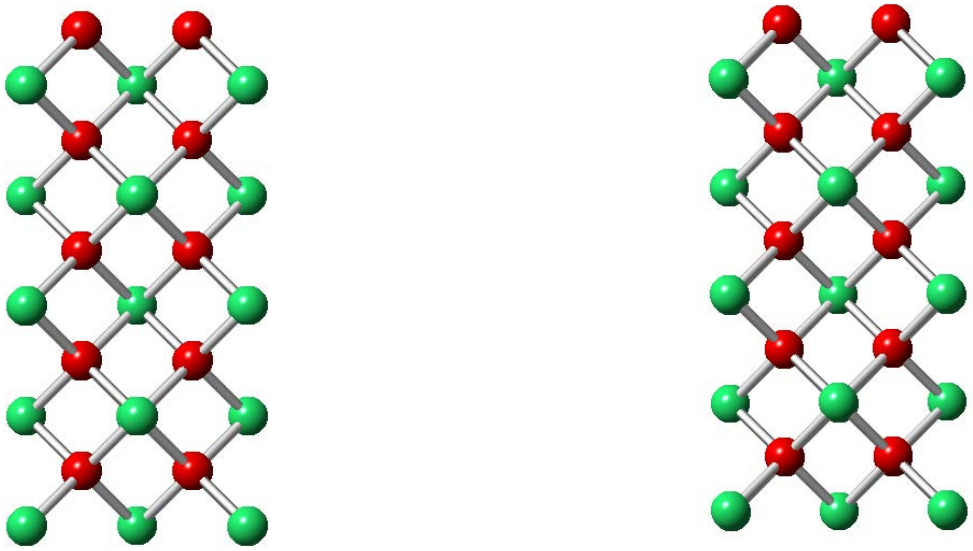

Figure 5.4: Surface structures of (a) before and (b) after relaxation of the [100] surface.

The [100] surface atoms did not seem to move at all upon relaxation but the unrelaxed and relaxed surface energies differ by a large amount (5.67-2.27).

The lower the surface energy, the more stable the surface. The order of stability for the surfaces discussed is shown below:

[111] > [110] > [100]

The surface energies calculated for the lowest miller index surfaces were when compared to other calculated values reports in the Bahera et al. review paper.

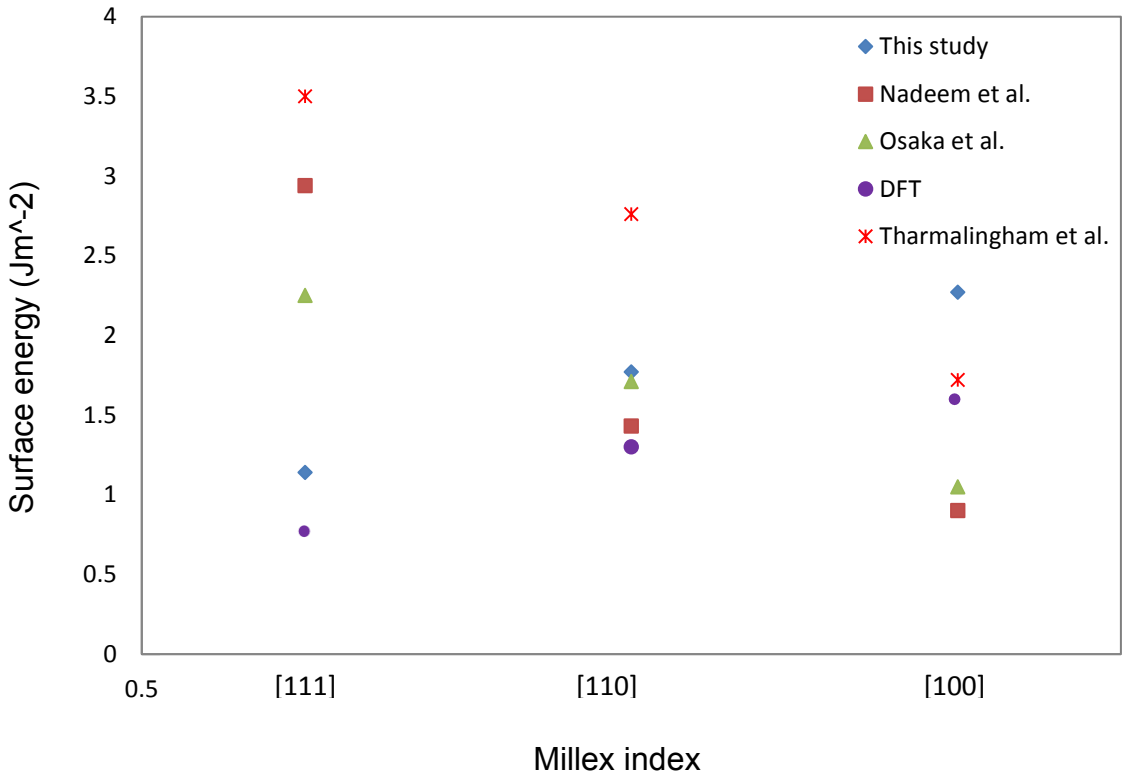

Figure 5.5: Surface energies values calculated in this work compared with the literature value for the three lower miller index surfaces.

The surface energies calculated for the lowest index surfaces in this study agree with those calculated from the robust potentials discussed in the Bahera et al. review paper and a set of potentials used in DFT calculations [123].

5.2.3 Surface morphology

Surface morphology predicts the structure of the material in terms of the surface coverage. The surface energies of the individual cut surfaces are used to determine the surface coverage of the crystal. The morphology of the structure was simulated using the low index surfaces only and the [111] surface dominated the structure throughout.

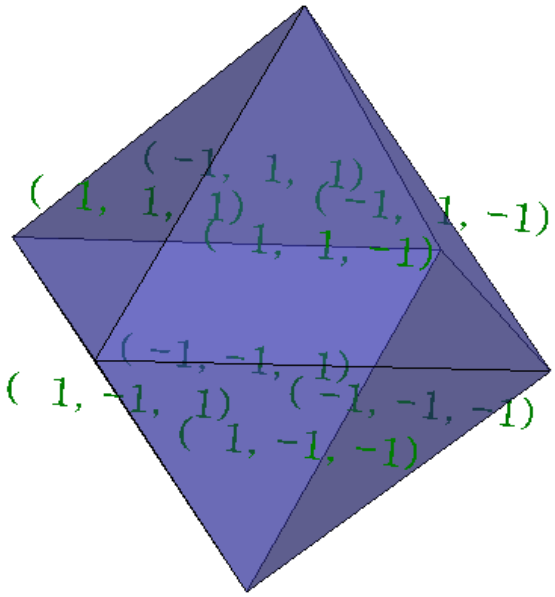

Figure 5.6: Relaxed surface morphology of theThO_2 solid crystal structure. The [111] surface predominates in the structure.

5.2.4 Defective surfaces

Any significant changes in the surface energy of a material will alter the surface morphology and ultimately any surface properties of that material. Therefore it is important that we consider any defects that may occur within the surface. The [111] surface is the most stable and dominated the surface morphology. The defect was first introduced at the surface and integrated into the bulk of the material this provided details about the segregation of the defect; is it more energetically favourable for the defects to remain within the bulk or segregate to the surface. Again, the supercell size was tested for convergence with the defect energies and the 3x3x3 supercell was selected. Table 4.1 shows the results of the defect energy calculations in GULP and METADISE.

Defect	**Surface defect formation energy** *(eV per defect)*	**Bulk defect formation energy** *(eV per defect)*		
		GULP	**METADISE**	**Percentage difference** *(%)*
Th^{4+} vacancy	63.88	78.05	77.74	0.40
O^{2-} vacancy	25.36	16.15	16.14	0.06
Th^{4+} Interstitial	-56.97	-59.13	-59.34	-0.36
O^{2-} Interstitial	-11.35	-11.06	-11.12	-0.54

Table 4.1: Defect formation energies for various simple intrinsic point defects

Initial calculations showed that the thorium vacancy was more energetically favourable at the surface rather than the bulk and that the oxygen vacancy was more energetically favourable within the bulk of the material rather than at the surface. This would suggest that the thorium vacancies would be the most likely to form at the surface of the material and the oxygen vacancies would be most likely to form within the bulk of the material.

5.4 Chapter summary

In this chapter the lower index surface were examined explicitly with relation to their surface energies and attachment energies to determine the most stable surface. The [111] surface was determined to be the most stable surface. The morphology of the crystal was then determined showing predomination of the [111] surface. Some simple defects energies including thorium and oxygen interstitials and vacancies were then determined for the lowest energy [111] surface. All of the results were then compared to literature where possible.

5.5 Further work

Future work in this area would include a more in depth investigation of the defect energy of the three lower index surfaces with inclusion of extrinsic defects such as the fission materials mentioned in chapter four. The segregation of these defects would also be examined in more detail. The grain boundaries could also be investigated as these are thought to be the preferred site for any initial corrosion of the material.

Chapter 6

Molecular dynamics simulations of ThO_2

Contents

6.1 Introduction

Molecular dynamics simulations are used to study the physical movements of atoms, ions or molecules within a given structure. This allows the dynamical evolution of the system to be analysed over time. This is beneficial when predicting the chemical and physical characteristics of a nuclear fuel under the harsh conditions of a nuclear reactor. Static lattice simulations have been able to model the energies related to ion position within the lattice and therefore predict movement of ions throughout the lattice. Molecular dynamics simulations can complement any static calculations by providing detailed information of the mechanisms of diffusion of ions throughout the structure and the evolution of the movement over time [123-125]. These diffusion calculations performed can then be compared to experimental diffusion data. Molecular dynamics simulations can also be used to study the local atomic ordering of the structure and how it varies with time under different conditions.

Molecular dynamics has been proven to be successful in modelling a range of materials from biological molecules [126,127] to solid state chemistry [128-129]. Previously mentioned studies that used molecular dynamics to study thorium dioxide as a fuel include Osaka et al. [66] and Martin et al. [68]. It is these two research papers that have been taken through and used as a comparison to the work done within this chapter. The code used to complete the given calculations performed within this chapter is DL_POLY and the methodology used is outlined in chapter 2.

6.2 The simulation model

Simulations performed within this chapter have been constructed from the 4x4x4 supercell generated for the static calculations discussed previously. This supercell contained around 800 thorium and oxygen ions. The interatomic potentials derived in chapter 3 and used throughout the static simulations have been used throughout the simulations performed in this chapter.

Periodic boundary conditions (discussed in chapter 2) were applied to the system in order to generate an unbound system that contained no surfaces. Initial simulations were performed under conditions of constant volume (V), constant temperature (T) and with a constant number of ions (N) by utilising the NVT ensemble. A pressure of 1 atm was applied to the system and the simulation run with a simulation time of 1 nanosecond ($1x10^{-9}$ s) and a time step of 1 femtosecond ($1x10^{-15}$ s). The system was allowed to equilibrate after 10000 steps (0.01 nanoseconds). Once initial conditions had been applied and the system allowed to equilibrate the ensemble and simulation time could be adapted to fit the simulation being performed.

Initial lattice simulations showed a melting point much lower than that predicted using GULP; changes in lattice parameter with temperature showed a breakdown of the lattice at around 2400K. Therefore, any further simulations performed were limited to a temperature of 2400K. Figure 6.0 shows the structure of the pure ThO_2 simulation cell at 1500K and 2100K in which significant movement of the ions from their lattice positions can be seen.

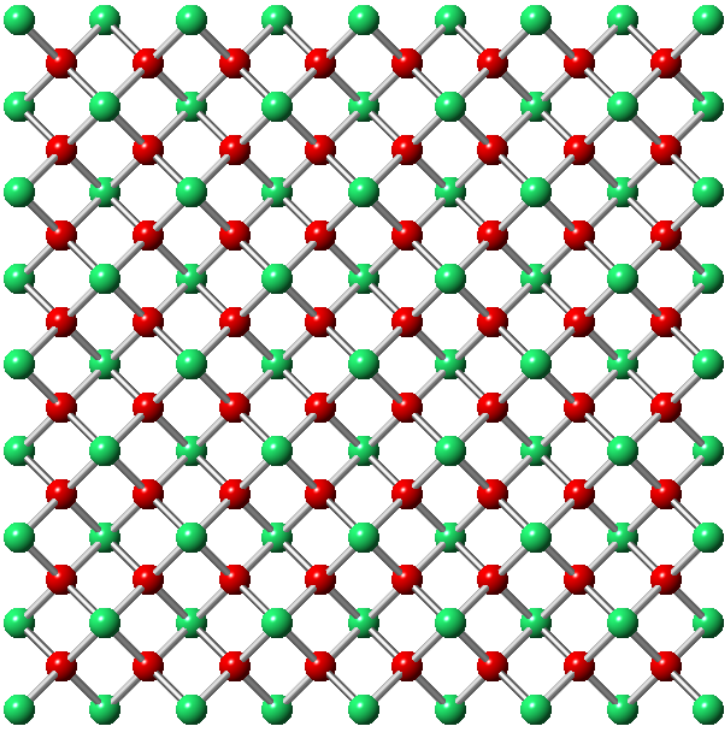

(a)

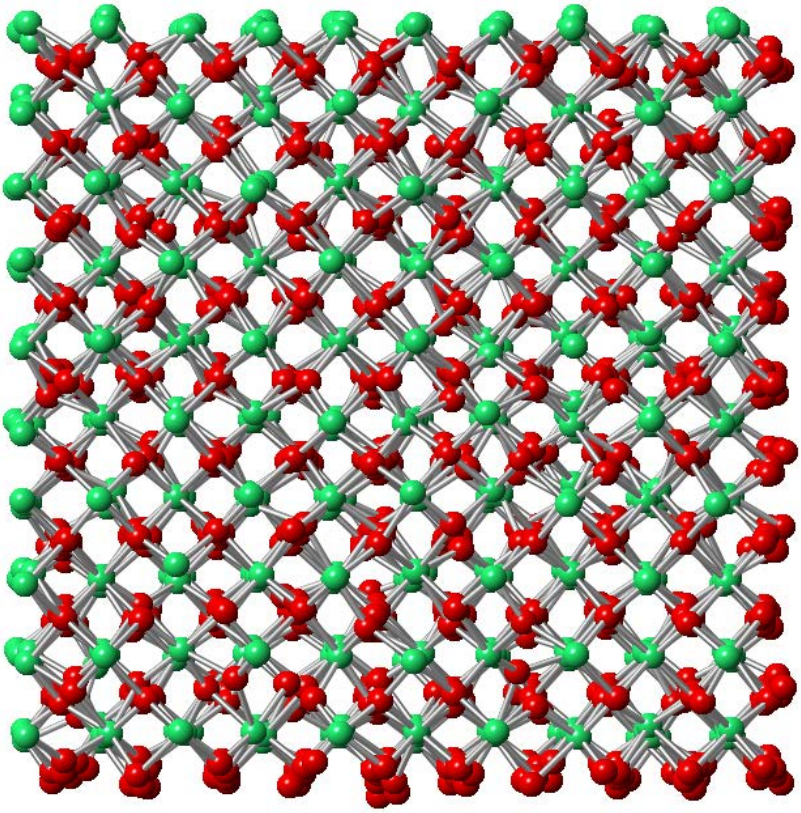

(b)

Figure 6.0: Illustration of the 4x4x4 supercell at (a) 1500K and (b) 2100K.

6.3 Radial distribution function

The radial distribution function is used within molecular dynamics simulations to analyse the trajectory data and determine how the ions are radially distributed around each other. This allows the study of the local atomic ordering over a range of conditions. When a material undergoes a phase change the local atomic ordering will shift causing the radial distribution function to change; solid crystal structures will have a series of sharp peaks that will broaden and shift slightly upon melting. A RDF graph illustrates how the pair correlation function, g(r), changes with relation to the interatomic distance. The pair correlation function is related to the probability of finding the centre of a particle a given distance from the centre of another particle, commonly its nearest neighbours.

In this chapter the radial distribution function for the pure material were investigated; the NPT ensemble was employed to allow the volume of the system to change and the simulations were run for 1 nanosecond with a time step of 1 femtosecond.

Martin et al. calculated the RDF for pure thoria and uranium doped thoria for a range of concentrations and temperatures. They found that there was no change in peak height or placement upon doping of uranium (up to 10% doping) but there was a slight change in the position of the nearest neighbour peak with increasing temperature. The range of temperatures used throughout the work of Martin et al. was 1500 K, 2700K and 3600K. Unfortunately, due to the lower melting point of 2400K predicted by initial MD simulations, temperature of 1500K, 1800K and 2100K were used and compared to the work of Martin et al. where possible.

The partial pair distribution functions, g(r), were calculated for Th-Th, O-O and Th-O pairs and have been compared to the literature where possible. Figure 6.1 shows the

radial distribution function for the Th-O pair at temperatures of 1500K, 1800K and 2100K. It can be seem from figure 6.1, that as the temperature increases the peaks shift very slightly from their original position and they shorten slightly in peak height (g(r)). Figure 6.2 shows the RDF plot for the Th-Th pair at temperatures of 1500K, 1800K and 2100K. As the temperature increases the peak position shifts very slightly and the peak height also decreases. Any changes in peak position show a change in the nearest neighbour distance; an increase in the distance would suggest expansion of the crystal structure.

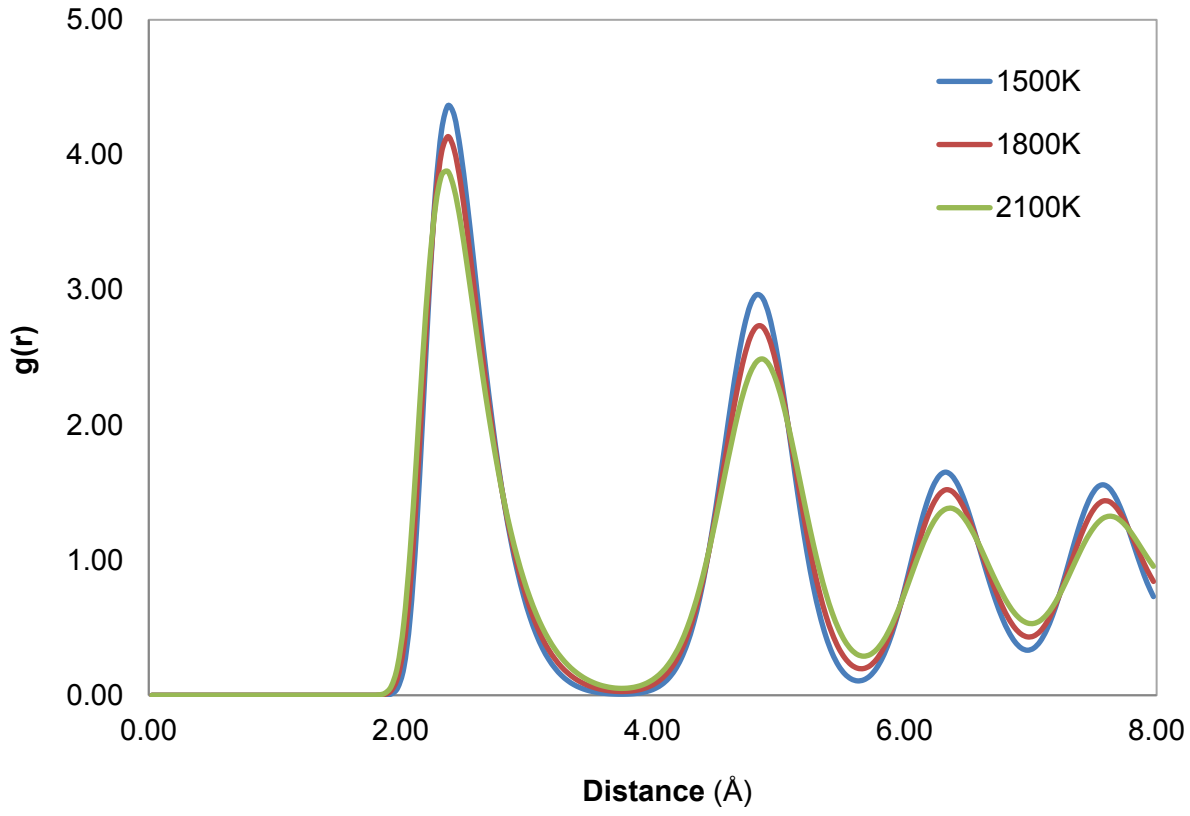

Figure 6.1: Th-O RDF plot for pure ThO_2 at 1500K, 1800K and 2100K.

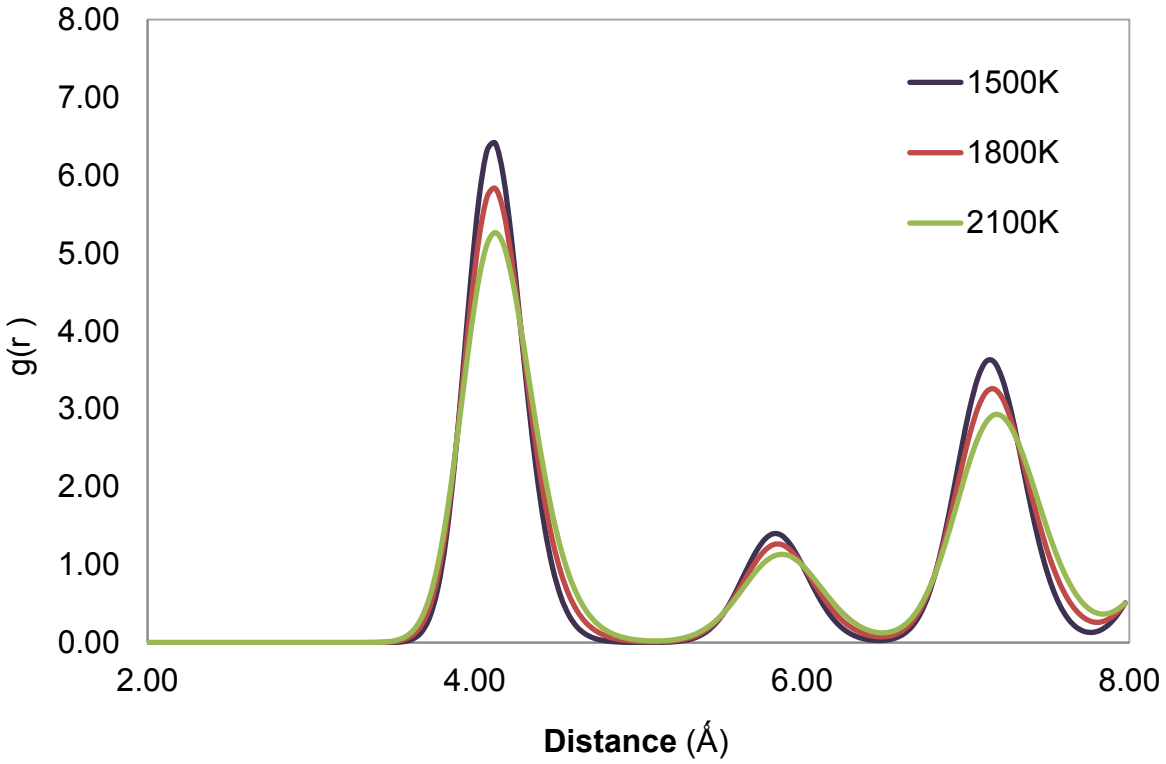

Figure 6.2: Th-Th RDF plot for the pure ThO_2 system at 1500K, 1800K and 2100K.

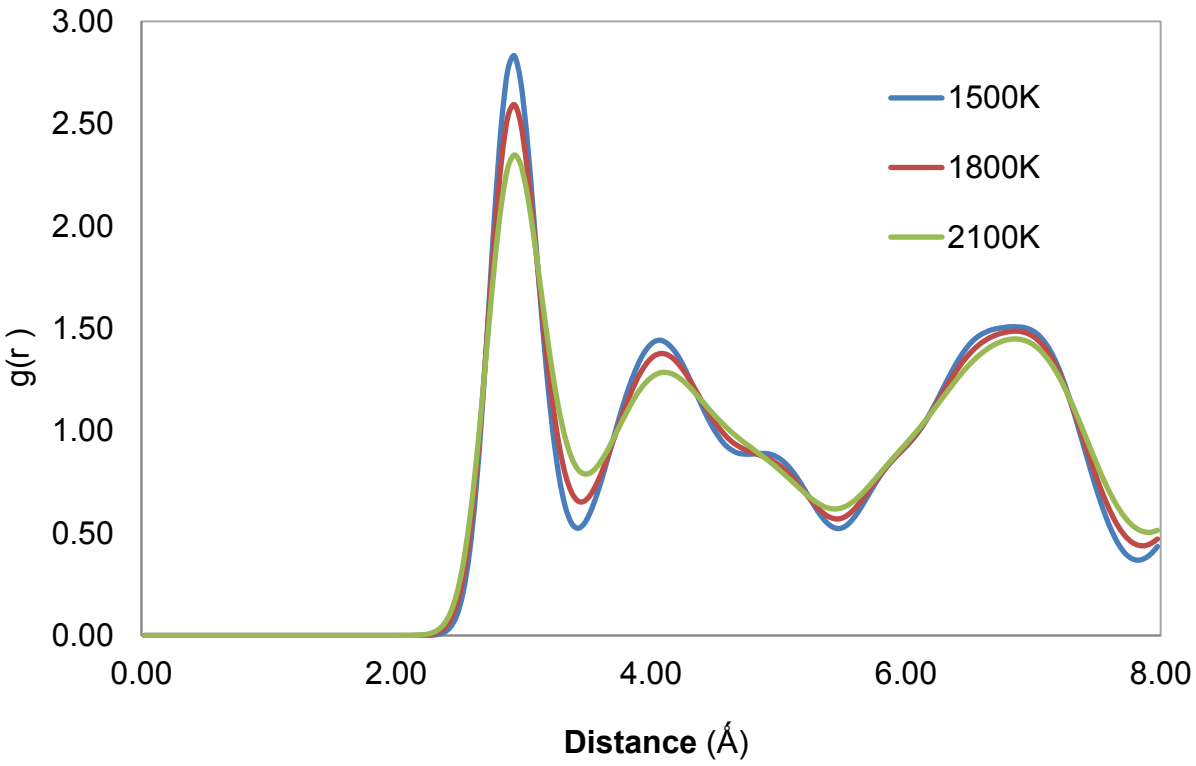

Figure 6.3: O-O RDF plot for the pure ThO_2 system at 1500K, 1800K and 2100K.

The O-O RDF (shown in figure 6.3) shows slight deviations in the structure after the second nearest neighbour because of the cumulative vibrations of the lighter oxygen ions about their lattice positions.

The interatomic potentials used throughout the work of Martin et al. were used within this work to simulate the Th-O, Th-Th and O-O RDF's at 1500K for comparison. The RDF plots that show a comparison of this work with that of Martin et al. are shown in figure 6.4 for the Th-O separation, figure 6.5 for the Th-Th separation and figure 6.6 for the O-O separation. The plot shows the same trend in interatomic separation but the peak position is shifted slightly and the values for g(r) are slightly lower (decrease in peak height). This is a result of different interatomic potentials being used. The potentials derived in this study are a closer fit to the observed crystal structure and thus slightly more repulsive than those used by Martin et al.

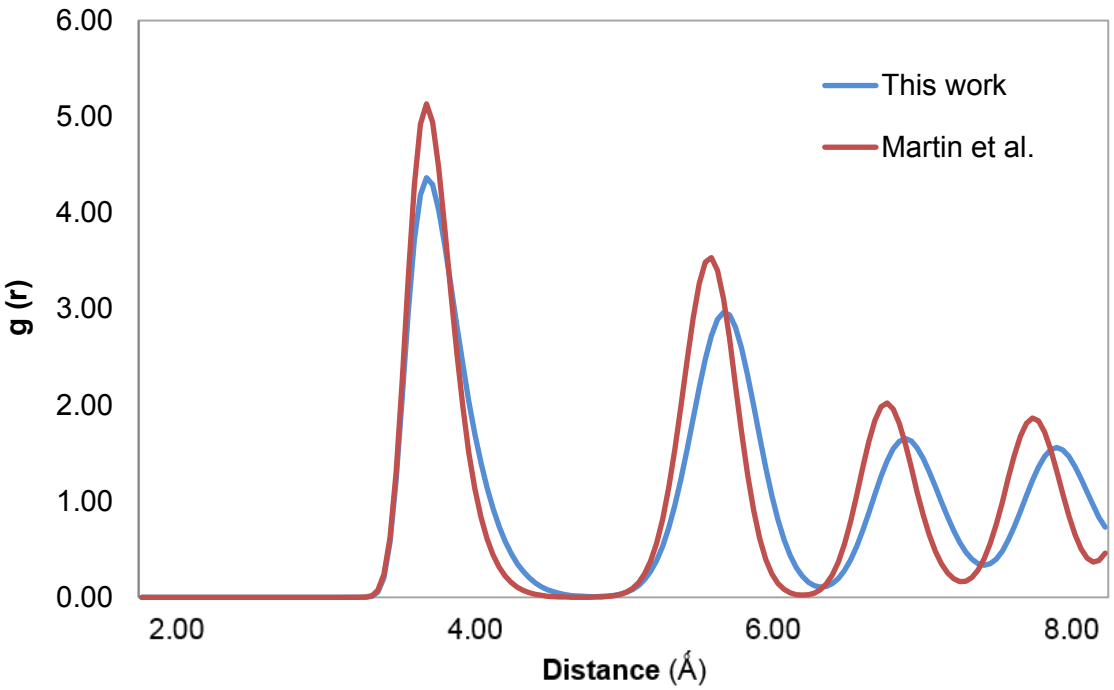

Figure 6.4: RDF for the Th-O pair calculated at 1500K for this work and that of Martin et al.

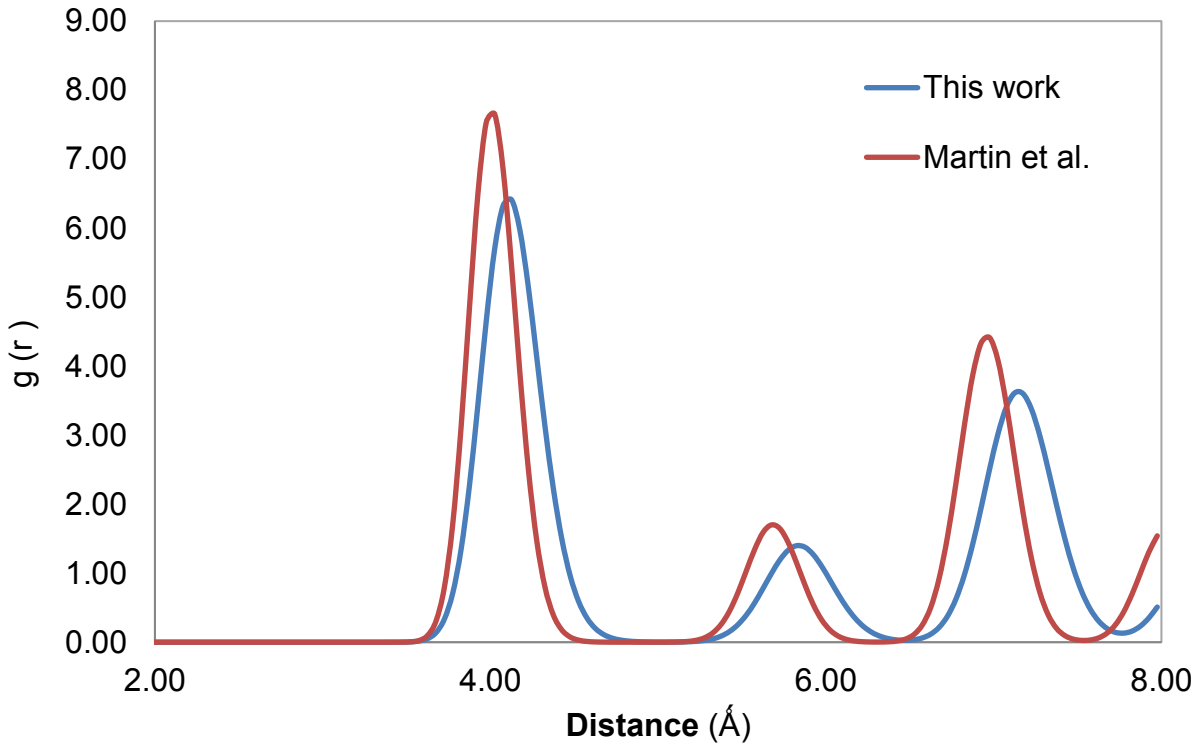

Figure 6.5: RDF for the Th-Th pair calculated at 1500K for this work and that of Martin et al.

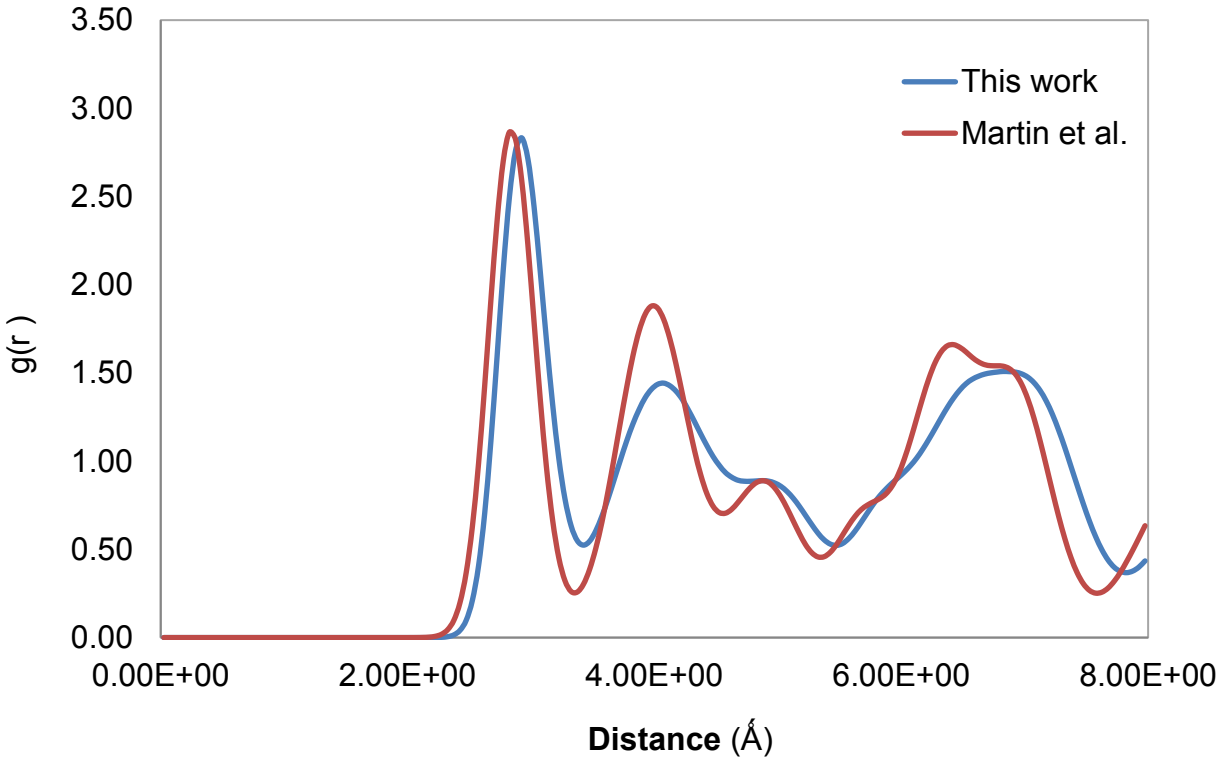

Figure 6.6: RDF for the O-O pair calculated at 1500K for this work and that of Martin et al.

Chapter Summary

The radial distribution plots configured within this work are characteristic of a typical, high symmetry crystalline solid. They show a change in interatomic distance with temperature which is what would be expected as thermal expansion will occur within the crystal structure as temperature increases. The comparison of the RDF's plotted in this work to the work of Martin et al. shows slight differences in peak position and height but have the same general features including the number of nearest neighbours and the average position of the nearest neighbour.

Further work

Earlier surface calculations (discussed in chapter 4) showed that oxygen ions may migrate into the bulk of the material rather than stay at the surface; therefore diffusion of oxygen throughout the material would be a natural progression from initial simulations. Mean square displacement calculations could be carried out to measure the displacement of the oxygen anion from its original lattice position over time in both the pure and mixed oxide fuel. Mean square displacement calculations could also be used to investigate the movement of fission products within the fuel. The radial distribution function for the mixed oxide fuel could be examined with relation to dopant ion concentration to predict expansion or contraction of the fuel upon doping. Osaka et al. studied the RDF's for gadolinium doped thoria and investigated how they changed upon introduction of defects. This investigation would be interesting to repeat as initial static calculations carried out in chapter four show contraction of the unit cell upon increased gadolinium doping.

Chapter 7

Summary

Contents

7.1 Derivation of enhanced interatomic potentials

Within this work, two different derivation methods were used to develop two separate sets of potentials. The ThO_2 potentials were derived using a method that has previously been used for a number of other nuclear materials including UO_2. This method used available experimental data to derive a set of potentials, initially only on lattice parameter data and then later refined using other crystal structure data including elastic constants and dielectric properties. The Gd_2O_3 potentials were derived using a novel piece of Phython code generated within the Read group. The code also used available experimental data to fit to initially, but used a Monte-Carlo type approach in which a potential set was generated via a weighted least squares method to each of the crystal properties.

Both of the methods were successful in deriving a set of potentials that correctly fit the bulk properties of the material with improved percentage difference values to other published potential sets. Both of the potential sets were then taken forward to simulate static, surface and molecular dynamics simulations.

The potential sets derived within this work have proven substantial in modelling both of the materials in various simulations and can therefore be used in any further work with confidence.

7.2 Static Calculations

Within chapter 4, the General Utility Lattice Programme (GULP) was used to model both the pure and doped system with relation to defect formation and thermophysical properties. Defect properties of the pure system included the simulations of simple

intrinsic defects such as interstices, vacancies and frenkel and schottky defects. Once the pure system had been simulated, the defected system could be predicted with respect to extrinsic defect clusters formed by doping of waste materials such as strontium and gadolinium in order to model the evolution of the fuel upon exposure to radiation damage. Finally, the mixed oxide fuel was doped with uranium and plutonium and Many of the intrinsic defect calculations were then repeated within the mixed fuel.

The pure, mixed and fission product doped systems were all exposed to increasing temperatures and properties such as the melting point and lattice expansion coefficient were determined for the pure and mixed oxide fuels. In each case the doping of uranium and plutonium showed a favourable result with respect to improved efficiency and fuel performance.

7.3 Surface calculations

In this chapter the lower index surface were examined explicitly with relation to their surface energies and attachment energies to determine the most stable surface. The [111] surface was determined to be the most stable surface. The morphology of the crystal was then determined showing predomination of the [111] surface. Some simple defects energies including thorium and oxygen interstitials and vacancies were then determined for the lowest energy [111] surface. All of the results were compared to literature where possible.

7.4 Molecular dynamics

Within chapter 6, molecular dynamics simulations were carried out using the DLPOLY code. Firstly, the radial distribution functions of the material were investigated and compared with the recent work of Martin et al. The radial distribution plots configured within this chapter were characteristic of a typical, high symmetry crystalline solid. They showed a change in interatomic distance with temperature, which is what would be expected as thermal expansion will occur within the crystal structure as temperature increases. The comparison of the RDF's plotted in this work to the work of Martin et al. shows slight differences in peak position and height but have the same general features including the number of nearest neighbours and the average position of the nearest neighbour.

These initial high temperature simulations show excellent compatibility of the potential sets derived within this work and those used in combination with the ThO_2 set. They also further prove the strength of the potential sets in relation to further molecular dynamic simulations.

List of References

[1] R. L. Hurst, R. Bezdek, R. Wendling, Peaking of World Oil Production: Impacts, Mitigation & Risk Management, U.S department of energy, 2005, 8-10.

[2] Legislation.gov.uk. Climate Change Act. 2008. C.27 http://www.legislation.gov.uk/ukpga/2008/27/contents [Accessed 9 Sept. 2016]

[3] H.C. Davies, N. Datarnia, *Renewable energy*, 2013, **60**, 355-362.

[4] L. Schlapbatch, A. Zuttel, *Nature*, 2001, **414**, 353-358.

[5] Benjamin K. Sovacool. *Energy Policy.***36** (2008) 2940-2953

[6] Nei.org. (2016). *World Statistics - Nuclear Energy Institute*. [online] Available at: http://www.nei.org/Knowledge-Center/Nuclear-Statistics/World-Statistics [Accessed 12 Aug. 2016].

[7] NIA.org (2016) *Nuclear Industry Association.* [Online]. Available at http://www.niauk.org/facts-and-information-for-nuclear-energy. [Accessed on 12 Aug. 2016]

[8] Nucleartourist.com (1996-2011) *The Virtual Nuclear Tourist*. [Online] Available at http://www.nucleartourist.com/basics/reasons1.htm [Acessed on 9 Sept 2016].

[9] Neil Endicott. Thorium-Fuelled Moleten Salt Reactors. (2013) The Weinburg Foundation .info@the-weinberg-foundation.org.

[10] Lung, O. Gremm. Perspectives of the Thorium fuel cycle. *Nucl. Eng. Des*. **180** (1998) 133-146.

[11] S. Peggs, W. Horak, T. Roser, G. Parks, M. Lindroos,R. Seviour , S. Henderson., *Proceedings of the international particle accelerator conference*. IPAC 2012.(2012) 29-33

[12] A. Ghiorso, W.W. Meinke, and G.T. Seaborg., Artificial Collateral Chains to the Thorium and Actinium Families., *Phys. Rev.* **74**, 695 (1948).

[13] E. Segrè and G.T. Seaborg., Fission Products of Uranium and Thorium Produced by High Energy Neutrons, *Phys. Rev.* **59**, 212 (1941).

[14] Barc.gov.in. (2016). *About Us:ANUSHAKTI - Atomic Energy In India: Strategy for Nuclear Energy - BARC*. [online] Available at: http://www.barc.gov.in/about/anushakti_sne.html [Accessed 12 Aug. 2016].

[15] Bucher, R.G. (January 2009), India's Baseline Plan for Nuclear Energy self-sufficiency stage *(pdf), Argonne National Laboratory,* retrieved 26 March 2012

[16] Jayaram, K.M.V., An Overview of World Thorium Resources, Incentives for Further Exploration and Forecasts for Thorium Requirements in the Near Future (PDF), Hyderabad: IAEA, archived from the original (pdf) on 28 June 2011, retrieved 26 March 2012.

[17] Comparison of Throium and Uranium fuel cycles, *National nuclear laboratory* (11), 11593, **Issue 5**, (2012).

[18] Prof, R. Fleming, Private communication. University of Michigan 2015.

[19] World nuclear association. 2016. *The nuclear fuel cycle*. [ONLINE] Available at: http://www.world-nuclear.org/information-library/nuclear-fuel-cycle/introduction/nuclear-fuel-cycle-overview.aspx. [Accessed 4 September 2016].

[20] Graph of Fission Product Yields. Nuclear Data Centre, japan Atomic Product Yields. http://wwwndc.jaea.go.jp/cgi-bin/FPYfig?iso=nTh232&xpar=z (Accessed on 02/5/2014)

[21] R.J. Orton, O.E. Sturrn, V. Vyshemirsky, M. Calder, D. Gilbert and W. Kolch. Computational modelling of the receptor-tyrosine-kinase-activated MAPK pathway. *Biochem. J.* **392** (2005) 249-261.

[22] H. Chermette. Chemical reactivity indexes in densirt functional theory. *J. Comp. Chem.* **21**, 1, (1999) 129-154.

[23] R.H.J Peerlings, R. de Borst, W. A. M. Brekelmans, M.G.D Geers. *Journal or Mechanics of Cohesive-frictional Materials.* **3** (4) (1998) 323-342

[24] C. Gueneau, N. Duplin, B. Sundam, C. Martial, J. Dumas. *J. Nuc. Mat*. **419** (2011) 145-167.

[25] M.S.D Read. R.A. Jackson. *J. Nuc. Mat*. **406** (2010) 293-303.

[26] M. Nadeem, M.J. Akhtar, R. Shaheen and M.N. Haque. *J. Mater. Sci. Technol*. **17** (2001) 638-642.

[27] P. Martin, D. J. Cooke and R. Cywinski. *J. Appl. Phys*. **112** (2012) 073507.

[28] Gale, J. D., "GULP: A computer program for the symmetry-adapted simulation of solids", J. Chem. Soc., Faraday Trans., 93, 629 (1997).

[29] Watson, G.W., Kelsey, E.T., de Leeuw, N.H., Harris, D.J. & Parker, S.C., 1996. Atomistic simulation of dislocations, surfaces and interfaces in MgO. *Journal of the Chemical Society, Faraday Transactions*, **92**(3), p.433.

[30] Smith, W. and Forester, T. R., "DL POLY 2.0: A general–purpose parallel molecular dynamics simulation package", J. Molec. Graphics, 14, 136 (1996).

[31] Born, M. & Mayer, J.E., 1932. Zur Gittertheorie der Ionenkristalle. *Zeitschrift für Physik*, **75**(1-2), pp.1–18.

[32] P.P Ewald, *Ann, Phys.* **64** (1921) 253.

[33] P.M.Morse. "Diatomic molecules according to the wave mechanics. II. Vibration levels. *Physical review*, **34** (1929).

[34] Verlet, L., "Computer "Experiments" on Classical Fluids. I. Thermodynamical Properties of Lennard–Jones Molecules", *Phys. Rev*., 159, **98** (1967).

[35] R.A. Buckingham., 1938. The classical equation of state of gaseous Helium, Neon and Argon. *Proceedings of the Royal Society A: Mathematical, Physical and Engineering Sciences*, **168**(933), pp.264–283.

[36] B.G. Dick and A.W. Overhauser. *Phys. rev.* **112** (1958) 90-103

[37] M.S Islam. "Ionic transport in ABO3 perovskite oxides: a computer modelling tour. *Journal of Materials Chemistry* **10** (4), 1027-1038 (2000).

[38] CAJ Fisher, VM Hart Prieto, MS Islam. "Lithium Battery Materials Li M PO4 (M= Mn, Fe, Co, and Ni): Insights into Defect Association, Transport Mechanisms, and Doping Behaviour". *Chemistry of Materials* **20** (18), 5907-5915 (2008)

[39] Catlow, C. R. A.; Jackson, R. A. and Thomas, J. M., "Computational Studies of Solid Oxidation Catalysts", *J. Phys. Chem*., **94**, 7889 (1990).

[40] L. Minervini, M. O. Zacate, R. W. Grimes. *J. Solid State Ionics*. **116** (1999) 339.

[41] Shanno, D.F., 1970. Conditioning of quasi-Newton methods for function minimization. *Mathematics of Computation*, **24**(111), pp.647–647.

[42] N.F. Mott, M.J. Littleton. *J. Chem. Soc. Faraday. Trans*. II **85**, Part 5 (1989) 565.

[43] Kenway, P. R.; Parker, S. C. and Mackrodt, W. C., "The calculated structure, stability and composition of the low index surfaces of La2CuO4 and Nd2CuO4", *Surf. Sci*., **326**, 301 (1995).

[43] P.W. Tasker. "The surface energies, surface tensions and surface structure of the alkali halide srystals." *Philosophical magazine* A, **39**, Issue 2 (1979).

[44] D.H. Gay and A.L. Rohl. "MARVIN: a new computer code for studying surfaces and interfaces and its application to calculating the crystal morphologies or corundum and zircon." *J. Chem. Soc., Farady Trans.* **91**(1995) 925-936.

[45] Watson G. W., Kelsey E. T., de Leeuw N. H., Harris D. J., Parker S. C. "Atomistic simulation of dislocations, surfaces and interfaces in MgO" *J. Chem. Soc. Faraday Trans.* **9** (1996) 433-438.

[46] Kerisit S, Cooke DJ, Marmier, A and Parker, SC. " Atomistic simulation of charged iron oxyhydroxide surfaces in contact with aqueous solution" *CHEM COMM* (24): 3027-3029 (2005)

[47] Parker SC, Cooke DC, Kerisit S, Marmier A. "Computer modelling of cation segregation to oxide and mineral surfaces in the presence of water*." ABSTR PAP AM CHEM S* 226: 113-GEOC Part 1 (2003).

[48] Wulff, G., "Zur Frage der geschwindigkeit des Wachstums und der Auflosung der Krystallflachen", *Z. Kristallogr. Kristallgeom.,* 39, 449 (1901).

[49] Gibbs, J. W., On the Equilibrium of Heterogeneous Substances, New York : Longman, vol. 1 edition (1928).

[50] Kern, R., Morphology of Crystals, Terra Scientific Publishing Company, Tokyo, part a, ch.2 edition (1990).

[51] Hartman, P. and Perdok, W. G., “On the Relations Between Structure and Morphology of Crystals. I”, Acta Cryst., 8, 49 (1955).

[52] Mackrodt, W. C.; Davey, R. J.; Black, S. N. and Docherty, R., “The Morphology of Alpha-Al2O3 and Alpha-Fe2O3 - The Importance of Surface Relaxation”, J. Cryst. Growth, 80, 441 (1987).

[53] Ronald M. Levy, Olivia De la Luz Rojas, Richard A. Friesner. Quasi-harmonic method for calculating vibrational spectra from classical simulations on multi-dimensional anharmonic potential surfaces. *J. Phys. Chem.*, **1984**, *88* (19), pp 4233–4238

[54] Hoover, W. G., “Canonical Dynamics - Equilibrium Phase–space Distributions”, Phys. Rev. A, 31, 1695 (1985).

[55] Berendsen, H. J. C.; Postma, J. P. M.; van Gunsteren, W. F.; DiNola, A. and Haak, J. R., “Molecular-Dynamics With Coupling to an External Bath”, J. Chem. Phys., 81, 3684 (1984).

[56] Nose, S., “A Unified Formulation of the Constant Temperature Molecular-Dynamics Methods”, J. Chem. Phys., 81, 511 (1984).

[57] Nose, S., “A Molecular-Dynamics Method for Simulations in the Canonical Ensemble”, Molec. Phys., 52, 255 (1984).

[58] Fincham, D., and Mitchell, P. J., 1993, *J. Phys. Condens. Matter*, **5**, 1031. 54

[59] M.S.D. Read, R.A. Jackson and S. R. Walker. *Pys. Status Solidi C*. **10** (2), (2013) 197-201.

[60] G.C.Benson, P.I. Freeman and E. Dempsey. *J. Am. Ceram. Soc*. **46** (1963) 43-47

[61] W.C. Mackrodt and R.F Stewart. *J. Phys. C: Solid State Phys*. **12** (1979) 431-449.

[62] E. A. Colbourn and W.C. Mackrodt. *J. Nucl. Mater*. **118** (1983) 50-59.

[63] K. Clausen, W. Hayes, J. E. Macdonald, R. Osbourn, P.G. Schnabel, M.T. Hutchings and A. Magerl. *J. Chem. Soc. Faraday. Trans. 2*. **83** (1987) 1109-1112.

[64] M. Nadeem, M.J. Akhtar, R. Shaheen and M.N. Haque. *J. Mater. Sci. Technol*. **17** (2001) 638-642.

[65] M. M. Elcombe and A. W. Pryor. *J. Phys. C: Solid State Phys*. **3** (1970) 492.

[66] M. Osaka. J. Adachi, K. Kurosaki, M. Uno and S. Yamanaka. *J. Nucl. Sci. Technol.* **44** (2007) 1543-1549.

[67] H.Y. Xiao, Y. Zhang and W.J. Weber. *Phys. Review. B*. **86** (2012) 054109.

[68] P. Martin, D. J. Cooke and R. Cywinski. *J. Appl. Phys*. **112** (2012) 073507

[69] G.V. Lewis and C.R.A. Catlow, *J. Phys. C* **18**, 1149-1161 (1985).

[70] R. Cywinski, Bungau, Cristian, Barlow and Roger. *Proc. IPAC2012* (2012) 4112-4114

[71] R. K. Bahera and C. S. Deo. *J. Phys: Condens. Matter.* **24** (2012) 215405.

[72] K. Tharmalingham. *Phil. Mag.* **23** (1971) 199-204.

[73] J. R. Walker and C. R. A. Catlow*. J. Phys. C: Solid State Phys*. **14** (1981) L979-83.

[74] S. M. Lang and F. P. Knudsen. *J. Am. Chem. Soc.* **39** (1956) 412-24.

[75] M. Idiri, T. Le Bihan, S. Heathman and J. Rebizant*. J. Phys. Rev. Ser 3; B. Condens. Matter*. **70** (2001) 014113-1-014113-8.

[76] C. B. Basak, A. K. Sengupta and H. S. Kamath. *J. Alloys. Compounds.* **360** (2003) 210-6.

[77] T. Arima, S. Yamasaki, Y. Inagaki and K. Idemitsu. *J. Alloys. Compunds*. **400** (2005) 43-50.

[78] Y. Lu, Y. Yang and P. Zhang. *J. Phys.: Condens. Matter.* **24** (2012) 225801.

[79] V. Kanchana, G. Valtheeswaran, A. Svane and A. Delin. *J. Phys.: Condens. Matter.* **18** (2006) 9615-9624.

[80] P. J. Kelly and M. S. S. Brooks. *J. Chem. Soc, Faraday. Trans. 2*, **83** (1987) 1189-1203.

[81] H. Y. Xiao, Y. Zhang, W.J. Weber*. J. Nuc. Mat*. **414** (2011) 464-470.

[82] A. Boudjemline, L. Louail, M. M. Islam, B. Diawara*. J. Comp. Mat. Sci.* **50** (2011) 2280-2286.

[83] T. Karakasidis and P. J. D. Lindan*. J. Phys.: Condens. Matter.* **6** (1994) 2965-9.

[84] J. S. Olsen, L. Gerward, V. Kanchana and G. Vaitheeswaran. *J. Alloys. Compounds*. **381** (2004) 36-40.

[85] A. C. Momin, E.B. Mirza and M.D. Mathews. *J. Nuc. Mat.* **185** (1991) 308-310.

[86] R. K. Bhagat, K. Krishan, T.R.G. Kutty, A. Kumar, H.S. Kamath and S. Banerjee. *J. Nuc. Mat.* **422** (2012) 152-157.

[87] P.M. Macedo, W. Capp and J.B. Wachtman. *J. Am.Ceram. Soc*. **47** (1964) 651.

[88] J.D.Axe and G.D.Pettit. *Phys. Rev*. **151** (1966) 676-680.

[89] M. Ishigame and M. Kojima. *J. Phys. Soc. Japan*. **41** (1976) 202-10.

[90] M. J. Sarsfield, R. J. Taylor. C. Puxley and H. M. Steele. *J. Nuc. Mat.* **427** (2012) 333-342.

[91] R. Agarwal, R. Prasad and V. Venugopal. *J. Nuc. Mat.* **322** (2-3), (2003) 98-110.

[92] S. Dash, S.C. Parida, Z. Singh, B.K. Sen and V. Venugopal. *J. Nuc. Mat.* **393** (2009) 276-281.

[93] K. Bakker, E.H.P Cordfunke, R.J.M Konings and R.P.C. Schram. *J. Nuc. Mat.* **250** (1997) 1-12.

[94] R.A. Jackson, A.D. Murray, J.H. Harding and C.R.A. Catlow. *Phil. Mag*. A., 53, 27-50 (1986).

[95] M. H. Xing G, B. E, Song Y, Z. L, S. B, Li X, Wang, P. C, Korotcov. A, L. W, Liang, X. J, Chen, C. Yuan, Z. F, Chen Z, S.T, Chai Z, F. M, Zhao Y.

[96] T.S. Bush, J.D. Gale, C.R.A. Catlow and P.D. Battle. *J. Mater. Chem.* **6**, (1994) 831-837.

[97] Database of published interatomic potentials. www.ucl.ac.uk/klmc/potentials [Accessed January 2014].

[98] S. Yamanouchi and T. Tachibana. *J. Nucl .Sci. Tech.* **25, 6** (1988) 528-533.

[99] F. X. Zhang, M. Lang, J.W. Wang, U. Becker and R.C. Ewing. *Physical review B*. **78** (2008) 064114.

[100] M. D. Mathews, B. R. Ambekar and A.K. Tyagi. *J. Nuc. Mat.* **341** (2005) 19 – 24.

[101] A.M. Pires, M.R. Davolos, C.O. Paiva-Santos, E.B. Stucchi and J. Flor*. J. Solid. State. Chem*. **171** (2003) 420-423.

[102] F.X. Zhang, M. Lang, J.W. Wang, U. Becker and R.C. Ewing. *Physical review B.* **78**, 064114 (2008).

[103] Olander, D.R., *Fundamental aspects of nuclear reactor fuel elements*, Springfield, VA: Energy Research and Development Administration (1976).

[104] Olander, D., Nuclear fuels – Present and future. *Journal of Nuclear Materials*, (2009) 389(1), pp.1–22.

[105] R. Bohler , A. Quaini, L. Capriotti, P. Cakır, O. Beneš, K. Boboridis , A. Guiot , L. Luzzi ,R.J.M. Konings , D. Manara. The solidification behaviour of the UO2–ThO2 system in a laser heating study. *Journal of alloys and compounds.* **616** (2014) 5-13

[106] Ronchi C, Hiernaut JP (1996) Experimental measurement of pre-melting and melting of thorium dioxide. *J Alloys Compound* **240**:179–185.

[107] Benz R (1969) Thorium-thorium dioxide phase equilibria. *J Nucl Mater* **29**:43–49.

[108] Paul A., Tipler; Gene Mosca (2008). *Physics for Scientists and Engineers, Volume 1* (6th ed.). New York, NY: Worth Publishers. pp. 666–670. *ISBN 1-4292-0132-0.*

[109] Marples, J.A.C., 1976. Plutonium 1975 and other actinides : 5th International Conference on Plutonium and Other Actinides 1975: proceedings. In H. Blank & R. Lindner, eds. *Plutonium 1975 and other actinides : 5th International Conference on Plutonium and Other Actinides 1975: proceedings*. Amsterdam: North Holland Publishing Company.

[110] Yamashita, T., Nitani, N., Tsuji, T. & Inagaki, H., 1997. Thermal expansions of NpO2 and some other actinide dioxides. *Journal of nuclear materials*, **245**, pp.72–78.

[111] Kr¨oger, F. A. and Vink, H. J., Solid State Physics, Vol 3, Eds. F. Seitz and D. Turnball, Academic Press, New York (1956).

[112] Read M S D, Islam M S, Watson G W and Hancock F E, 'Defect Chemistry and Surface Properties of LaCoO3', *J. Mater. Chem*. **10**, 2298-2305 (2000)

[113] On the effects of fission product noble metal inclusions on the kinetics of radiation induced dissolution of spent nuclear fuel. Martin Trummer, Sara Nilsson, Mats Jonsson. *Journal of Nuclear Materials Volume* **378**, Issue 1, 15 August 2008, Pages 55–59

[114] Diffusion theory of fission gas migration in irradiated nuclear fuel UO_2. K. Forsberg, A.R. Massih, *Journal of Nuclear Material*, Volume **135**, Issues 2-3 (1985) 140-148.

[115] R. W. Grimes, C. R. A. Catlow. "The Stability of Fission Products in Uranium Dioxide" Published 15 June 1991.DOI: 10.1098/rsta.1991.0062.

[116] S. Liu and J. Cai.*Annals. Nuc. Energy.* **62** (2013) 429-436.

[117] B. Guangwen, S. Shengya and L. Chanyun. *Nucl. Technology.* **183,** 3, (2013) 308-320

[118] Hubert S, Purans J, Heisbourg G, Moisy P, Dacheux N. Local structure of actinide dioxide solid solutions Th(1-x)U(x)O2 and Th(1-x)Pu(x)O2. *Inorg Chem.* 2006 May **15**;45(10):3887-94.

[119] Managing the UK plutonium stockpile. Parliamentary Office of Science and Technology (2005) Number 237. www.parliament.uk/post/home.htm

[120] Thermophysical Properties of Thora-based Fuels. T.R. Govindan Kutty, Joydipta Banerjee, Arun Kumar. Thoria-based Nuclear Fuels, Green Energy and Technology. DOI: 10.1007/978-1-4471-5589-8_2 (2013).

[121] Structure of solid surfaces. http://www.chem.qmul.ac.uk/surfaces/scc/scat1_1b.htm. [Accessed on 01/09/16].

[122] Skomurski F N, Shuller L C, Ewing R C and Becker U 2008. *J. Nucl. Mater.* **375** 290–310

[123] Kawano, M.; Vessal, B. and Catlow, C. R. A., "A Molecular–Dynamics Simulation of the Temperature–Dependence of the Diffusion of Methane in Silicalite", *J. Chem. Soc. Chem.* ***Commun.,*** **12**, 879 (1992).

[124] Wolf, M. L.; Walker, J. R. and Catlow, C. R. A., "Structural and Transport-Properties of β–Al2O3", *Solid State Ionics,* 13, **33** (1984).

[125] Lindan, P. J. D. and Gillan, M. J., "Shell–Model Molecular–Dynamics Simulation of Superionic Conduction in CaF2", *J. Phys.: Condens. Matter,* **5**, 1019 (1993).

[126] Michael R. Jones, Cong Liu, and Angela K. Wilson. Molecular Dynamics Studies of the Protein–Protein Interactions in Inhibitor of κB Kinase-β. *J. Chem. Inf. Model.*, 2014, ***54*** (2), pp 562–572

[127] Swetha RG, Ramaiah S, Anbarasu A[1]. Molecular Dynamics Studies on D835N Mutation in FLT3-Its Impact on FLT3 Protein Structure*. J Cell Biochem,* 2016, 1439-45.

[128] Zhang, X. and Catlow, C. R. A., "Molecular–Dynamics Study of Oxygen Diffusion in YBa2Cu3O6.91", *Phys. Rev. B,* **46**, 457 (1992).

[129] Shimojo, F.; Okabe, T.; Tachibana, F.; Kobayashi, M. and Okazaki, H., "Molecular–Dynamics Studies of Yttria Stabilised. *Chem. Phys. Let.* **247**. (1995) 386-390.